



LAWRENCE
LIVERMORE
NATIONAL
LABORATORY

LIFE Materials: Corrosion and Environmental Cracking of Structural and Cladding Materials Volume 6

J.C. Farmer

November 21, 2008

Disclaimer

This document was prepared as an account of work sponsored by an agency of the United States government. Neither the United States government nor Lawrence Livermore National Security, LLC, nor any of their employees makes any warranty, expressed or implied, or assumes any legal liability or responsibility for the accuracy, completeness, or usefulness of any information, apparatus, product, or process disclosed, or represents that its use would not infringe privately owned rights. Reference herein to any specific commercial product, process, or service by trade name, trademark, manufacturer, or otherwise does not necessarily constitute or imply its endorsement, recommendation, or favoring by the United States government or Lawrence Livermore National Security, LLC. The views and opinions of authors expressed herein do not necessarily state or reflect those of the United States government or Lawrence Livermore National Security, LLC, and shall not be used for advertising or product endorsement purposes.

This work performed under the auspices of the U.S. Department of Energy by Lawrence Livermore National Laboratory under Contract DE-AC52-07NA27344.

LLNL-TR-408942

**LIFE Materials:
Corrosion and Environmental Cracking of
Structural and Cladding Materials
Volume 6**

Joseph Collin Farmer

Physical and Life Sciences Directorate

National Ignition Facility and Photon Sciences Directorate

Lawrence Livermore National Laboratory

7000 East Avenue

Livermore, California 94550

July 4th 2008 – Initial Report

October 5th 2008 – Revision 1

October 12th 2008 – Revision 2

October 15th 2008 – Revision 3

December 15th 2008 – Revision 4

Executive Summary

The National Ignition Facility (NIF) project, a laser-based Inertial Confinement Fusion (ICF) experiment designed to achieve thermonuclear fusion ignition and burn in the laboratory, is under construction at the Lawrence Livermore National Laboratory (LLNL) and will be completed in April of 2009. Experiments designed to accomplish the NIF's goal will commence in late FY2010 utilizing laser energies of 1 to 1.3 MJ. Fusion yields of the order of 10 to 20 MJ are expected soon thereafter.

Laser initiated fusion-fission (LIFE) engines have now been designed to produce nuclear power from natural or depleted uranium without isotopic enrichment, and from spent nuclear fuel from light water reactors without chemical separation into weapons-attractive actinide streams. A point-source of high-energy neutrons produced by laser-generated, thermonuclear fusion within a target is used to achieve ultra-deep burn-up of the fertile or fissile fuel in a sub-critical fission blanket. Fertile fuels including depleted uranium (DU), natural uranium (NatU), spent nuclear fuel (SNF), and thorium (Th) can be used. Fissile fuels such as low-enrichment uranium (LEU), excess weapons plutonium (WG-Pu), and excess highly-enriched uranium (HEU) may be used as well. Based upon preliminary analyses, it is believed that LIFE could help meet worldwide electricity needs in a safe and sustainable manner, while drastically shrinking the nation's and world's stockpile of spent nuclear fuel and excess weapons materials. LIFE takes advantage of the significant advances in laser-based inertial confinement fusion that are taking place at the NIF at LLNL where it is expected that thermonuclear ignition will be achieved in the 2010-2011 timeframe.

Starting from as little as 300 to 500 MW of fusion power, a single LIFE engine will be able to generate 2000 to 3000 MWt in steady state for periods of years to decades, depending on the nuclear fuel and engine configuration. Because the fission blanket in a fusion-fission hybrid system is subcritical, a LIFE engine can burn any fertile or fissile nuclear material, including un-enriched natural or depleted U and SNF, and can extract a very high percentage of the energy content of its fuel resulting in greatly enhanced energy generation per metric ton of nuclear fuel, as well as nuclear waste forms with vastly reduced concentrations of long-lived actinides. LIFE engines could thus provide the ability to generate vast amounts of electricity while greatly reducing the actinide content of any existing or future nuclear waste and extending the availability of low cost nuclear fuels for several thousand years. LIFE also provides an attractive pathway for burning excess weapons Pu to over 99% FIMA (fission of initial metal atoms) without the need for fabricating or reprocessing mixed oxide fuels (MOX). Because of all of these advantages, LIFE engines offer a pathway toward sustainable and safe nuclear power that significantly mitigates nuclear proliferation concerns and minimizes nuclear waste.

An important aspect of a LIFE engine is the fact that there is no need to extract the fission fuel from the fission blanket before it is burned to the desired final level. Except for fuel inspection and maintenance process times, the nuclear fuel is always within the core of the reactor and no weapons-attractive materials are available outside at any point in time. However, an important consideration when discussing proliferation concerns associated with any nuclear fuel cycle is the ease with which reactor fuel can be converted to weapons usable materials, not just when it is extracted as waste, but at any point in the fuel cycle. Although the nuclear fuel remains in the core of the engine until ultra deep actinide burn up is achieved, soon after start up of the engine, once the system breeds up to full power, several tons of fissile material is present in the fission blanket. However, this fissile material is widely dispersed in millions of fuel pebbles, which can be tagged as individual accountable items, and thus made difficult to divert in large quantities.

Several topical reports are being prepared on the materials and processes required for the LIFE engine. Specific materials of interest include:

- Baseline TRISO Fuel (TRISO)
- Inert Matrix Fuel (IMF) & Other Alternative Solid Fuels
- Beryllium (Be) & Molten Lead Blankets (Pb/PbLi)
- Molten Salt Coolants (FLIBE/FLiNaBe/FLiNaK)
- Molten Salt Fuels (UF₄ + FLIBE/FLiNaBe)
- Cladding Materials for Fuel & Beryllium
- ODS FM Steel (ODS)
- Solid First Wall (SFW)
- Solid-State Tritium Storage (Hydrides)

This Topical Report is Volume 6 in a 12-volume series which is summarized below, and discusses data and models that account for the corrosion and environmental cracking of as-received and irradiated structural and cladding materials in high-temperature molten-salt coolants and liquid fuels. Liquid metal coolants such as Pb-17Li may have to be dealt with in future editions as the engine design further evolves.

Topical reports are organized in 12 volumes:

- Volume 1 – Overview of Fuels & Structural Materials Issues
- Volume 2 – Design & Fabricability
- Volume 3 – Transmutation & Phase Formation
- Volume 4 – Radiation Effects
- Volume 5 – Thermomechanical Effects
- Volume 6 – Corrosion & Environmental Cracking
- Volume 7 – Molten-Salt Coolants
- Volume 8 – Molten-Salt Fuels
- Volume 9 – On-Site Solid-State Tritium Storage
- Volume 10 – Proliferation Resistance
- Volume 11 – Fuel Cycle & Repository
- Volume 12 – Licensability

Volume 6, entitled Corrosion and Environmental Cracking, is organized as follows:

- Executive Summary
- Table of Contents, List of Tables, and List of Figures
- Acronyms & Nomenclature
- Chapter A. LIFE Requirements for Materials
- Chapter B. Summarize Existing Knowledge
- Chapter C. Gaps in Knowledge & System Vulnerabilities
- Chapter D. Strategy for Future Work
- Bibliography
- Tables Summarizing Important Properties
- Figures & Illustrations

Table of Contents

| | |
|--|----|
| Executive Summary | 2 |
| Table of Contents..... | 5 |
| List of Tables | 8 |
| List of Figures..... | 8 |
| Acronyms | 11 |
| Acronyms | 11 |
| Nomenclature..... | 13 |
| Chapter A. LIFE Requirements for Materials | 19 |
| Mission | 19 |
| Tungsten First Wall..... | 19 |
| Neutron Multiplication Blanket | 19 |
| Fission Blanket..... | 20 |
| Engine & Structural Materials | 20 |
| Molten Salt Coolant | 20 |
| Chapter B. Summary of Existing Knowledge | 21 |
| Topical Report | 21 |
| Nuclear Reactions | 21 |
| Overview of Materials of Construction..... | 22 |
| Tungsten First Wall..... | 22 |
| Neutron Multiplication Blanket | 23 |
| Sub-Critical Fission Blanket..... | 24 |
| Structural and Cladding Materials | 24 |
| Iron-Based and Nickel-Based Steels | 25 |
| Oxide Dispersion Strengthened (ODS) Ferritic Steels..... | 26 |

| | |
|---|----|
| Alternatives to Steel | 27 |
| Vanadium Alloys..... | 27 |
| Molybdenum Alloys..... | 28 |
| Niobium Alloys | 28 |
| Other Advanced Materials of Interest | 28 |
| Corrosive Environments..... | 29 |
| Molten Salt Coolants | 29 |
| Liquid Fuels & Continuous On-Line Reprocessing | 31 |
| Corrosive Attack of Engine Materials..... | 33 |
| Corrosion Mechanisms | 33 |
| Corrosion Models | 36 |
| Tafel Kinetics Applied to Anodic and Reactions..... | 36 |
| Effects of Mass Transport on Rate of Corrosion | 37 |
| Approximations Based Upon Mass-Transport Limited Currents | 38 |
| Threshold Potential for Localized Corrosion..... | 40 |
| Application of Mixed Potential Theory to Engine Materials | 40 |
| Cathodic Protection and Sacrificial Anodes | 44 |
| Corrosion Rate Limited by Corrosion Product Solubility | 45 |
| Mechanical Fracture and Fatigue | 50 |
| Environmental Fracture | 51 |
| Chapter C. Gaps in Knowledge & System Vulnerabilities | 53 |
| Chapter D. Strategy for Future Work..... | 54 |
| Objectives | 54 |
| Tasks..... | 55 |
| Deliverables | 56 |

| | |
|--|----|
| Experimental Methodology | 56 |
| Electrochemical Measurement of Corrosion Rates | 56 |
| Determining the Effects of Mass Transfer on Corrosion Rate | 57 |
| Determining Solubility Limited Corrosion Rate from Dissolved Metal | 57 |
| Electrochemical Impedance Spectroscopy of Interface | 58 |
| Thermal Pulsing & Corrosion Fatigue | 62 |
| Measurements of Small Ion-Beam Irradiated Samples | 63 |
| Integrated Predictive Models | 64 |
| Summary..... | 64 |
| Acknowledgements..... | 66 |
| Bibliography | 66 |
| Table..... | 73 |
| Figures | 80 |

List of Tables

| | |
|--|----|
| Table 1 – Important Physical Properties of Candidate Structural Materials | 73 |
| Table 2 – Blanket and Coolant Properties | 74 |
| Table 3 – Free Energies of Formation for Various Fluorides | 75 |
| Table 4 – Results of corrosion tests in LiF-19.5CaF ₂ at 797°C (1467°F) for 500 h (a) | 76 |
| Table 5 – Corrosion of Steels in High Temperature Molten Salts..... | 77 |
| Table 6 – Solubility of Chromium in Various Fluoride Salts..... | 79 |

List of Figures

| | |
|--|----|
| Figure 1 – Structure of LIFE engine, showing contacting of ODS ferritic steel structure, fission fuel, and beryllium neutron multiplier by flowing molten salt coolants..... | 80 |
| Figure 2 – The operating windows for materials used to construct the LIFE engine are bounded by radiation embrittlement at lower temperatures, and by thermal creep at higher temperatures..... | 80 |
| Figure 3 – Yield strength of new ODS FM steels such as 9Cr-ODS & Kobe 12YWT showing exceptional yield strength at high temperature..... | 81 |
| Figure 4 – Elongation of new ODS FM steels such as 9Cr-ODS & Kobe 12YWT showing exceptional creep resistance at high temperature..... | 81 |
| Figure 5 – ODS ferritic-martensitic steel has longer fatigue life than conventional ferritic steels such as modified 9Cr-1Mo steel. | 82 |
| Figure 6 – A binary mixture of BeF ₂ and LiF produces a eutectic composition. The mixture of BeF ₂ and LiF forms a low-melting eutectic (Li ₂ BeF ₄) with a melting point of less than 638 K (365°C)..... | 83 |
| Figure 7 – Calculated phase diagram for molten salt fuel, showing regions of composition and temperature where only liquid exists, which defines the limits of safe operation. The solubility of PuF ₃ and other fission product salts bound the safe operating temperature for liquid fuels..... | 84 |
| Figure 8 – Corrosion mechanism for ODS ferritic steel in molten FLIBE based upon discussion in the literature..... | 85 |
| Figure 9 – Schematic representation showing rotating disk electrode (lower face of cylinder), with the fluid flow approaching the electrode normal to the lower surface. | 85 |

| | |
|--|----|
| Figure 10 – Mixed potential theory applied to ODS ferritic steel without sacrificial beryllium anode in molten Li_2BeF_4 at 815°C..... | 86 |
| Figure 11 – Mixed potential theory applied to ODS ferritic steel with sacrificial beryllium anode in molten Li_2BeF_4 at 815°C..... | 86 |
| Figure 12 – A comparison of these two curves, taken from Figures 10 and 11 respectively, clearly show the cathodic shift of the open circuit corrosion potential due to galvanic coupling of beryllium and ODS steel at 815°C. A comparison of these two curves shows the cathodic shift of the corrosion potential due to galvanic coupling. | 87 |
| Figure 13 – Limited corrosive attack of ODS by molten salts at 815°C, assuming a rate of attack of 5.0 mils per year, and saturation of the salt with chromium at a concentration of approximately 3000 ppm. | 88 |
| Figure 14 – Limited corrosive attack of ODS by molten salts at 815°C, assuming a rate of attack of 70.1 mils per year, and saturation of the salt with chromium at a concentration of approximately 3000 ppm. | 88 |
| Figure 15 – This drawing shows a cross-sectional view of a high temperature test chamber, showing the exposure of multiple samples of structural or cladding material. | 89 |
| Figure 16 – The samples can be frozen in the high-temperature molten fluoride salt for cross-sectioning to enable scanning electron microscopy (SEM) and energy dispersive analysis with X-rays (EDAX), thereby enabling elemental mapping of the corroded interface, and the concentration profile of dissolved metals in the frozen salt. | 89 |
| Figure 17 – Scanning electron microscopy of ODS steel after corrosive attack by molten fluoride salts at 750°C..... | 90 |
| Figure 18 – Electrochemical cell for corrosion testing of structural and cladding materials in high-temperature molten fluoride salts. The material being tested is held in the cell by a machined ceramic plug. The lower right image shows the cell at 800°C..... | 91 |
| Figure 19 – Photographs showing working electrode (larger disk of ODS steel on left), reference electrode (smaller disk of ODS steel on right), and counter electrode (platinum bar suspended above the two ODS steel disks). | 92 |
| Figure 20 – Electrical resistance of high-temperature electrochemical cell for testing structural and cladding materials in high-temperature molten-salt environments showing the melting of the salt and wetting of the sample as the cell is heated to 800°C. Such monitoring enables experimentalist to determine when to begin measurements..... | 93 |

| | |
|--|----|
| Figure 21 – The ability to perform <i>in situ</i> electrochemical impedance spectroscopy (EIS) of steel surface in molten-salt at 800°C has been demonstrated. We can now begin to elucidate high temperature molten salt corrosion mechanisms and monitor corrosion rates at 363°C to temperatures above 800°C <i>in situ</i> | 94 |
| Figure 22 – The simple single time-constant equivalent circuit is insufficient to explain EIS spectra. A two time constant model is required to explain observed impedance spectra qualitatively, with more parameters needed for better fit. | 94 |
| Figure 23 – Test sample of ODS ferritic steel being thermally stressed for fatigue and corrosion fatigue studies with current pulse. | 95 |
| Figure 24 – Timing chart showing current pulse and sympathetic transient temperature during testing of a sample such as ODS steel..... | 95 |
| Figure 25 – Schematic showing surface flaws where corrosion fatigue cracking can initiate and propagate. | 96 |
| Figure 26 – Schematic showing the determination of the Ultimate Tensile Strength (UTS) of ion-beam irradiated sample through determination of the Brinell Hardness Number (BHN). | 96 |
| Figure 27 – A systematic approach to materials modeling will enable design of next-generation materials. | 97 |

Acronyms

| | |
|---------|--|
| ATR | Advanced Test Reactor |
| ABWR | Advanced Boiling Water Reactor |
| ALWR | Advanced Light Water Reactor |
| APWR | Advanced Pressurized Water Reactor |
| BHN | Brinell Hardness Number |
| BWR | Boiling Water Reactor |
| CTE | Coefficient of Thermal Expansion |
| CV | Cyclic Voltammetry |
| EIS | Electrochemical Impedance Spectroscopy |
| FFHR | Force Free Helical Reactor |
| FIMA | Fission of Initial Metal Atoms |
| FLIBE: | Molten Fluoride Salt (Li_2BeF_4) |
| FLINABE | Molten Fluoride Salt (LiNaBeF_4) |
| FLINAK | Molten Fluoride Salt (Li-Na-K-F) |
| HEU | Highly Enriched Uranium |
| HIC | Hydrogen Induced Cracking |
| HFIR | High Flux Isotope Reactor |
| ICF | Inertial Confinement Fusion |
| INL | Idaho National Laboratory |
| IMF | Inert Matrix Fuel |
| IPyC | Inner Pyrolytic Carbon (Layer) |
| LEU | Low Enriched Uranium |
| LIFE | Laser Initiated Fusion-Fission Energy |
| LLNL | Lawrence Livermore National Laboratory |

| | |
|-------|---|
| LP | Linear Polarization |
| LWR | Light Water Reactor |
| MD | Molecular Dynamic |
| NIC | National Ignition Campaign |
| NIF | National Ignition Facility |
| NP | New Production |
| NPR | New Production Reactor |
| MHTGR | Modular High Temperature Gas-Cooled Reactor |
| OCP | Open Circuit Potential |
| ODS | Oxide Dispersion Strengthened |
| OPyC | Outer Pyrolytic Carbon (Layer) |
| ORNL | Oak Ridge National Laboratory |
| PWR | Pressurized Water Reactor |
| RN | Radionuclide |
| SCC | Stress Corrosion Cracking |
| SDR | Slip Dissolution Repassivation |
| SHC | Solid Hollow Core Fuel |
| SNF | Spent Nuclear Fuel |
| SSRT | Slow Strain Rate Testing |
| TMT | Thermo Mechanical Treatment |
| TRISO | TRI-ISO-tropic Fuel |
| UTS | Ultimate Tensile Strength |
| WP | Waste Package |
| YMP | Yucca Mountain Project |

Nomenclature

| | |
|-----------------|---|
| A, A_{ods} | Area of engine wall being corroded; Area of ODS steel being corroded |
| A_0 | Coefficient 0 in polynomial expression relating stress to crack depth |
| A_1 | Coefficient 1 in polynomial expression relating stress to crack depth |
| A_2 | Coefficient 2 in polynomial expression relating stress to crack depth |
| A_3 | Coefficient 3 in polynomial expression relating stress to crack depth |
| BHN | Brinell Hardness Number |
| C_d | Double layer capacitance at electrode-electrolyte interface |
| C_p | Parallel capacitance in equivalent circuit representing electrochemical cell |
| C_s | Series capacitance in equivalent circuit representing electrochemical cell |
| C_w | Warburg capacitance in equivalent circuit representing electrochemical cell |
| $C_{0,j}(0,t)$ | Concentration of j^{th} oxidized species – species being reduced |
| $C_{R,j}(0,t)$ | Concentration of j^{th} reduced species – species being oxidized |
| CTE | Coefficient of thermal expansion |
| D_j | Diffusion of j^{th} species in molten salt coolant or fuel |
| E | Voltage across equivalent circuit in complex notation |
| E | Young's modulus of elasticity |
| E | Electrochemical potential |
| E_{mix} | Mixed potential corresponding to open circuit corrosion potential |
| E_{corr} | Open circuit corrosion potential |
| $E_{threshold}$ | Threshold (critical) potential for initiation of localized corrosion |
| ΔE | Difference between corrosion and threshold potentials ($\Delta E = E_{corr} - E_{threshold}$) |

| | |
|------------------|--|
| E_j^0 | Standard potential for the j^{th} oxidation-reduction couple |
| F | Faraday's constant (96,500 C/equiv) |
| F_1 | Magnification factor 1 for SECP solution for stress intensity factor |
| F_2 | Magnification factor 2 for SECP solution for stress intensity factor |
| F_3 | Magnification factor 3 for SECP solution for stress intensity factor |
| F_4 | Magnification factor 4 for SECP solution for stress intensity factor |
| G | Geometry correction factor for SECP solution for stress intensity factor |
| G_C | Critical energy release rate for Griffith crack criterion |
| I | Current flowing through equivalent circuit in complex notation |
| I | Amplitude of current pulse used to induce thermal fatigue |
| J^0 | Dissolution current density of the fresh surface at initial time in SDR model |
| $J_j, J_{ods,j}$ | Flux of j^{th} species in molten salt coolant or fuel |
| $K_I(a, \sigma)$ | Stress intensity factor |
| K_C | Threshold (critical) stress intensity factor for the initiation of mechanical fracture |
| K_{ISCC} | Threshold (critical) stress intensity factor for the initiation of SCC |
| $(K_I)_{SECP}$ | SECP solution for the stress intensity factor |
| N | Number of fatigue cycles |
| Q_f | Oxidation charge density between film-fracture events in SDR model |
| R_j | Homogeneous reaction rate for j^{th} species in molten salt coolant or fuel |
| $R_{ct,j}$ | Charge transfer resistance for j^{th} species |
| $R_{mt,c,j}$ | Mass transfer resistance for j^{th} species – cathodic reactant |

| | |
|--------------|--|
| $R_{mt,a,j}$ | Mass transfer resistance for j^{th} species – anodic reactant |
| R_p | Parallel resistance in equivalent circuit representing electrochemical cell |
| R_s | Series resistance in equivalent circuit representing electrochemical cell |
| R_w | Warburg resistance in equivalent circuit representing electrochemical cell |
| R_Ω | Electrolyte resistance in equivalent circuit representing electrochemical cell |
| M | Molecular weight of passive film in SDR model |
| MP | Melting point temperature |
| Nu_j | Dimensionless Nusselt number for mass transport of j^{th} species |
| Re | Dimensionless Reynolds number for molten salt coolant or fuel |
| Sc_j | Dimensionless Schmidt for mass transport of j^{th} species |
| T | Temperature |
| T_{MP} | Melting point temperature |
| V_{salt} | Volume of flowing molten salt making contact with corroding engine wall |
| V_t | Crack propagation rate |
| UTS | Ultimate tensile strength |
| Y | Complex admittance of equivalent circuit representing electrochemical cell |
| Z | Complex impedance of equivalent circuit representing electrochemical cell |
| Z_f | Faradaic component of the complex impedance |
| Z_{Im} | Imaginary part of the complex impedance |
| Z_{Re} | Real part of the complex impedance |
| Z_w | Warburg component of the complex impedance |
| a | Crack depth; flaw size |
| d | Equilibrium atomic spacing in 6-12 Leonard-Jones potential |

| | |
|---------------------|--|
| e | Modulation voltage across equivalent circuit in frequency domain |
| f | Normalized electrochemical constant (F/RT) |
| f | Frequency of modulation voltage applied to equivalent circuit |
| $f(a/w)$ | Geometric factor for calculating critical stress intensity factor |
| h | Thickness of single-edged cracked plate in stress intensity factor model |
| i | Current response flowing through equivalent circuit in frequency domain |
| i_j | Electrochemical current density for the j^{th} species |
| $i_{0,j}$ | Exchange current density for the j^{th} species in Tafel kinetic expression |
| $i_{l,c,j}$ | Cathodic limiting current density for reduction of the j^{th} species |
| $i_{l,a,j}$ | Anodic limiting current density for oxidation of the j^{th} species |
| $\langle i \rangle$ | Time average of the dissolution current density at crack tip in SDR model |
| $k_{0,j}$ | Kinetic rate constant for exchange current density for j^{th} species |
| $k_{f,j}$ | Forward kinetic rate constant for the j^{th} species |
| $k_{r,j}$ | Reverse kinetic rate constant for the j^{th} species |
| m | Exponent for stress intensity factor in crack propagation rate expression |
| m | Alternative variable representing mass density of molten salt |
| n | Parameter in SCC models that is dependent upon crack tip environment |
| n_s | Formation rate of slip steps in SDR model |
| $r_{corr,j}^0$ | Initial corrosion rate for j^{th} alloying constituent with no dissolved product |
| $r_{i,j}$ | Inner atomic separation on 6-12 Leonard-Jones Potential model |
| t | Time in corrosion model |
| t_0 | Initial time ($t=0$) in corrosion model |

| | |
|------------------------|---|
| u_j | Electrochemical mobility of the j^{th} species in the molten salt or fuel |
| v | Velocity of the molten salt or fuel |
| x | Depth of stress corrosion crack; penetration due to corrosion of LIFE engine wall |
| z_j | Electrons transferred in electrochemical reaction of j^{th} species |
| Φ | Electrochemical potential driving electromigration in transport model |
| $\Phi_{i,j}$ | 6-12 Leonard-Jones potential used in molecular dynamic simulations |
| α | Coefficient of thermal expansion |
| α_j | Tafel parameter for kinetic expression for j^{th} species |
| β | Time constant for exponential decay of repassivation current in SDR model |
| β | Factor in K_I expression dependent upon geometry of crack and component |
| ε | Well depth in the 6-12 Leonard-Jones potential model |
| ε_f | Rupture strain for passive film at crack tip in SDR model |
| $d\varepsilon_{ct}/dt$ | Crack tip strain rate |
| η_j | Electrochemical overpotential of the j^{th} species |
| γ_s | Specific surface energy where crack initiates |
| μ | Viscosity of the molten salt coolant or fuel |
| ϕ | Phase angle between modulation voltage and current in equivalent circuit |
| ν | Kinematic viscosity of the molten salt or coolant |
| ρ | Temperature-dependent electrical resistivity of ODS steel |
| ρ, ρ_f | Density of the passive oxide film in SDR model |
| ρ, ρ_{ods} | Density of ODS steel or other structural material |
| ρ, ρ_{salt} | Density of the molten salt or coolant |

| | |
|------------|--|
| σ | Parameter including diffusivities and used to define the Warburg impedance |
| σ | Applied or residual tensile stress driving SCC of engine wall |
| σ_c | Threshold (critical) value of applied stress for crack extension |
| ω | Angular velocity of rotating cylinder or rotating disk electrode |
| ω | Angular frequency ($2\pi f$) of modulation voltage applied to equivalent circuit |

Chapter A. LIFE Requirements for Materials

Mission

There are three primary missions for the LIFE engine, which include the burning of excess weapons-grade plutonium (WG-Pu), natural and depleted uranium (DU and HEU), and light-water reactor (LWR) spent nuclear fuel (SNF). WG-Pu and HEU can be incorporated into a solid fuel such as TRISO, or digested directly into a molten salt, thereby forming a high burn-up liquid fuel for the direct incineration of old weapons materials. Natural and depleted uranium (Nat-U and DU) can be incorporated into a variety of solid fuels including: TRI-structural ISO-tropic fuel (TRISO); baseball or solid hollow core (SHC); and inert matrix fuel (IMF). The LIFE engine enable the direct burning of such fuels with no isotopic enrichment or chemical separation, with the potential to attain very high burn-up, which is quantified in terms of fission of initial metal atoms (FIMA).

Tungsten First Wall

The high-energy (14 MeV) neutrons generated within the deuterium-tritium (DT) filled fusion targets will travel outward, first encountering a layer of solid tungsten armor supported by a low-activation ODS ferritic steel substrate. This “first wall” should be able to withstand bombardment by the hard-spectrum neutrons emitted by the target, as well as the high temperatures resulting from the absorption of X-rays that accompany the neutrons. The gas that fills the chamber is expected to offer protection from ions.

These materials will be subjected to a severe radiation and high-temperature environment. Energy from ICF target carried by: neutrons (14 MeV); Ions (< 100 keV); X-rays (< 100 keV); gamma ray contribution small. The target chamber and beam path will be filled with xenon gas at an atomic density of approximately $3 \times 10^{16} \text{ cm}^{-3}$. This gas absorbs a significant portion of the x-ray energy and stops all ions emitted from the indirect-drive target. The hot gas cools via radiation on a timescale sufficiently long to prevent damage to the tungsten first wall.

Neutron Multiplication Blanket

After passing through the tungsten first wall, the neutrons from the target will then enter a layer of beryllium which serves as a neutron multiplier. $\text{Be}(n,2n)\text{Be}$ reactions moderate their energy and generate approximately 2 neutrons for every one absorbed. The moderated and multiplied neutrons will then strike the next layer, a sub-critical fission blanket. The baseline fission fuel will be in the form of approximately 2-cm diameter pebbles containing a large number of smaller TRISO particles embedded in a graphite inert matrix. Other fuels are also being investigated with the objective of ultra-deep burn (99.9% FIMA).

Fission Blanket

An enhanced TRISO fuel particle with a more robust silicon carbide capsule than conventional fuel particles enables fission-gas containment at very high burn-up. This TRISO configuration is being considered as one possible high burn-up fuel option for the LIFE engine. The enhanced TRISO will have to endure more radiation damage than conventional TRISO fuels. The experience base for TRISO fuels is limited, with 8 to 20% FIMA demonstrated with low enriched uranium (LEU), and 79% FIMA demonstrated with highly enriched uranium (HEU) [Petti et al. 2004]. These LEU and HEU fuels experienced only approximately 3.5×10^{21} n/cm², but at a relatively high temperature of 1100 to 1200°C. In contrast, LIFE fuels will experience a much higher neutron dose of approximately 1.2×10^{23} n/cm², but at a much lower temperature of about 700°C. The temperature spike in the fuel pellets that result from the pulse of neutrons entering the fission blanket every 1/20th of a second is approximately 20°C.

Engine & Structural Materials

The fusion-fission chamber is the heart of the LIFE Engine, and is shown in Figure 1. The LIFE engine's structural challenges include: need for high-temperature strength; resistance to high-temperature creep; immunity to radiation damage, including swelling and helium embrittlement; resistance to corrosion and environmental cracking in high-temperature molten fluoride salts; and the ability to be fabricated into necessary shapes and configurations with practical welding processes. It is hoped that these challenges can be met with oxide dispersion strengthened (ODS) ferritic steels, sheets and coatings of refractory metals such as tungsten, advanced solid or liquid fuels, and other advanced reactor materials.

The operating windows for materials used to construct the LIFE engine are bounded by radiation embrittlement at lower temperatures, and by thermal creep at higher temperatures, as shown in Figure 2. The operating conditions for LIFE have been selected to enable the survivability of known materials of construction.

Molten Salt Coolant

Clad fuel pebbles formed from several thousand TRISO fuel particles, or an alternative solid fuel such as SHC or IMF are immersed in a molten fluoride salts that carries away heat to drive electrical generators. The very high volumetric heat capacities of these salts allow the fission blanket to be compact and have high power density when coupled to a point source of fusion neutrons (fusion target) [Sviatoslavsky et al. 2004]. Preferred coolants are FLIBE (Li₂BeF₄) in the primary coolant loop and FLINABE (LiNaBeF₄) in the secondary coolant loop. Note that FLIBE is a binary mixture of lithium and beryllium fluorides ($2\text{LiF} + \text{BeF}_2 = \text{Li}_2\text{BeF}_4$). The FLIBE input temperature is 620°C and the exit temperature for this design is 680°C. The transmutation of lithium in these coolants produces tritium for the steady stream of fusion targets that must be fed to the LIFE engine, thereby making the system self sufficient in tritium. Unfortunately, this reaction also produces very corrosive hydrofluoric acid species (HF and TF),

which can rapidly degrade structural and cladding materials. In the case of homogenous liquid fuels, UF₄ can be dissolved in these molten salt mixtures.

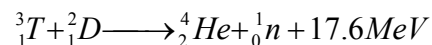
Chapter B. Summary of Existing Knowledge

Topical Report

This report is Volume 6 in a 12-volume series, and focuses on the corrosion and environmental cracking of ODS steel during exposure to high-temperature molten-salt coolants and fuels. Discussion includes: the electrochemical potential for reversible reactions; the mixed potential theory, which serves as the basis for predicting the open circuit corrosion potential, and for predicting the beneficial effects of sacrificial anodes; kinetic and mass-transport limited corrosion currents; corrosion rates, based upon corrosion currents; a model for solubility limited rates of corrosion in molten salts; the criterion for initiation of mechanical fracture; the criterion for initiation of stress corrosion cracks; and various methodologies for studying the corrosion of structural and cladding materials in high-temperature molten salt environments, including linear polarization, electrochemical impedance spectroscopy, corrosion penetration measurement with SEM, concentration profile determination with EDAX mapping, and current-induced thermal cycling for initiation of thermal and corrosion fatigue. The information discussed within this report was obtained from searches of the published scientific and technical literature, as well as searches of published United States patents pertaining to first-wall materials for fusion reactors. This report will be revised and updated in the future to provide additional information.

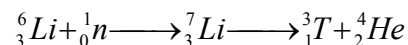
Nuclear Reactions

The neutrons for driving the sub-critical fission blanket are produced by implosion of the DT capsule in the inertial-confinement fusion (ICF) target in the center of the engine. The well-known D-T reaction in the target consumes tritium and deuterium:



The energy imparted to the neutron in the D-T reaction is approximately 14 MeV. This energy is sufficient to make the neutron relativistic [Equation 4.13, Foster & Wright 1973].

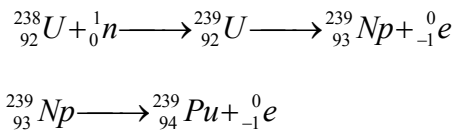
When the neutrons from the fusion target enter the coolant (or liquid fuel), they react with ⁶Li to produce ³T which can be separated, stored, and eventually fed back to the LIFE engine. The lithium transmutation reaction is [Equation 4.14, Foster & Wright 1973]:



Natural lithium consists of 92.58% ⁷Li and 7.42% ⁶Li. According to the published literature, natural lithium has an absorption cross-section for thermal neutrons of approximately 70b, while

${}^7\text{Li}$ has a neutron absorption cross-section of approximately 0.033b. The transmutation of ${}^6\text{Li}^+$ in the FLIBE produces ${}^3\text{T}^+$, which is very corrosive.

Approximately 99.3% of the world's natural uranium is ${}^{238}\text{U}$, which cannot be fissioned by thermal neutrons, but can be converted to fissile material with the fast neutrons produced in fusion-fission hybrids such as the LIFE engine. Fast (14 MeV) neutrons from the fusion targets will be used for the conversion of fertile nuclei (natural and depleted uranium, and spent light-water reactor fuel) via the following reactions [Equations 4.10a and 4.10b, Foster & Wright 1973]:



Neutron capture produces ${}^{239}\text{U}$, which decays to ${}^{239}\text{Np}$ by an initial beta emission, which in turn decays to ${}^{239}\text{Pu}$ by a second beta emission. Thus, the LIFE engine burns plutonium during most of its service period. In a similar manner, such hybrids can be used to support a thorium-based fuel cycle. Neutron capture converts ${}^{232}\text{Th}$ to ${}^{233}\text{Th}$, which decays to ${}^{233}\text{Pa}$ by an initial beta emission, which in turn decays to ${}^{233}\text{U}$ by a second beta emission.

Overview of Materials of Construction

Materials for fusion-fission hybrid reactors fall into several broad categories, including: (1) lasers and optics, (2) fusion targets, (3) tungsten first wall, (4) neutron multiplication blanket, (5) sub-critical fission blanket, (6) structural and cladding materials, (7) coolants and/or liquid fuels, (8) reflector, and (9) balance of plant. Issues related to lasers and optics, as well as fusion targets are discussed elsewhere. This collection of topical reports focuses on fission fuels, structural and first wall materials, the neutron multiplier, coolants and some special materials such as metal tritides required for the balance of plant. This report focuses on the interaction of (6) structural and cladding materials with (7) coolants and/or liquid fuels.

Tungsten First Wall

Tungsten-based alloys and materials are favored for use as the first wall in the LIFE Engine. United States Patent 7,128,980 discloses a novel tungsten-based composite for first-wall applications in fusion reactors. A layer of tungsten-based alloy is used to face the high-temperature plasma, exploiting the high-temperature refractory properties of the material, while copper alloys are used to enhance heat transfer. Specifically, this laminated composite consists of a plasma-facing area made of tungsten or a tungsten-based alloy (tungsten concentration greater than 90 weight %) and a heat-dissipating area made of copper or a copper-based alloy, with a thermal conductivity of at least 250 W/m-K, and a mean grain size of greater than 100 microns.

The regions separating the heat-resistant tungsten-alloy face and the heat-dissipating copper face is separated by a refractory-metal-copper composite; the refractory-metal-copper composite having a macroscopically uniform copper and tungsten concentration progression and a refractory metal concentration ranging from 10 to 40 volume % throughout material's thickness of 0.1 mm to 4 mm. The refractory metal phase forms a virtually continuous skeleton in this composite structure. Refractory-metal-copper composites with nearly continuous skeletons can also be produced by pressing powder mixtures or composite powders and sintering. Aside from W-Cu and Mo-Cu composites produced in this way, the use of rolled or extruded Mo-Cu composites has proven to be particularly advantageous.

Suitable tungsten materials for the plasma-facing segment are believed to include monocrystalline tungsten, pure tungsten, AKS (aluminum-potassium-silicate doped) tungsten, UHP (ultra-high-purity) tungsten, nanocrystalline tungsten, amorphous tungsten, ODS (oxide-dispersion-strengthened) tungsten, W-Re, ODS-W-Re and carbide-, nitride, or boride-precipitation-hardened tungsten alloys with preferred a carbide, nitride or boride concentration of between 0.05 and 1 vol. %. Segmentation of the tungsten/tungsten-alloy components is advantageous. As the crack propagation rate of the tungsten components is significantly higher in the direction of deformation than perpendicular to it, it may be advisable in the case of parts exposed to high levels of stress to produce the tungsten parts in such a way that the direction of deformation is perpendicular to the plasma-facing surface. In order to achieve sufficient structural stability and rigidity, a component consisting of a metallic material with strength of more than 300 MPa is bonded to the copper segment. Particularly suitable metallic materials include age-hardened Cu--Cr--Zr, and ODS-Cu materials as well as austenitic steels.

Neutron Multiplication Blanket

Current fusion reactor concepts consider the application of beryllium as neutron moderator and neutron multiplier [Ursu 1985, Section 12.5.3, p. 434]. The 14-MeV neutrons from the ICF target bombard beryllium in the neutron multiplication blanket where $\text{Be}(n,2n)\text{Be}$ reactions moderate their energy and generate approximately 2 neutrons for every one absorbed. Beryllium is one of the best solid moderators and is used either as metallic beryllium or as beryllium oxide. Beryllium has a low absorption cross section, a high scattering cross section, and a high melting point of 885°C (1158K). Beryllium is a light metal with an elastic modulus slightly superior to that of steel, and does not readily oxidize in air.

With the advent of fusion and fusion-fission reactors in the future, beryllium is expected to become an increasingly important material. Published estimates indicate that a fusion reactor generation capacity of one-million megawatts will require approximately 4.6×10^7 kilograms of beryllium. The availability of this strategic material is discussed by Shedd [2007], as well as in Volume 1 of these topical reports.

Beryllium is stable under the modest neutron irradiations that have been encountered in conventional nuclear systems, but may be problematic at the fluencies expected in the LIFE engine [Ursu 1985]. Its exposure to neutron fluencies up to 2.3×10^{21} n/cm² does not entail any sizeable dimensional change, nor does its electrical resistivity and corrosion resistance changes. As for the other properties, the thermal conductivity decreases slightly, the tensile strength increases from 500 MPa to about 714 MPa, whereas the elongation decreases from 1.4 to 0.3 percent. Notably, the hardness increases by about 30%. Also, the generation of helium as a result of irradiation causes beryllium to become brittle.

Beryllium and its salts, including FLIBE and FLINABE are considered very toxic and will have to be handled very carefully. Assuming an eight-hour work day, the maximum allowable concentration of beryllium aerosol in a fusion reactor facility should be no more than 2 micrograms per cubic meter. Exposure of the public should be no more than 0.01 micrograms per cubic meter.

Sub-Critical Fission Blanket

There are three primary missions for the LIFE engine, which include the burning of excess weapons-grade plutonium (WG-Pu), natural and depleted uranium (DU and HEU), and light-water reactor (LWR) spent nuclear fuel (SNF). WG-Pu and HEU can be digested directly into a molten salt, thereby forming a high burn-up liquid fuel for the direct incineration of old weapons materials. Natural and depleted uranium (Nat-U and DU) can be incorporated into a variety of solid fuels including: TRI-structural ISO-tropic fuel (TRISO); baseball or solid hollow core (SHC); and inert matrix fuel (IMF).

Commercial TRISO fuels use a mixed ceramic phase, uranium oxy-carbide (UOC), which appear to minimize thermal migration effects of the kernel. Ultimately, several different types of fertile and fissile materials could be used for fabrication of solid fuels for the LIFE engine. Ultimately, solid fission fuel for the engine could be fabricated from nitrides, oxides, carbides, oxycarbides, silicides, aluminides and metallic alloys. The LIFE engine enable the direct burning of such fuels with no isotopic enrichment or chemical separation, with the potential to attain very high burn-up, which is quantified in terms of fission of initial metal atoms (FIMA).

Structural and Cladding Materials

Metallic alloys that have been considered for structural components in various nuclear reactor applications include austenitic stainless steels, ferritic steels, and refractory metal alloys such as V-Cr-Ti, which are summarized in Table 1. The austenitic steels are prone to extreme swelling and high temperature thermal creep, as will be discussed subsequently. Ferritic steels show relatively little swelling during neutron irradiation, and can be enhanced by inclusion of a nano-dispersion of oxide particles. The refractory may be useful at higher temperatures than the levels that can be attained with austenitic and ferritic steels. Refractory metals are found in Groups IVB and VB of the periodic table, and include Nb, Ta, Cr, Mo, and W, as serve as the basis of

refractory alloys. Tungsten-based alloys and materials are frequently preferred for first-wall applications in fusion reactor designs.

Iron-Based and Nickel-Based Steels

The mechanical and corrosion performance, ease of fabrication, and relatively low cost of iron- and nickel-based steels make them logical choices for the fabrication of reactor structural components. The addition of refractory metals such chromium enhances high-temperature tensile strength, as well as corrosion resistance, though such performance is generally compromised by irradiation. The performance of iron and nickel based alloys in nuclear applications is discussed in substantial detail by Ursu [1985, Section 12.5.2, p. 441-445]. Insights from Ursu are summarized in several of the following paragraphs.

In the temperature range of 400-550°C, pearlitic-ferritic steels are frequently used. To extend the range of operating temperatures to 450-550°C, it is necessary to increase the chromium (Cr) content to 3-3.5 weight percent (3-3.5%). Carbide-forming elements such as molybdenum, tungsten, and vanadium (Mo, W, and V) are also beneficial for extending the range of operating temperature. These steels are said to behave acceptably with hydrogen within this range of temperatures. Ferritic stainless steels are chromium-containing alloys with body-centered cubic (bcc) crystal structures [Davis 1995]. Chromium content is usually in the range of 10.5-30 weight percent (10.5-30%). Some grades contain molybdenum, silicon, aluminum, titanium, or niobium (Mo, Si, Al, Ti, or Nb) to confer particular characteristics. These alloys have good ductility and formability, but high-temperature strengths are relatively poor compared to those of austenitic grades. Toughness may be somewhat limited at low temperatures in heavy sections.

Annealed ferritic stainless steels usually have yield and tensile strengths of 240-380 MPa (35-55 ksi) and 415-585 MPa (60-85 ksi), respectively. Ductilities tend to range from 20 to 35 percent. More highly alloyed ferritic stainless steels may have yield and tensile strengths as high as 515 MPa (75 ksi) and 655 MPa (95 ksi), respectively. These alloys are not strengthened by heat treatment or cold working. The strain-hardening rates of ferrite are relatively low and cold work lowers ductility.

Ferritic steels are favored for nuclear applications since they swell relatively little after exposure to high neutron doses. Irradiation with heavy ion beams is used to simulate the effects of neutron bombardment, and to perform accelerated testing for high fluence applications [Farrell and Lee 1986].

Whereas martensitic stainless steels offer only moderate corrosion resistance, that of ferritic stainless steels can range from moderate for lower alloyed grades, to outstanding for more highly alloyed grades. Typical applications for ferritic stainless steels include equipment for handling oxidizing and organic acids, food processing equipment, and heat exchangers and piping used in seawater.

To enable operation at higher temperatures, in the 500-600°C range, additional chromium is required. Chromium additions of 5-15 weight percent (5-15%) increase the re-crystallization temperature and prevent plastic deformation. For example, enhanced steels with 12 weight percent chromium (12% Cr) have been shown to behave well at an applied stress of 200 MPa and a temperature of 500°C for 10,000 hours. At the upper limit of this temperature range, molybdenum, tungsten, vanadium and niobium (Mo, W, V or Nb) are needed.

Austenitic steel with 18% Cr, 9% Ni and 1% Ti, with carbides, have been shown to be capable of withstanding an applied stress of 200 MPa at 630°C for 10,000 hour. Nickel alloys can be used as structural materials at temperatures up to 700°C, nickel-cobalt alloys can be used up to 800°C, and chromium alloys can be used up to 1100°C. Unfortunately, austenitic alloys undergo significant swelling during neutron irradiation. The effects of irradiation on nickel alloys are discussed by Makenas et al. [1986] and Angeliu et al. [2007].

Refractory steels are used in the temperature range 900-1200°C, but cannot serve reinforcement purposes. Their strength depends upon temperature and increases with the rise in Cr concentration.

Oxide Dispersion Strengthened (ODS) Ferritic Steels

New oxide dispersion strengthened (ODS) ferritic-martensitic (FM) steels have been developed specifically for a variety of nuclear applications, including cladding for fuel in fast reactors. These alloys exploit the ability of the ferritic matrix to withstand extreme neutron irradiation with relatively little swelling. Oxide dispersion strengthening with Y_2O_3 or TiO_2 nanoparticles enhances tensile strength and creep resistance at high temperature [Allen et al. 2005]. These alloys are therefore considered to be good candidates for construction of structural components of the LIFE engine.

The ODS FM steels known as Kobe 12YWT and 9Cr-ODS have demonstrated exceptional tensile strength and creep resistance at relatively high temperature, as shown in Figures 3 and 4 [Ukai and Fujiwara 2002; Klueh et al. 2007]. The yield strengths and elongations as functions of test temperature for several additional ODS steels, including as-received EUROFER 97, CRPP ODS EUROFER97 with 0.3 wt. % Y_2O_3 and CRPP ODS EUROFER97 with 0.3 wt. % Y_2O_3 and 0.3 wt. % TiO_2 are given by Schaublin et al. [2006].

Given the thermal pulsing of the LIFE Engine, the resistance of materials of construction to thermal fatigue is also of interest. ODS FM steels appear to have much longer fatigue life than conventional ferritic steels such as modified 9Cr-1Mo steels. Predictions as shown in Figure 5 are based upon regression analysis of data for $N_f < 100,000$ cycles [Ukai and Ohtsuka 2007]. Strain-controlled low-cycle fatigue tests were conducted for 9Cr-ODS and 12Cr-ODS at 873-1023K. The total strain ranges were controlled from 0.5 to 1.5% with a strain rate of 0.1% per second. Corresponding plastic strain ranged from 0.01 to 1%. The ODS has longer fatigue life

than modified 9Cr-1Mo ferritic steel. The oxide dispersion strengthening prevented softening or hardening during cycling.

Alternatives to Steel

An outstanding critical analysis of the operating temperature windows for nine candidate structural materials for fusion reactors has been performed [Zinkle et al. 2000-2008]. These include: four reduced-activation structural materials (oxide-dispersion-strengthened and ferritic/martensitic steels containing 8-12%Cr, V-4Cr-4Ti, and SiC/SiC composites), copper-base alloys (CuNiBe), tantalum-base alloys (e.g. Ta-8W-2Hf), niobium alloys (99Nb-1Zr), and molybdenum and tungsten alloys. The results are compared with the operating temperature limits for Type 316 austenitic stainless steel. Several factors define the allowable operating temperature window for structural alloys in a fusion reactor. The lower operating temperature limit in all body-centered cubic (bcc) and most face-centered cubic (fcc) alloys is determined by radiation embrittlement (decrease in fracture toughness), which is generally most pronounced for irradiation temperatures below similar to $0.3 T_{MP}$ where T_{MP} is the melting temperature. The lower operating temperature limit for SiC/SiC composites will likely be determined by radiation-induced thermal conductivity degradation, which becomes more pronounced in ceramics with decreasing temperature.

Vanadium Alloys

Vanadium alloys have been investigated for structural and first-wall applications in fusion reactors [Smith et al. 2000]. Insights from Smith et al. are summarized in this section. These refractory alloys provide favorable safety and environmental features such as low long-term activation, low decay heat and contact dose, and the potential for recycle. Vanadium alloys discussed by these investigators cover a broad range of compositions, V-(0-15)%Cr-(1-20)%Ti-(0-1)%Si, with particular emphasis given to a reference alloy, V-4Cr-4Ti. The three key alloying elements, vanadium, chromium and titanium, are mutually soluble in each other at elevated temperatures, and they all exhibit favorable low-activation characteristics.

Vanadium alloys with a few percent titanium are resistant to irradiation-induced swelling and embrittlement at projected operating temperatures, and are believed to be compatible with liquid-metal blankets/coolants. Helium and hydrogen transmutation rates in vanadium alloys are substantially less than those for other candidate materials exposed to high-energy neutrons characteristic of deuterium-tritium plasmas. Irradiation does harden the materials. For example, the yield stress of V-4Cr-Ti increases from the pre-irradiation level of 200-300 MPa to 600-700 MPa at a damage level of approximately 30 dpa, and temperatures of 430 to 600°C.

The primary thermo-mechanical treatment of these alloys is a solution anneal at approximately 1000°C for one hour. Properties are relatively insensitive to annealing conditions for 950-1100°C for 0.5-2 hours. Thermal aging at temperatures ranging from 500 to 1000C, for exposure times up to 5000 hours, show no significant grain growth (grain size $20 \pm 2 \mu\text{m}$). In summary,

candidate vanadium alloys exhibit good resistance to irradiation damage at temperatures of interest and offer a potential for long operating lifetime.

Other important physical properties of these candidate materials are summarized in Table 2 [Smith et al. 2000]. In particular, the coefficient of thermal expansion of V-Cr-Ti is lower than that of austenitic and ferritic steels, which would help alleviate thermal stress and associated environmental cracking, and the thermal conductivity is significantly higher, which would help alleviate concerns regarding heat transfer. This could make these materials good choices in applications where thermal pulsing is determined to be problematic.

Molybdenum Alloys

Molybdenum alloy with small additions of titanium, zirconium and carbon, such as 99.4%Mo-0.5%Ti-0.08%Zr-0.01%C, have good strain endurance and fracture toughness at high temperature. However, their susceptibility to oxidation requires that they be coated with thermal-spray coatings of Si-Al-Co. Other cladding is also possible. Additions of rhenium have been used to improve the ductility and fabricability of molybdenum alloys. Specific Re-containing molybdenum alloys that have been developed include: Mo-7Re (13 wt. % Re); Mo-27Re (42 wt. % Re); and Mo-30Re (45 wt. % Re). After neutron irradiation of Mo-27Re and Mo-30Re at 750 to 1075°C, MoRe₃ (Chi phase) precipitates formed at grain boundaries and on the surface at a damage level of 1.5 dpa; these precipitates were not observed in Mo-7Re [Ursu 1985]. Neutron activation may also pose challenges.

Niobium Alloys

These materials also have good strain endurance and fracture toughness. Some of the best tensile properties obtained with niobium-based alloys have been reported with: (1) Nb-15%W-3%Ti-1%Zr and (2) Nb-10%-3%Ti-1%Zr. Titanium additions have enhanced the hardness of these alloys, and have improved their refractory properties, allowing them to operate at temperatures as high as 1300°C. These materials tend to have better ductility than Mo alloys. Furthermore, these materials can be prepared using cold and hot pressing. Argon arc welding is possible. Coatings of silicon have been used to prevent high temperature oxidation [Ursu 1985].

Other Advanced Materials of Interest

Other approaches to dispersion-strengthening also exist, such as thermomechanical treatment (TMT). The microstructure of 9-12% Cr steels has been improved dramatically with hot rolling, which has become known as thermomechanical treatment (TMT). TMT has been used to process 9Cr-1Mo and 12 Cr steels, thereby forming precipitates at dislocations, as shown in Figure 37. Dispersions of precipitates produced with TMT are much finer than those observed in conventionally processed 9-12 Cr steels, and mechanical properties are substantially improved. [Klueh et al. 2005 & 2007].

The LIFE engine will push crystalline engineering materials to their limits of radiation tolerance. The intense neutron bombardment will displace atoms from lattice sites numerous times, and may eventually convert crystalline materials into an amorphous state, with substantial helium and hydrogen implantation. Since a completely amorphous material may evolve at the extremes of neutron bombardment, the search for any new solid-phase material with immunity to extreme neutron irradiation should include amorphous materials (expected end state). Neutron bombardment would not displace atoms from lattice sites since none exist. The challenge in the development of radiation tolerant amorphous metals will be the attainment of high fracture toughness, and incorporation of features that enable either trapping of large quantities of helium and hydrogen, or that enable the rapid transport of these species out of the matrix.

In addition to the possible application as radiation-tolerant structures, amorphous materials may also have other important applications in the LIFE engine. For example, the high boron content of $\text{Fe}_{49.7}\text{Cr}_{17.7}\text{Mn}_{1.9}\text{Mo}_{7.4}\text{W}_{1.6}\text{B}_{15.2}\text{C}_{3.8}\text{Si}_{2.4}$ (SAM2X5) makes it an extremely effective neutron absorber for thermal neutrons, and suitable for criticality control applications [Farmer et al. 2007-2008]. Other yttrium-containing amorphous metals such as SAM1651 could be optimized for the absorption of fast neutrons by substituting Gd for Y or other alloying constituents, and should be explored for LIFE shielding.

Average measured values of the neutron absorption cross section in transmission (Σ_t) for Type 316L stainless steel, Alloy C-22, borated stainless steel, a Ni-Cr-Mo-Gd alloy, and SAM2X5 have been determined to be approximately 1.1, 1.3, 2.3, 3.8 and 7.1, respectively. This material and its parent alloy have been shown to maintain corrosion resistance up to the glass transition temperature, and to remain in the amorphous state after receiving relatively high neutron dose.

Materials used in criticality control applications must be relatively stable during irradiation with thermal neutrons. Melt-spun ribbon samples of various iron-based amorphous metals were subjected to high neutron dose in the 1.5 MW TRIGA reactor at McClellan Nuclear Radiation Center (MNRC) [22]. The neutron flux was $1.6 \times 10^{10} \text{ n cm}^{-2} \text{ sec}^{-1}$. Samples were irradiated for three different times: duration of 1st irradiation was 44 minutes; duration of 2nd irradiation was 132 minutes; and duration of 3rd irradiation was 263 minutes. The corresponding neutron doses were: $4.3 \times 10^{13} \text{ n cm}^{-2}$, $1.3 \times 10^{14} \text{ n cm}^{-2} \text{ sec}^{-1}$ and $2.6 \times 10^{14} \text{ n cm}^{-2}$, respectively. These doses are equivalent to approximately 670, 2000 and 4000 years inside the waste packages designed for emplacement at Yucca Mountain. An exposure corresponding to a 4000-year service life does not cause any detectable, deleterious phase transformations. Additional phase stability studies would be required before the materials could be used for LIFE engine applications.

Corrosive Environments

Molten Salt Coolants

High-temperature liquid-phase coolants appropriate for heat transfer in nuclear power systems such as the LIFE engine fall into two broad categories, liquid metals and molten salts [Grimes

and Cantor 1972]. Liquid metal include Hg, Na, K, Pb, Bi, Pb-Bi, Sn, Li, Li-Al, Pb-Li, Sn-Li, and others. Molten salts include FLIBE ($2\text{LiF} + \text{BeF}_2 = \text{Li}_2\text{BeF}_4$), FLINABE ($\text{LiF} + \text{NaF} + \text{BeF}_2 = \text{LiNaBeF}_4$), FLINAK ($\text{LiF} + \text{NaF} + \text{KF}$) and others (for example, $^{24}\text{NaBF}_4 + ^{24}\text{NaF}$). FLIBE has been proposed for use in the primary coolant loop of the LIFE engine, while beryllium-free FLINAK has been proposed for use in the secondary loop. The lithium in the primary loop coolant will enable tritium breeding, while the beryllium helps moderate neutrons.

Molten salt coolants are less prone to catch fire than the liquid metal coolants, and can be used to breed tritium via the transmutation of lithium. A binary mixture of BeF_2 and LiF produces the eutectic composition Li_2BeF_4 , which has a relatively low melting point of less than 400°C , as shown in Figure 6. The formula weight, density, melting point and boiling point of several of these candidates are summarized in Table 2 [Williams et al. 2006; Moir et al. 1985; Foster & Wright 1973; Rosenthal et al. 1971]. Pure FLIBE has relatively low viscosity, comparable to kerosene at ambient temperature, and therefore would be expected to flow well.

Note that several other programs have investigated the use of molten fluoride salts. FLIBE is considered as a candidate material for tritium breeding in a fusion liquid due to its chemical stability and low electrical conductivity. The *Jupiter-II Irradiation Tests for Fusion Research* also focused on the use of FLIBE [Petti et al. 2006]. It was selected for the conceptual design of the *Force Free Helical Reactor (FFHR)*. The tritium release behavior and the corrosion of the structural materials by FLIBE were key to success in this application. In this particular design, a ferritic steel (Fe-9Cr-2W) and a vanadium alloy (V-4Cr-4Ti) are the candidate materials for the blanket structure [Nishimura et al. 2001].

Investigators at the University of Tokyo (YAYOI) placed a Monel crucible with 100 to 300 grams of FLIBE in a fast-neutron reactor and heated the salt to 873K [Nishimura et al. 2001]. The neutron flux during these irradiations was 10^8 to 10^9 n cm^{-2} sec. At hydrogen partial pressures above 1000 Pa, the primary tritium-bearing species responsible for tritium release is gaseous diatomic HT. These investigators determined the normalized release rates for tritium in flowing stream of helium purge gas with various concentrations of hydrogen. The normalized tritium release rate dropped dramatically below hydrogen partial pressures of 1000 Pa. Steady state was achieved after approximately 120 to 140 minutes of purging.

Unfortunately, the transmutation of lithium in this coolant produces very corrosive tritium fluoride species (TF), which behaves like hydrofluoric acid and can rapidly degrade structural materials. Thermal neutrons react with Li^+ and convert it to T^+ , which then reacts with fluoride anions to form gaseous TF. Exchange reactions between tritons (T^+) and diatomic hydrogen (H_2) formed protons (H^+) and diatomic HT. The corrosion of structural components of the LIFE engine in contact with this coolant must be understood.

It may be possible to control the release of tritium from the FLIBE blanket through the manipulation of electrochemical oxidation and reduction reactions, using an on-line electrolytic

cell. The reduction of tritons (T^+) in such a cell would simultaneously remove the threat of acidic TF, while enabling the extraction of tritium from the salt for storage in solid-state media.

Liquid Fuels & Continuous On-Line Reprocessing

If a homogenous liquid fuel is desired, fertile/fissile materials can be dissolved in these molten salt mixtures. Unlike solid fuels, molten salts with dissolved uranium, thorium and plutonium will not be structurally damaged by long-term exposure to neutron bombardment. From a purely technical point of view, such liquid fuels might therefore serve as ideal fuels for achieving nearly complete burn-up. Such molten salt fuels have been considered for graphite-moderated molten-salt breeder reactors that operate on the thorium-uranium fuel cycle, and enable continuous reprocessing of the fuel. Unfortunately, continuous on-line reprocessing is required to keep fission products at desirable levels. A widely referenced fuel salt consists of Li_2BeF_4 (FLIBE) with dissolved fissile UF_4 and a blanket salt consisting of Li_2BeF_4 with dissolved fertile ThF_4 . These conceptual designs assumed that $NaBF_4$ and NaF_2 would be used as secondary loop coolants. FLINABE and FLINAK based systems are also possible.

These liquid-phase solutions are very complex. In-depth understanding must be developed through application of internationally accepted predictive codes such as THERMOCALC to predict the formation of various phases, including precipitates such as plutonium trifluoride (PuF_3). The prediction of phase diagrams for complex liquid fuels, with large numbers of fission products, requires that the phase diagrams for several binary pairs of salts first be developed. For example, equilibrium phase diagrams have already been predicted for: BeF_2 - LiF (FLIBE), BeF_2 - ThF_4 , BeF_2 - UF_4 , BeF_2 - ZrF_4 , LiF - PuF_3 , LiF - ThF_4 , LiF - ZrF_4 , ThF_4 - UF_4 and several other systems. The LIFE Project has recently predicted a phase diagram for the most basic FLIBE-based liquid fuel, assumed to consist primarily of lithium, beryllium, uranium and plutonium fluorides. This phase diagram is shown in Figure 7, and reveals regions of stable operation for such liquid fuels. Such systems would have to be operated at compositions and temperatures where no solid-phase precipitates form. Other continuous molten-salt processing schemes are reviewed elsewhere by Farmer, Shaw, Moir and Halsey [2008].

Much of our practical knowledge pertaining to liquid fuel comes from the development of the molten salt breeder reactor (MSBR) [Haubenreich & Engel 1970; Foster & Wright 1973]. The MSBR concept depends upon molten fluoride salts containing 7LiF , BeF_2 , ThF_4 and $^{233}UF_4$ being pumped through a graphite moderated core where heat released by fission will raise the salt temperature to $700^\circ C$ ($\sim 1300^\circ F$), close to the operating temperature of the LIFE engine. The heated salt then passes through an intermediate heat exchanger where its enthalpy is reduced by transfer of heat to a secondary salt, sodium fluoroborate, which in turn may transfer energy to steam at 3500 psia and $540^\circ C$ ($\sim 1000^\circ F$).

Initially, a two-salt MSBR design was favored, with a fuel salt containing only fissile UF_4 and no fertile ThF_4 , and a blanket salt containing only ThF_4 and no UF_4 . The fuel and blanket salts were

passed in close proximity to one another inside a graphite moderator block, where uranium-233 was bred from thorium. Unfortunately, problems due to dimensional instability of the graphite moderator block after long-term neutron irradiation were encountered.

In the case of the two-salt MSBR, a relatively simple on-line fuel reprocessing plant was enabled by the physical separation of fissile and bred uranium in the graphite moderator block [Figure 13.31, Foster & Wright 1973]. In the conceptual on-line salt reprocessing plant, fuel salt was to be fluorinated to convert dissolved UF_4 to gaseous UF_6 , thereby allowing uranium separation from the liquid stream. The remaining salt was to be separated from rare earth and other fission products by vacuum distillation. Approximately 5% of the fuel salt was to be discarded in this process, with the need for LiF and BeF_2 makeup. In contrast, the blanket salt was to be fluorinated primarily for the removal of bred uranium from the fertile thorium. Approximately 5% of the blanket salt would have also been discarded in this process, with the need for LiF, BeF_2 and ThF_4 makeup. The total salt leaving the loop would have been approximately 8%. LIFE engines with liquid fuels will require continuous removal of rare earth fission products to prevent PuF_3 precipitation, and will require much more efficient on-line separation processes.

A reactor design with a single-salt two-region core and an easily replaceable graphite core assembly evolved, due to the problems anticipated with dimensional stability of the graphite in the two-salt design. This design eliminated the need for complicated flow paths inside the moderator block. The value of k_∞ was found to peak at approximately 4% salt content and drop to below unity at approximately 18% salt content. It was found that a core with 13% salt content would be critical with k_∞ of 1.034, while a reflector region having less than 37% salt content would be sub-critical with k_∞ of 0.392. A breeding ratio of 1.07 to 1.08 was predicted for such a system with low fuel costs and small fuel inventories.

In the conceptual MSBR, the strong neutron capture of protactinium-233 ($\sigma_a = 43\text{b}$) in the core of the core leads to the production of protactinium-234, which in turn would decay to non-fissionable uranium-234. It is therefore necessary to remove ^{233}Pa (27.4-day half life) from the core so that it has time to decay to fissionable ^{233}U . A liquid-to-liquid extraction process may be the best means for separating protactinium and uranium from the molten salt. An electrolysis process is then used to selectively recycle the uranium from salt in the decay tank to the MSBR fuel salt. Residual protactinium is then trapped in solidified salt for discarding.

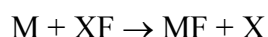
The removal of noble gases such as xenon from the core of the MSBR is also essential for efficient breeding. Specifically, helium purging is used to remove xenon-135 ($\sigma_a = 2.72 \times 10^6\text{b}$), reducing the concentration of this gaseous fission poison by an order-of-magnitude ($\times 10$).

Corrosive Attack of Engine Materials

Corrosion Mechanisms

The steels used for construction of the LIFE engine must be able to withstand high temperatures without melting or excessive thermal creep. Chromium has been added to many of the structural steels of interest to enhance high temperature mechanical properties, as well as oxidation and corrosion resistance in molten Li_2BeF_4 and other such coolants. An alloy 0.35 to 0.45% for carbon, 2 to 3% for silicon, and 8 to 10% for chromium is suggested for operation at 850°C, close to the current design temperature of the LIFE Engine. The concentration of chromium in the ODS FM steels proposed for construction of the LIFE Engine fall within the recommended range.

The corrosion of structural materials are due to the oxidative dissolution of reduced alloy constituents (M) with the high-temperature molten fluoride salt (XF), as described by Cheng et al. [2003]:



In this reaction, X represents lithium, sodium, beryllium, or transmutation products, such as tritium. The transmutation of lithium produces hydrogen isotopes which react with free fluoride to form acid (HF, for example), making the blanket and coolant much more corrosive than it would otherwise be.

The relative corrosion susceptibility of refractory metals and Fe-Cr steels can be understood by ranking the free energies of formation for their respective fluoride salts, as done in Table 3 [Cheng et al. 2003]. The transmutation of lithium in the Li_2BeF_4 forms corrosive tritium fluoride, which behaves chemically like hydrogen fluoride, or hydrofluoric acid. The ultimate selection of materials for long-term containment such corrosive transmutation products in fluid pumping loops requires the use of alloy systems with constituents that form fluoride salts less thermodynamically stable than hydrogen fluoride. It is therefore useful to rank candidate alloying constituents based upon the free energies of formation of their respective fluoride salts, each with the units of kilocalories per gram mole of fluoride at 1000 Kelvin. Such a ranking reveals that MoF_6 , WF_6 , NiF_2 , VF_5 , VF_4 have less negative free energies than that of HF, indicating acceptability of Mo, W, Ni, and V, while FeF_2 has a free energy comparable to HF, indicating marginal acceptability of Fe-based alloys. Chromium has more negative free energy, which explains the dissolution of chromium by such fluoride salts, and the formation of the well-known chromium depletion layer. Some refractory materials such as Nb-based and Ta-based alloys would be expected to be unacceptable for long-term exposure in high-temperature fluoride salts. Note that metallic beryllium (the proposed neutron multiplier in LIFE engine) would be expected to undergo dissolution in Li_2BeF_4 , especially with galvanic coupling to more noble materials such as Mo-, W-, Ni-, V- and Fe-based alloys.

As previously discussed, molten salts used as blankets/coolants in fusion-fission hybrid reactors become extremely corrosive through the transmutation of lithium in the blanket/coolant, which results in the formation of hydrofluoric acid species (HF and TF). The corrosion mechanisms of steels and refractory alloys in these electrolytes are not yet completely understood, however, reasonable assumptions can be made based upon published experimental data. Corrosion may be controlled by manipulation of the oxidation potential, but it is expected that vigilant control would be required.

The postulated corrosion mechanisms for steels in molten fluoride salts are very complicated and are illustrated in Figure 8. The anodic process will involve the oxidative dissolution of metallic elements in the structural material, thereby forming dissolved metal cations. In the absence of oxygen, electrons generated by the anodic oxidation of the structural material must be consumed by some other electrochemical reduction process. Based upon published information, it is assumed that this cathodic reaction will involve reduction of H^+ and T^+ cations and the formation of gaseous hydrogen (H_2), deuterium (D_2), tritium (T_2) and other dimmer species formed from the three hydrogen isotopes. This reduction will liberate fluoride anions (F^-) which will then form ion pairs with dissolved metal cations produced by the anodic dissolution of metallic elements from the structural materials. Some of these metal fluoride salts will be in thermochemical equilibrium with volatile metal fluoride species. The high ionic strength of the molten salt makes it a highly conductive supporting electrolyte for corrosion reactions.

The published results of thermochemical simulation with the MALT2 database and the GEM code have provided valuable insight into the corrosion ferritic stainless steel and vanadium-based alloys in FLIBE [Nishimura et al. 2001]. Chemical species predicted to form in the gas phase include: $(H,T)_2$, $(H,T)F$, $((H,T)F)_2$, $(H,T)_2O$, $Be(H,T)_2$, BeF_2 , $LiBeF_3$ and FeF_3 . Chemical species predicted to form in the condensed liquid phase due to the corrosion of ferritic stainless steel include: Fe, Cr, Fe_3W_2 , Cr_2O_3 , CrF_2 , CrF_3 , BeO, Li_2BeF_4 and $LiBeF_3$.

Experimental observations of the corroded surface were made with X-ray diffraction (XRD), Rutherford backscattering (RBS) and Moessbauer Spectroscopy have provided additional insight. The existence of α -Fe, Fe_2O_3 and spinel phases on the surface were detected with XRD. The formation of the chromium depletion layer after a 3-day immersion in the molten salt was found with Moessbauer Spectroscopy. Trivalent iron was also detected, suggesting the formation of Fe_2O_3 . Rutherford backscattering (RBS) was used to measure the thickness of the oxygen penetration layer, which was found to be 200 nanometers.

These data indicate that the Cr_2O_3 film provides only limited corrosion protection. The preferential dissolution of chromium into the Li_2Be_4 salt results in the formation of a chromium depletion layer, which lies below a mixed oxide film of $Fe(Fe,Cr)_2O_4$ and disperse deposit of Fe_2O_3 particles. Dissolution and fluorination of iron leads to the formation of the volatile FeF_3 species. The formation of this volatile iron species can be suppressed by increasing the partial pressure of hydrogen partial pressure in the system. While the presence of metallic beryllium has

a positive effect on the formation of corrosive HF (TF), it promotes formation of problematic gaseous BeH₂.

The transmutation of lithium in the Li₂BeF₄ salt leads to the formation of acidic tritium fluoride, which has the chemical behavior of hydrofluoric acid, as previously discussed. The reduction of T⁺ at the ODS-salt interface may lead to the formation of reduced T₂, with the simultaneous oxidation of Fe and Cr in the alloy to form Cr⁺³ and Fe⁺². Atomic tritium adsorbed on the surface of the ODS steel could be absorbed by the steel, which could lead to tritium (hydrogen) induced cracking. The presence of metallic beryllium is predicted to suppress the formation of HF (TF).

Cathodic tritium charging forms adsorbed tritium adatoms on the surface of the ODS FM steel. These tritium adatoms can recombine at the surface and form gaseous diatomic tritium. Alternatively, these adatoms may be absorbed into the bulk material and cause embrittlement and cracking, a situation that can be worsened by any dissolved species that might serve as a recombination poison. The mechanism would be analogous to that of hydrogen induced cracking (HIC). In many metals, such as titanium, infused hydrogen diffuses up stress gradients to crack tips, forming brittle hydride phases. These brittle hydride phases periodically rupture under the stress at the crack tip, and enable crack propagation through the classical film rupture mechanism.

Furthermore, hydrogen isotopes absorbed by the bulk material may reduce oxide dispersion strengthening particles, further compromising high-temperature and radiation-tolerant mechanical properties. The possible reduction of oxide dispersion strengthening agents by absorbed hydrogen isotopes deserves further attention.

The localized corrosion, specifically the pitting of steels and refractory alloys has been reported in FLIBE molten salts. Pitting of alloys is frequently associated with the localized destabilization of passive films with halide anions, such as fluoride, the reaction of such halide anions with relatively soluble inclusions in the alloy surface, or the localized reaction of such aggressive anions with specific active sites on the surface of an immune metal. In all cases, a threshold electrochemical potential exists, above which localized attack can occur.

In experimental studies with vanadium, pits with diameters of approximately 200 microns were observed. After 10-day immersions, the alloy became brittle. X-ray diffraction did not show the formation of VF₂, VOF, or VO, which could have formed protective scales, but were not observed to do so. FLIBE is a very stable molten salt, however, under irradiation it forms acidic HF and TF, and causes severe corrosion of structural materials, including ferritic steels (specifically, Fe-9Cr-2W) and vanadium alloys (specifically, V-4Cr-4Ti). This does not necessarily rule out the design and fabrication of other high-performance ferritic and refractory alloys that could perform well in such environments. Alloys with elements forming less volatile fluoride species would be particularly interesting. Other pertinent corrosion studies have also been performed [Indacoechea et al. 1999].

Corrosion Models

A wide range of vapor and aqueous phase corrosion models have been reviewed and documented by Farmer et al. [1991]. For example, crevice corrosion can occur in conventional light-water reactors, which leads to dramatic lowering of pH inside the crevice due to the hydrolysis of dissolved metal cations. Halide ions are simultaneously driven into the crevice by the potential difference that exists between the cathode at the crevice mouth, and the anode deep within the crevice. Low pH and high chloride ion concentration inside the crevice lead to accelerated corrosive attack, including other modes of localized attack such as pitting. Localized corrosion models include several for pit initiation: the halide nuclei theory; the point-defect model; and the stochastic probability model. Transport-limited models for the propagation pits are also reviewed, including cases where the growth of a hemispherical pit is limited by the presence of a salt film. The possibility of initiating a corrosion fatigue crack at pits is discussed, where the pit is considered to be a surface flaw. Models for initiation and propagation stress corrosion cracks via brittle film fracture at the crack tip are reviewed, and include the film rupture and slip dissolution models. Cases where the propagation of cracks is controlled by anodic dissolution at the tip, and assumed to be mass-transport limited are also considered. While relatively few fundamental corrosion models have been successfully applied to the corrosive molten salt environment inside nuclear reaction systems, the possibility exists to do so. The successful corrosion engineering of the LIFE engine will make such extensions of corrosion science essential.

Tafel Kinetics Applied to Anodic and Reactions

Most theoretical discussions of corrosion based in mathematics begin with a review of Tafel kinetics. The electrochemical current density i_j , for a given oxidation-reduction couple consists of one term representing the reduction of the oxidized form of the species $C_{O,j}(0,t)$, and a second term representing the oxidation of the reduced form of the species $C_{R,j}(0,t)$ [Bard & Faulkner 1980, Chapter 3]:

$$i_j = z_j F A k_{0,j} \left[C_{O,j}(0,t) e^{-\alpha_j z_j f (E - E_j^0)} - C_{R,j}(0,t) e^{(1-\alpha_j) z_j f (E - E_j^0)} \right]$$

The forward and reverse rate constants $k_{f,j}$ and $k_{r,j}$, are related to a single rate constant $k_{0,j}$ by the two following expressions:

$$k_{f,j} = k_{0,j} e^{-\alpha_j z_j f (E - E_j^0)}$$

$$k_{r,j} = k_{0,j} e^{(1-\alpha_j) z_j f (E - E_j^0)}$$

Linus Pauling [1970] defines the electrochemical potential is defined in terms of the Gibbs free energy for the reaction with Equation 15-15 in his classic text on general chemistry:

$$E_j^0 = -\frac{\Delta G_j^0}{z_j F}$$

The Tafel parameter is approximately 0.5 in cases where the activation barrier is symmetrical.

$$\alpha_j \approx 0.5$$

Faraday's constant, the universal gas constant, and the absolute temperature are combined in a single parameter (f) for simplification.

$$f = \frac{F}{RT}$$

The overpotential (η_j) is linearly related to natural or base-ten logarithms of the cathodic current density:

$$\eta_j = \frac{RT}{\alpha_j z_j F} \ln t_0 - \frac{RT}{\alpha_j z_j F} \ln i_j$$

$$\log \frac{i_j}{1 - e^{z_j f \eta_j}} = \log i_{0,j} - \frac{\alpha_j z_j F \eta_j}{2.3 RT}$$

Effects of Mass Transport on Rate of Corrosion

The electrochemical current density and the mass transport flux for the j^{th} species are related. The flux consists of an electromigration term, which is driven by the local electric field, a diffusive flux term, which is proportional to the diffusivity, and a convective transport term, which is a product of the hydrodynamic velocity and the concentration of the j^{th} species in the electrolyte. In some cases, such as very strong supporting electrolytes and slow or stagnant flow, simplifications can be made, accounting only for Fickian diffusion in the electrolyte [Newman 1991, Chapter 16].

$$\bar{J}_j = -z_j u_j F C_j \bar{\nabla} \Phi + D_j \bar{\nabla} C_j + \bar{v} C_j$$

$$\bar{i} = -F^2 \bar{\nabla} \Phi \sum_{j=1}^n z_j^2 u_j C_j - F \sum_{j=1}^n z_j D_j \bar{\nabla} C_j$$

The reactive transport equation includes a term for the homogeneous reaction of the j^{th} species in the molten salt of fuel.

$$\frac{\partial C_j}{\partial t} = -\bar{\nabla} \cdot \bar{J}_j + R_j$$

These equations serve as a solid foundation for many useful approximations for the mass-transport limited current density encountered in electrochemical systems, including metals and alloys under corrosion.

Approximations Based Upon Mass-Transport Limited Currents

Simplifications exist that enable mass transport effects to be accounted for with relatively simple expressions which include limiting current expressions for cathodic and anodic reactions [Bard & Faulkner, Chapter 4].

$$\frac{i_j}{i_{0,j}} = \left(1 - \frac{i_j}{i_{l,c,j}}\right) e^{-\alpha_j z_j f \eta_j} - \left(1 - \frac{i_j}{i_{l,a,j}}\right) e^{(1-\alpha_j) z_j f \eta_j}$$

This expression can be rearranged, providing an explicit expression for the electrochemical overpotential for the j^{th} species in terms of the exchange current density, and the limiting current densities for the anodic and cathodic reactions.

$$\eta_j = -\frac{RT}{z_j F} i_j \left(\frac{1}{i_{0,j}} + \frac{1}{i_{l,c,j}} + \frac{1}{i_{l,a,j}} \right)$$

This expression can be further simplified, expressing the proportionality between the overpotential and total current density in terms of three resistances, the charge transfer resistance which represents the heterogeneous kinetics at the electrode-electrolyte interface, the mass transfer resistance associated with the anodic reaction, and the mass transfer resistance associated with the cathodic reaction.

$$\eta_j = i_j (R_{ct,j} + R_{mt,c,j} + R_{mt,a,j})$$

The limiting current densities can be calculated from appropriate correlations for flow channels, or rotating cylinder and disk electrodes, which are used to study such systems due to their well understood and characterized flow fields [Bard & Faulkner 1980, Chapter 8; Newman 1991, Chapter 17; Bennet & Myers 1974, Chapter 14]. These correlations are expressed in terms of three dimensionless numbers, the Schmidt, Reynolds and Nusselt numbers, Sc_j , Re and Nu_j , respectively.

$$Sc_j = \frac{\nu}{D_j}$$

$$Re = \frac{\omega d_R^2}{2\nu}$$

$$Nu_j = 0.0791 \times Re \times Sc_j$$

These numbers are written in terms of the kinematic viscosity, which is the ratio of the molten salt viscosity and density.

$$\nu = \frac{\mu}{\rho}$$

The Reynolds number and the corresponding limiting current for a rotating cylinder electrode are:

$$Re = \frac{\omega d_R^2}{2\nu}$$

$$i_{l,j} = \frac{F \times Nu_j \times D_j \times C_j}{d_R}$$

In the case of the rotating cylinder electrode, the Reynolds number and the corresponding limiting current are both linearly proportional to the angular velocity (ω). In contrast, in the case of the rotating disk electrode, the well-known Levich equation predicts that the limiting current density has a square root dependence on the angular velocity ($\omega^{1/2}$):

$$i_{l,j} = 0.620 F A \omega^{1/2} \nu^{-1/6} n_j D_j^{3/2} C_j$$

The pertinent feature of the rotating disk electrode, illustrated in Figure 9 is that the velocity normal to the disk, which brings fresh reactant to and product away from the surface depends upon axial displacement (z), but not on radial displacement (r).

$$v_z = \sqrt{\nu \omega} H \left(z \sqrt{\frac{\omega}{\nu}} \right)$$

Consequently, there is no reason for the concentration to depend upon anything besides the normal distance from the disk. The convective velocity bringing fresh reactant to the electrode is the same over the entire surface of the disk, with the practical advantage that the reaction rate at the electrode surface will be the same everywhere, independent of the distance from the axis of rotation. Levich analyzed the mass transfer to a rotating disk electrode, with rigorous incorporation of the fluid dynamics, with the results given here. Several examples of experimental determination of the limiting current are available in the literature [Farmer et al. 1992].

Threshold Potential for Localized Corrosion

The resistance to such localized corrosion should be quantified through measurement of the open-circuit corrosion potential (E_{corr}), the threshold potential for localized attack ($E_{threshold}$), and the repassivation potential (E_{rp}), provided that the localized attack involves destabilization of a passive film, and provided that repassivation occurs during the cathodic branch of the polarization curve. Spontaneous breakdown of the passive film and localized corrosion require that the open-circuit corrosion potential exceed the critical potential [Farmer et al. 1989-1991, 1998-2000]:

$$E_{corr} \geq E_{threshold}$$

The greater the difference between the open-circuit corrosion potential and the critical potential (ΔE), the more resistant a material is to modes of localized corrosion such as pitting and crevice corrosion. In integrated corrosion models, general corrosion is invoked when E_{corr} is less than $E_{threshold}$ ($E_{corr} < E_{threshold}$), and localized corrosion is invoked when E_{corr} exceeds $E_{threshold}$. Measured values of the repassivation potential (E_{rp}) are sometimes used as conservative estimates of the critical potential ($E_{threshold}$).

Cyclic polarization is a convenient way to determine the threshold potential for steels and refractory alloys in high-temperature molten salts such as FLIBE. To the extent possible, cyclic polarization (CP) measurements should be conducted in accordance with the ASTM G 5 standard, and related standards, with those modifications necessary for application in a high-temperature electrochemical cell with a molten salt electrolyte. Note that the ASTM G 5 standard calls for a 1N H₂SO₄ electrolyte, whereas measurements for the fusion-fission hybrid reactor will be made with FLINAK, FLINABE and/or FLIBE, with the possible addition of UF₄ as representative fuel, and other elements to serve as surrogate fission products. In the absence of high fluxes of fast neutrons, the effects of transmutation will be simulated by adding hydrogen fluoride to and inert purge gas that will be bubbled through the cell.

Since relatively little actual corrosion data appears to exist for ODS ferritic steels under conditions specifically relevant to operation of the LIFE Engine, experiments must be done to obtain the required data. First, the open-circuit potential (OCP), relative to a suitable high-temperature reference electrode, should be monitored as a function of immersion time. Note that the OCP correspond the corrosion potential (E_{corr}). The linear polarization method should then be used as a means of monitoring the corrosion rates of various structural steels and refractory alloys immersed in FLIBE and FLINABE. This approach will require that the relevant anodic and cathodic reactions must be established.

Application of Mixed Potential Theory to Engine Materials

When two metals are galvanically coupled, a intermediate "mixed potential" is established. The exact position of this mixed potential, which is located between the oxidation-reduction

potentials of the coupled metals, is determined by their relative electrode kinetics. The anodic and cathodic reactions are usually assumed to obey Tafel kinetics, and electro-neutrality must be preserved in the reactions. The intersection of the anodic and cathodic Tafel lines identifies the formal mixed potential. This will be the rest potential of both galvanically coupled metals. At this potential, one metal will undergo anodic dissolution, while the other will be cathodically protected, with the possible recombination of hydrogen ions on the surface. As an example, consider the zincs on your boats brass propeller, the less noble metal (zinc) will undergo anodic dissolution to protect the more noble metal from corrosion (brass or steel).

By galvanically coupling either metallic lithium or beryllium to iron immersed in a blanket of FLIBE, a mixed potential will be established for the couple between the two reduction-oxidation (redox) potentials. This mixed potential will be more positive than the reversible potential for either the lithium and beryllium couple and more negative than the reversible potential for either the iron and hydrogen couple. The lithium or beryllium will therefore undergo preferential dissolution, while the solid iron will be cathodically protected, and the hydrogen ions (from hydrofluoric acid species) will be converted to free fluoride anion and hydrogen gas. This may be an over simplified explanation, and the published standard potentials (which are directly related to the Gibbs free energies for the reactions) are for aqueous solutions (solutions with hydrogen ions). However, they do provide sufficient insight for a generalized understanding.

The coupling of a sacrificial material, such a lithium or beryllium, to a more noble material, such a ODS ferritic steel, serves to protect the steel at the expense of the sacrificial material. The extent of the protection provided by such galvanic coupling can be predicted through application of the mixed potential theory. To explain this concept, it is best to begin by defining the total externally-applied electrochemical current in terms of the anodic and cathodic contributions.

$$I_{total} = I_a + I_c$$

The anodic current is then calculated by summing all anodic reactions that occur in parallel:

$$I_a = \sum_{j=1}^m A_{a,j} i_{a,j}$$

The cathodic current is then calculated by summing all cathodic reactions that occur in parallel:

$$I_c = \sum_{j=1}^m A_{c,j} i_{c,j} \frac{C_j}{C_j^*}$$

At the open circuit corrosion potential, since there is no externally applied current, and since the conservation of charge must be obeyed, the anodic and cathodic currents are equivalent:

$$I_a = I_c$$

This can be rewritten in terms of the anodic and cathodic current densities for each of the reactive species in the system as follows:

$$\sum_{j=1}^m A_{a,j} i_{a,j} + \sum_{j=1}^m A_{c,j} i_{c,j} \frac{C_j}{C_j^*} = 0$$

The anodic and cathodic current densities depend upon the corresponding overpotentials:

$$i_{a,j} = i_{0,j} e^{-\alpha_j z_j f \eta_j}$$

$$i_{c,j} = -i_{0,j} e^{(1-\alpha_j) z_j f \eta_j}$$

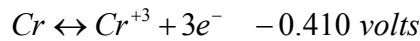
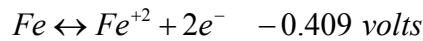
$$\sum_{j=1}^m A_{a,j} i_{0,j} e^{-\alpha_j z_j f \eta_j} - \sum_{j=1}^m A_{c,j} i_{0,j} e^{(1-\alpha_j) z_j f \eta_j} \frac{C_j}{C_j^*} = 0$$

$$A_a \sum_{j=1}^m i_{0,j} e^{-\alpha_j z_j f \eta_j} - A_c \sum_{j=1}^m i_{0,j} e^{(1-\alpha_j) z_j f \eta_j} \frac{C_j}{C_j^*} = 0$$

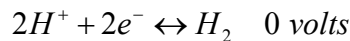
The difference between the mixed potential, which corresponds to the open-circuit corrosion potential, and the reversible potential for the j^{th} oxidation-reduction couple, can be substituted for the overpotential, and the above expression rewritten.

$$\sum_{j=1}^m i_{0,j} e^{-\alpha_j z_j f (E_{mix} - E_j^0)} - \frac{A_c}{A_a} \sum_{j=1}^m \frac{C_j}{C_j^*} i_{0,j} e^{(1-\alpha_j) z_j f (E_{mix} - E_j^0)} = 0$$

While the actual reactions involved in the corrosion of structural and cladding materials in the LIFE engine by molten salt coolants and fuels are numerous and complex, the following representative reactions can be used to shed light on the possible benefits of galvanically coupling beryllium and ODS ferritic steel. The anodic oxidation reactions for iron and chromium free electrons at the interface, and occur at nearly the same potential:

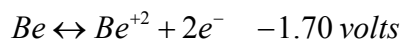


The transmutation of lithium in the molten salt will continuously generate a supply of tritium cations for the depolarization of the anodic corrosion reactions. Tritium cations are expected to behave electrochemically like hydrogen ions. The cathodic reduction of these dissolved cations will consume electrons produced during the anodic dissolution of the ODS steel.



In this case, the dissolution rate of the engine wall will be bound by the tritium breeding rate, minus the rate at which tritium is removed from the salt. This reaction will serve as an ideal depolarization reaction for the anodic dissolution of iron and chromium, and may also provide adsorbed hydrogen isotopes at the interface which can diffuse into the bulk, thereby causing hydrogen embrittlement and hydrogen-induced cracking. Such bulk hydrogen could also reduce Y_2O_3 and TiO_2 nanoparticles, thereby removing the nanostructural feature responsible for high-temperature strengthening, and immunity to excessive irradiation-induced swelling. If this is found to be problematic, TMT-type materials may provide an opportunity for superior performance.

Beryllium can be galvanically coupled to the ODS steel, thereby enabling it to serve as a protective sacrificial anode.



At the mixed potential that results from the coupling of the reactions for the anodic dissolution of iron and chromium, the reaction for the cathodic reduction of hydrogen isotope ions, and the reaction for the sacrificial anodic dissolution of beryllium, the anodic current densities and corrosion rates for iron and chromium will be suppressed, since these reactions will occur at a more cathodic potential than they would otherwise occur. The mixed potential can be substituted into the expressions for anodic current density, and the corresponding corrosion rate.

As shown in Figure 10, mixed potential theory applied to ODS ferritic steel without Be in molten Li_2BeF_4 . In this case, the anodic Tafel line is assumed to be due to the anodic dissolution of iron and chromium from the ODS, while the cathodic Tafel line is assumed to be due to the electrolytic reduction of tritium cations. The intersection of these two Tafel lines defines the open circuit corrosion current, and the dissolution current density (corrosion rate).

As shown in Figure 11, mixed potential theory applied to ODS ferritic steel with sacrificial Be in molten Li_2BeF_4 . In this case, the anodic Tafel line is assumed to be due to the anodic dissolution of sacrificial beryllium, as well as iron and chromium from the ODS, while the cathodic Tafel line is assumed to be due to the electrolytic reduction of tritium fluoride. The intersection of these two Tafel lines defines the open circuit corrosion current, and the dissolution current density (corrosion rate). Most of the anodic current density is attributed to dissolution of the sacrificial beryllium, which shifts the open circuit corrosion potential to more negative levels, where the dissolution rates of Fe and Cr are less.

As shown in Figure 12, mixed potential theory applied to ODS steel with and without beryllium in molten Li_2BeF_4 . A comparison of these two curves, taken from Figures 10 and 11 respectively, clearly show the cathodic shift of the open circuit corrosion potential due to galvanic coupling of beryllium and ODS steel.

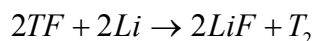
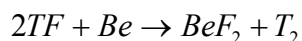
Cathodic Protection and Sacrificial Anodes

The corrosive attack of ODS FM steels in FLIBE may be manageable, provided that steps are taken to control the dissolution of the chromium into the fluoride salt. Corrosion resistance can be enhanced through careful engineering design, avoiding galvanic coupling of dissimilar metals, unless sacrificial protection is sought.

The use of sacrificial anodes is a form of passive electrochemical protection. Based upon preliminary analysis, it appears that either lithium (Li) or beryllium (Be) can be used as sacrificial anodes for the protection of the more noble ODS FM steel components. In the case of pure FLIBE, the introduction of metallic beryllium (Be) into FLIBE is considered a viable means of mitigating the corrosion of steels, since it promotes the conversion of hydrofluoric acid (HF or TF) species to hydrogen (H₂ or HT). If beryllium is used, the formation of colloidal beryllium in the molten salt may be problematic, in that it will thicken the solution. The formation of these particles may cause the salt solutions to become viscous, gray in appearance, and may necessitate continuous on-line removal. At this point, it should be noted that the beryllium neutron multiplier should be protected with a cladding or encapsulation to prevent unacceptable rates of dissolution and loss of dimensional tolerance during the service of the LIFE engine. Dimensional change would result in a loss of Be particle percolation in the annular regions of the LIFE engine, and jamming.

In essence, the beneficial effects observed by placing metallic beryllium in contact with neutron-irradiated FLIBE, with lithium transmutation products such as HF and TF can be understood, at least conceptually, by considering the electromotive series. Any electrochemical potential more negative (cathodic) than the stated Nernst potential will push the reactions to the right (reduction, acceptance of electron). Any electrochemical potential more positive (anodic) than the stated Nernst potential will push the reactions to the left (oxidation, liberation of electron by reduced metal or gas).

It is believed that metallic beryllium and lithium reduce hydrofluoric acid (HF/TF) formed from lithium transmutation products, and therefore eliminates aggressive free fluoride anions from the melt, along with the corrosive attack of structural materials caused by these species. The reactions for beryllium and lithium are:



Since more LiF than BeF₂ is consumed within the fusion reactor, the use of metallic lithium is the preferred method of reducing hydrofluoric acid and replenishing the lithium in the molten-salt blanket and coolant. The dissolution of either can be actively controlled with an adder potentiostat if desired.

Similar electrochemical protection may be accomplished with adder potentiostats (operational amplifiers with formal reference electrodes). Instead of relying on a sacrificial anode to maintain the surface to be protected at the appropriate potential, the potentiostat can be used to apply the potential through application of a carefully controlled current. Thus, the redox state of the ferritic steel and transmuted lithium (H^+ and T^+) can be intentionally converted to the gaseous forms in a well controlled manner.

The ODS FM steel structure may also undergo corrosive attack by liquid fuels, which would consist of Li_2BeF_4 and dissolved UF_4 , as well as a broad range of fission products. The ability of the broad range of fission products available at high burn-up to depolarize the anodic dissolution of the engine wall must be addressed. The use of sacrificial anodes and cathodic protection systems to mitigate the corrosion of the LIFE Engine in this aggressive environment should also be investigated.

An electrochemical controller could be used to mitigate the corrosive effects of HF and TF, and the attack of structural materials, such electrochemical control can also be used to manipulate the oxidation state of soluble uranium species (UF_3 , UF_4 and UF_6). The formation of the volatile hexavalent uranium species should be avoided if possible.

The use of high-temperature cathodic protection systems to control corrosion and actinide volatility in liquid fuels should be investigated. Imposed currents could suppress corrosion current and convert any potentially volatile hexavalent uranium species to the less volatile tetravalent form.

In summary, the free energy of formation of fluorides of the alloying elements found in steels and refractory alloys can be used to determine the relative stability of these materials in molten salts. The reduction of lithium transmutation products (H^+ and T^+) drives the electrochemical corrosion process, and liberates aggressive fluoride ions that pair with ions formed from dissolved structural materials. Corrosion can be suppressed through the use of metallic Be and Li, though the molten salt becomes laden with colloidal suspensions of Be and Li corrosion products in the process. Alternatively, imposed currents and other high-temperature cathodic protection systems are envisioned for protection of the structural materials. This general approach is highly successful in the protection of ship hulls. Electrochemical control could prove to be enabling technology for such high-temperature molten-salt reactors.

Corrosion Rate Limited by Corrosion Product Solubility

As discussed in the literature, corrosion of alloys in molten fluoride salts has been extensively studied for nuclear reactor applications [Lau 1990].

“The molten salt nuclear reactor uses a LiF - BeF_2 base salt as a fuel salt, with various amounts of UF_6 , ThF_4 , and ZrF_4 [Koger 1973]. The reactor coolant salt is $NaBF_4$ - NaF mixture. A nickel-based alloy, Hatelloy N, has proven to be the most corrosion resistant

in molten fluoride salts [Koger 1974]. The alloy was the primary containment material for a molten salt test reactor successfully operated from 1965 to 1969 [Keiser 1976]. Koger reported a corrosion rate of less than 0.0025 mm/y (0.1 mpy) at 704°C (1300°F) in the LiF-BeF₂ base salt (fuel salt) and about 0.015 mm/y (0.6 mpy) at 607°C (1125°F) in the NaBF₄-NaF coolant salt for alloy N [Koger 1973].”

“Iwamoto et al. [1980] performed corrosion tests in eutectic LiF-NaF-KF salt in a test loop with a 750°C (1380°F) hot leg and a 685°C (1265°F) cold leg for 500 hours. Alloy N exhibited only 2.06 mg/cm² of maximum weight loss at the hot leg.”

“At lower temperatures, austenitic stainless steels showed good performance. Type 316 exhibited 0.015 mm/y (0.59 mpy) at 650°C (1200°F) in 66LiF-34BeF₂ (mol. %), and about 0.002 mm/y (0.08 mpy) at 530°C (986°F) in 22LiF-31LiCl-47LiBr (mol. %) [Keiser 1979]. In a LiF-BeF₂ fuel salt containing UF₄, ThF₄ and ZrF₄, Type 304 suffered a corrosion rate of only about 0.028 mm/y (1.1 mpy) at 690°C (1270°F) [Koger 1973].”

“Corrosion can become more aggressive as temperature increases. It is particularly severe for stainless steels because of tube plugging problems due to mass transfer. Adamson et al. [1959] conducted corrosion tests in a thermal convection loop involving 43.5KF-10.9NaF-44.5LiF-1.1UF₄ (mol. %) with an 815°C (1500°F) hot leg and a 704°C (1300°F) cold leg. Types 410, 430, 316, 310, and 347 suffered severe tube plugging problems at the cold leg within the short test durations. Nickel and nickel-base alloys, on the other hand, showed no plugging even after 500 hours of testing. However, these alloys suffered corrosion at the hot leg after 500 hours of exposure. Alloy 600 suffered internal attack consisting of voids about 0.30 and 0.38 mm (12 to 15 mils) deep. NIMONIC alloy 75 suffered intergranular pitting about 0.20 to 0.33 mm (8 to 13 mils) deep, and nickel suffered even metal removal of about 0.23 mm (9 mils).”

“Misra and Whittenberger [1987] reported corrosion data for a variety of commercial alloys in molten LiF-19.5CaF₂, which was being considered for a heat-storage medium in an advanced solar space power system, at 797°C (1467°F) for 500 hours. The tests were conducted in alumina crucibles with argon as a cover gas. Results are tabulated in Table 4 (repeated in this report). For nickel-base alloys, chromium was detrimental. No influence of chromium, however, was noted in iron-base alloys.”

“Molten fluorides are generally used in a closed system under vacuum or an inert atmosphere. However, hydrogen fluoride may be present in the system, resulting in increased corrosion rates. Moisture, a common impurity in fluoride salts, can react with fluorides to produce gaseous HF, some of which may dissolve in the melt. Corrosion by HF will also be involved, leading to the production of hydrogen. Therefore, it is important to reduce the moisture level in the salt to reduce corrosion attack [Misra and Whittenberger, 1987].”

Based upon more recent data, corrosion rates of ODS ferritic steel by Li_2BeF_4 and Li-Na-K-F coolants are expected to be less than approximately 1 mil per year. Corrosive attack by these coolants will probably be limited by saturation of the electrolyte with dissolved iron and chromium. The beneficial effects of Be on the corrosion of ODS can be understood by application of mixed potential theory. Several refractory metals are also appropriate choices for corrosion protection in high-temperature fluoride salts. ODS has been successfully joined using several different industrial welding processes, and provides exceptional high-temperature properties LIFE engine design

The corrosion of austenitic iron and nickel based alloys such as Type 316 stainless steel and Inconel have been studied by Oak Ridge National Laboratory in a variety of high-temperature fluoride salts, with the results given in Table 5. Results for the alloy INOR-8 are also reported. Corrosion rates for the iron-based stainless steel appear to be bounded between approximately 5 and 150 mils per year [Williams et al. 2006].

As previously discussed, chromium from the ODS ferritic steel is expected to dissolve into both the FLIBE in the primary cooling loop, as well as into the FLINAK in the secondary cooling loop. The dissolution of alloy chromium will be limited to some extent by the saturation concentration of the chromium in the fluoride salt. These limiting solubility values are given in Table 6, and have been used to estimate the maximum wall penetration expected in the steel LIFE engine. The tabulated solubility for beryllium in fluoride salts further illustrates the facile dissolution of the neutron multiplier in these salts. Uranium is of course also readily dissolved, which is beneficial in the formation of damage tolerant liquid fuels [Williams et al. 2006].

A simple model has been developed to account for the dissolution of LIFE Engine materials in the high temperature FLIBE and FLINAK. This model assumes a constant rate of corrosion until the solution becomes saturated with chromium.

If the molten salt coolant or fuel saturates with iron and chromium corrosion products, the continued dissolution of the ODS ferritic steel will cease. To develop sufficient understanding of such saturation-limited corrosion, one begins with the conservation of mass, and the differential mass balance:

$$A_{ods} \times \rho_{ods} \times W_{ods,j} \times \frac{dx_{ods}}{dt} = V_{salt} \times \frac{dC_{salt,j}}{dt}$$

The penetration rate of the ODS steel due to molten salt corrosion (X_{ods}) can then be expressed in terms of the mass flux of iron and chromium into the liquid phase, from the corroding solid wall:

$$J_{ods,j} = \rho_{ods} \times W_{ods,j} \times \frac{dx_{ods}}{dt}$$

The flux is then substituted into the differential mass balance equation:

$$A_{ods} \times J_{ods,j} = V_{salt} \times \frac{dC_{salt,j}}{dt}$$

By invoking Fick's first law, the flux can be defined in terms of the diffusivity and concentration gradient of the dissolving iron or chromium (j^{th} species) in the molten salt:

$$J_{ods,j} = -D_{salt,j} \frac{dC_{salt,j}}{dx}$$

The concentration gradient can then approximated as the difference in the corrosion-product concentration in the salt at the engine wall, and the average concentration outside the mass-transfer boundary layer, divided by the thickness of the boundary layer. The corrosion-product concentration at the engine wall is assumed to be at saturation, the solubility limit of iron or chromium in the molten salt.

$$\frac{dC_{salt,j}}{dx} \approx \frac{C_{salt,j}^* - C_{salt,j}}{\delta_{salt,j}}$$

$$J_{ods,j} \approx -D_{salt,j} \left(\frac{C_{salt,j}^* - C_{salt,j}}{\delta_{salt,j}} \right)$$

This approximate solution is then substituted into the differential mass balance:

$$-A_{ods} \times \frac{D_{salt,j}}{\delta_{salt,j}} (C_{salt,j}^* - C_{salt,j}) \approx V_{salt} \times \frac{dC_{salt,j}}{dt}$$

Integration of the differential mass balance then provides a time-dependent relationship between the concentrations of the corrosion-products in the molten salt:

$$-\frac{A_{ods}}{V_{salt}} \times \frac{D_{salt,j}}{\delta_{salt,j}} \int_0^t dt \approx \int_0^{C_{salt,j}} \frac{dC_{salt,j}}{C_{salt,j}^* - C_{salt,j}}$$

The time-dependent relationship can be expressed as:

$$-\frac{A_{ods} D_{salt,j}}{V_{salt} \delta_{salt,j}} t \approx \ln \left(\frac{C_{salt,j}^* - C_{salt,j}}{C_{salt,j}^*} \right)$$

The differential mass balance is used again, this time to define the ratio of the diffusivity to the boundary layer thickness in terms of the steel density, the concentration of the metal in the ODS

steel forming the dissolved corrosion product, the corrosion rate at the initial time, and the solubility of the dissolving metal in the salt (dissolved corrosion product):

$$\frac{D_{salt,j}}{\delta_{salt,j}} = \frac{\rho_{ods} X_{ods,j}}{C_{salt,j}^*} \left(\frac{dx_{ods}}{dt} \right)_{t=0}$$

Redefining the corrosion rate at the initial time, the expression becomes:

$$\frac{D_{salt,j}}{\delta_{salt,j}} = \frac{\rho_{ods} X_{ods,j} r_{corr,j}^0}{C_{salt,j}^*}$$

Substitution provides a simple equation for the time-dependent concentration of corrosion products in the molten salt:

$$\frac{C_{salt,j}^* - C_{salt,j}}{C_{salt,j}^*} = e^{-(A_{ods}/V_{salt}) r_{corr,j}^0 t}$$

$$C_{salt,j} = C_{salt,j}^* \left(1 - e^{-(A_{ods}/V_{salt}) r_{corr,j}^0 t} \right)$$

The penetration of the engine wall can then be easily calculated from a simple mass balance:

$$\delta_{ods} = \frac{V_{salt} C_{salt,j}}{A_{ods} \rho_{ods} X_{ods}}$$

As will be discussed in a subsequent chapter, scanning electron microscopy (SEM) and energy dispersive analysis of X-rays (EDAX) of cross-sections of ODS steel frozen in FLIBE or FLINAK can be used to determine $C_{salt,j}$ and δ_{ods} , thereby calibrating and validating the model. For the time being, until better data is available, the parameters used to exercise this solubility-limited corrosion model for the LIFE engine are summarized as follows:

$$\rho_{ods} \approx 7.7808 \text{ g/cm}^3$$

$$\rho_{salt} \approx 2.0000 \text{ g/cm}^3$$

$$A_{ods} \approx 6,839,408 \text{ cm}^2$$

$$V_{salt} \approx 1,248,053 \text{ cm}^3$$

$$C_{salt,j}^* \approx 3,000 \text{ ppm} \times \rho_{salt}$$

$$C_{salt,j}^* \approx 0.006 \text{ g/cm}^3$$

$$r_{corr,j}^0 \approx 5 \text{ to } 71.1 \text{ mil/yr}$$

As previously discussed, the solubility of chromium in various molten fluoride salts is summarized in Table 6. Limited corrosive attack of the ODS FM steels by the high-temperature molten fluoride salts has been predicted for two cases. Case 1 assumes a constant rate of attack of 5.0 mils per year, and cessation of corrosion at the point when the salt becomes saturated with dissolved chromium at a concentration of 3000 ppm as shown in Figure 13. Case 2 assumes a constant rate of attack of 70.1 mils per year, and cessation of corrosion at the point where the salt becomes saturated with dissolved chromium at a concentration of 3000 ppm as shown in Figure 14.

As a final note, it is pointed out that the flux in the differential mass-balance equation can be defined in terms of the anodic current density if a potential-dependent prediction is desired.

$$J_{ods,j} = \frac{i_{a,j}}{z_j F}$$

Mechanical Fracture and Fatigue

Before presenting the mathematical framework for environmental fracture modes, such as stress corrosion cracking, the theoretical basis for mechanical fracture will be reviewed. The Griffith criteria for crack propagation relates energy release rate to stress, flaw size and elastic modulus [Thornton & Colangelo 1985, Chapter 9]:

$$G_C = \frac{\pi \sigma^2 a}{E}$$

This relationship provides the basis for the equation that enables prediction of the critical stress for mechanical fracture to the surface free energy, modulus and flaw size:

$$\sigma_C = \sqrt{\frac{2E\gamma_s}{\pi a}}$$

The threshold stress intensity factor for crack propagation can then be expressed in terms of the critical stress and the critical flaw size:

$$K_C = \sigma_C \sqrt{\pi a_C} f(a/W)$$

The LIFE engine will experience applied or residual tensile stress which will concentrate at imperfections on the surface of the engine. The stress intensity factor K_I for the concentration of tensile stress at a surface imperfection is given by Andresen and Ford [1994] and by Farmer et al. [1991, 2000].

$$K_I(a, \sigma) = \beta \sigma \sqrt{\pi a}$$

The geometric factor β is defined by the following polynomial:

$$\beta = 1.12 - 0.231\left(\frac{a}{h}\right) + 10.55\left(\frac{a}{h}\right)^2 - 21.72\left(\frac{a}{h}\right)^3 + 30.95\left(\frac{a}{h}\right)^4$$

An alternative solution for the stress intensity factor is:

$$K_I = G(K_I)_{SECP}$$

$$(K_I)_{SECP} = \sqrt{\pi a} \left[A_0 F_1 + \left(\frac{2a}{\pi}\right) A_1 F_2 + \left(\frac{a^2}{2}\right) A_2 F_3 + \left(\frac{4a^3}{3\pi}\right) A_3 F_4 \right]$$

Fatigue cracks may initiate and propagate when periodic fluctuations in stress are applied to a material. The propagation of fatigue cracks due to the application of cyclic stress is proportional to the fluctuation in the stress intensity factor:

$$\frac{da}{dN} = C(K_{\max} - K_{\min})^m$$

Environmental Fracture

Stress corrosion cracking (SCC) is assumed to initiate and propagate when the stress intensity factor exceeds the threshold stress intensity factor for SCC [Ford 1983; Jones 1987; Andresen 1987-88; Andresen & Ford 1994; Farmer et al. 1991, 2000]:

$$K_I \geq K_{ISCC}$$

Nakayama and Takano [1986] applied a slip-dissolution-repassivation (SDR) model to the SCC of Type 304 stainless steel in boiling 42% MgCl_2 solutions. The expression developed for crack propagation rate by these authors is:

$$V_t = \frac{da}{dt} = \frac{M \langle i \rangle}{zF\rho}$$

The time-average of the dissolution current density is $\langle i \rangle$, the molecular weight of the passive oxide film is M , the number of electrons transferred per mole of passive film formed is z , Faradays constant is F and the density of the passive oxide film is ρ .

$$\langle i \rangle = \frac{J^0}{\beta n_s (1 - \exp(-\beta/n_s))}$$

The dissolution current density for the fresh surface at the crack tip, free of the passive oxide is J^0 ; the decay constant for the transient repassivation current at the crack tip is β ; and n_s is the formation rate of slip steps. Similar models have been developed by Andresen and Ford for stress corrosion cracking, and also assume that propagation is due to the fracture of the passive film at the crack tip [1983-87].

$$V_t = \frac{da}{dt} = \frac{MQ_f}{zF\rho} \frac{d\varepsilon_{ct}}{dt} \frac{1}{\varepsilon_f}$$

The oxidation charge density between film-rupture events is represented by Q_f . As these authors point out, the effects of water and material chemistry on the crack propagation rate can be represented by a single parameter n :

$$V_t = \frac{da}{dt} = f(n) \left(\frac{d\varepsilon_{ct}}{dt} \right)^n$$

The slip-dissolution model for stress corrosion cracking has been used to predict crack propagation in boiling-water reactors [Andresen and Ford 1994], and is represented by the following equation:

$$V_t = \frac{da}{dt} = A \left(\frac{d\varepsilon_{ct}}{dt} \right)^n$$

Once initiated, stress corrosion cracks have been shown to propagate at a rate proportional to the crack tip strain rate raised to the n^{th} power. The straining at the crack tip causes slip and fracture of a brittle passive oxide film assumed to exist at the root of the crack. The proportionality factor is also expressed in terms of the adjustable parameter n , which depends upon the repassivation kinetics at the root of the crack:

$$A = 7.8 \times 10^{-3} (n)^{3.6}$$

Thus, the SCC propagation rate can be expressed in terms of the crack-tip strain rate and a single adjustable parameter n :

$$V_t = \frac{da}{dt} = 7.8 \times 10^{-3} (n)^{3.6} \left(\frac{d\varepsilon_{ct}}{dt} \right)^n$$

The crack-tip strain rate can then be calculated from the stress intensity factor:

$$\frac{d\varepsilon_{ct}}{dt} = 4.1 \times 10^{-14} K_I^4$$

Substitution of this expression for the crack-tip strain rate into the equation for the crack propagation velocity yields an expression directly relating velocity and stress intensity factor:

$$V_t = \frac{da}{dt} = \bar{A} (K_I)^{\bar{n}}$$

$$\bar{A} = A(4.1 \times 10^{-14})^n$$

$$\bar{n} = 4n$$

Other more fundamental models have been under development for more than two decades, but are not yet sufficiently mature to enable quantitative prediction of engine components. For example, a molecular dynamics (MD) model for the propagation of cracks in a surface covered with a thin brittle film was developed several years ago by Paskin et al. [1980-83]. Atoms were assumed to be arranged in a triangular lattice and to interact with a 6-12 Leonard Jones potential:

$$\Phi_{i,j} = \varepsilon \left[\left(\frac{d}{r_{i,j}} \right)^{12} - 2 \left(\frac{d}{r_{i,j}} \right)^6 \right]$$

Energies were measured in the units of well-depth (ε) and distances in units of the equilibrium spacing (d). A central difference method was used to solve Newton's laws of motion, thereby predicting molecular motion in the material near the incipient crack. The atomic positions, velocities, forces, total energy, work, potential energy, and modulus-of-elasticity were monitored throughout the simulation. An external tensile load was applied to each atom of the uppermost row, and each atom of the lowermost row of the sample. While such simulations provide invaluable insight into the mechanisms of SCC and other environmental cracking, quantitative predictions in realistic environments may not yet be possible for the LIFE engine, and more empirical models may still be required. More recently, others have done additional work on simulating environmental cracking of alloys, including SCC, with MD techniques.

Chapter C. Gaps in Knowledge & System Vulnerabilities

There are a number of outstanding challenges for the first wall, the neutron multiplication blanket, the structural materials, and the high-temperature molten-salt coolants. Practical realization of the spherical ODS chamber required for construction of the LIFE engine also requires substantial work. For example, methods for the large-scale production of high quality ODS steel must be developed. Methods for making joints (welds) with high integrity are also required. Critical properties must be determined, and include: long-term creep rates and rupture times, fatigue, creep-fatigue and fatigue crack growth, compatibility and corrosion rates in molten salts, and environmental cracking. The effects of long-term exposure to high-flux fast

neutrons at high temperature, the exact role of oxide nanoparticles in strengthening ODS steels, and the evolution of these small oxide particles during operation must all be better understood.

While predictive models for the corrosion of structural and cladding materials by high-temperature molten salts exist, or can be developed, there is insufficient test data to fully calibrate model parameters, and validate model predictions. Data from corrosion tests, accounting for the effects of irradiation and stress are desperately needed. Liquid metal corrosion has not been dealt with, but should be considered in the future [Pint et al. 2004 & 2006].

Chapter D. Strategy for Future Work

Over the next twelve months, the LIFE Materials Team will deliver more detailed predictive models for the corrosion of structural and cladding materials, as well as a detailed plan for experiments necessary to calibrate and validate model parameters, and preliminary results from the initial corrosion performance experiments, assuming that adequate resources are available for the planned work scope. Specific interrelated issues that must be dealt with include: pulsed heating of the first wall, structure and any required cladding, and the associated mechanical stresses; high-temperature creep of structural materials; corrosion and environmental cracking of those reactor components exposed to the high-temperature molten-salt coolant and tritium breeding blanket; radiation damage on fuels, structural and first wall materials; the creation of appropriate test environments for materials within the laboratory, including extreme neutron fluxes with representative energy spectra, rapid thermal pulsing with homogeneous heating; exposures to high-temperature lithium-beryllium-fluoride molten salts, and special problems associated with the use of beryllium multipliers in such applications. Planning, modeling and early experimental work will be used to begin solving corrosion and environmental cracking problems currently believed to challenge the LIFE reactor concept. A detailed research and development strategy will be formulated, thereby enabling the team to attack crucial corrosion and environmental cracking problems in an efficient and comprehensive manner.

Objectives

The LIFE Engine requires materials that can withstand harsh conditions of radiation, high temperature, active chemical agents, and thermal and sympathetic mechanical stress pulses for periods of time as long as 60 years. Pulse rates of 10 to 20 hertz are envisioned. While we have identified materials and materials systems candidates for first wall and fuel, practical experience and modeling code validation regarding these materials under the extreme conditions of LIFE does not yet exist. Even if an appropriate neutron material testing facility were to exist, testing materials over the intervals of 60 years is not considered to be a viable option at the present time. Accelerated testing methods coupled to advanced theory and modeling appears to be the only way to rapidly evaluate candidate materials. Thus, development of capabilities for reliable accelerated material testing becomes a critical priority for the development of LIFE.

Integral with this experimental simulation will be the implementation of existing models and the development of advanced codes to interpret experimental data. More importantly, the successful implementation of the modeling codes will also serve as a confidence builder for prediction of material performance under LIFE conditions.

The degradation and failure of LIFE Engine components will be limited by high-temperature corrosion in Li_2BeF_4 , LiNaBeF_4 and other coolants. A testing program will be needed to understand the corrosion, environmental fracture, thermally-driven fatigue, and radiation damage of hybrid reactor materials in high-temperature molten salts with high neutron fluence. Corrosion and environmental cracking will be exacerbated by thermal aging and radiation damage of crystalline solids, and the formation of transmutation products such as tritium fluoride and related chemical species (TF, DF & HF). Galvanic coupling of dissimilar materials, with one serving as a catalytic cathode, will drive anodic dissolution of the other at an accelerated rate. Enhanced mass transport in the intense flow-field of the vortex and annuli will accelerate corrosive dissolution of materials.

Fluoride salts formed with Mo, W, Ni and V are less stable than TF (HF) which will be formed by transmutation of lithium. Therefore, these metals are believed to have good corrosion resistance in FLIBE. In contrast, the other metals would be expected to undergo reaction with the fluoride ion to form stable fluoride-salt corrosion products.

Materials have been selected for construction of a LIFE Engine, and the susceptibility of those materials to corrosion must be determined. When problems are identified, alternative materials designs and selections may be required.

Ultimately, the effects of irradiation on materials subjected to corrosion and environmental cracking must be accounted for. As part of the point design effort we will develop detailed plans for a multi-ion-beam accelerated materials radiation facility while carrying out early experimental simulations of reactor environment radiations by sequential materials irradiations with helium and heavy ions to simulate the materials property changes associated with the LIFE environment. The ODS steel will be studied to radiation damage levels in excess of 200 dpa. Temperatures for irradiations will be representative of the anticipated operating conditions.

Tasks

1. Develop credible models for predicting the corrosion performance of materials
2. Procure or synthesize materials for testing
3. Develop a detailed plan for the modeling and experimental work to address these concerns
4. Procurement and preparation of coolants
5. Procurement and preparation of materials
6. Ion beam irradiation of materials for corrosion and environmental tests
7. Perform corrosion and environmental cracking tests

Deliverables

1. Necessary database to support development of models
2. Credible conceptual mechanistic corrosion and environmental cracking models
3. Quantitative predictive corrosion and environmental cracking models
4. Library of calibrated model parameters
5. Quantitative assessment of materials performance in molten salts
6. High quality material samples for testing
7. Ion beam irradiated materials samples for corrosion and environmental cracking tests
8. Data from high-temperature molten-salt testing for model calibration and validation
9. Long-range test plan for irradiations in LIFE Demonstration Unit

Experimental Methodology

Electrochemical Measurement of Corrosion Rates

The procedure proposed for in situ determination of corrosion rates is linear polarization. This test method consists of the following steps: (1) holding the sample for ten seconds at the OCP; (2) beginning at a potential 20 mV below the OCP, increasing the potential linearly at a constant rate of 0.1667 mV per second to a potential 20 mV above the OCP; (3) recording the current being passed from the counter electrode to the working electrode as a function of potential relative to an appropriate high-temperature reference electrode; and (4) determining the parameters in the cathodic Tafel line by performing linear regression on the voltage-current data, from 10 mV below the OCP, to 10 mV above the OCP. The slope of this line is the polarization resistance (R_p), and is defined in the published literature [Treseder 1991].

$$R_p = \left(\frac{\partial E}{\partial I} \right)_{E_{corr}}$$

A parameter (B) was defined in terms of the anodic and cathodic slopes of the Tafel lines:

$$B = \frac{\beta_a \beta_c}{2.303(\beta_a + \beta_c)}$$

The corrosion current density (i_{corr}) was defined in terms of the Tafel parameter (B), the polarization resistance (R_p) and the actual electrode area (A):

$$i_{corr} = \frac{B}{R_p \times A}$$

The corrosion or penetration rates of the amorphous alloy and reference materials are calculated from the corrosion current densities with the following formula:

$$\frac{dp}{dt} = \frac{i_{corr}}{\rho_{alloy} n_{alloy} F}$$

In this corrosion rate equation, p is the penetration depth, t is time, i_{corr} is the corrosion current density, ρ_{alloy} is the density of the alloy, n_{alloy} is the number of gram equivalents per gram of alloy, and F is Faraday's constant. The value of n_{alloy} is calculated with the following formula:

$$n_{alloy} = \sum_j \left(\frac{f_j n_j}{a_j} \right)$$

In this equation f_j is the mass fraction of the j^{th} alloying element in the material, n_j is the number of electrons involved in the j^{th} anodic dissolution process, which is assumed to be congruent, and a_j is the atomic weight of the j^{th} alloying element. Congruent dissolution is assumed, which meant that the dissolution rate of a given alloy element was proportional to its concentration in the bulk alloy. These equations are used to calculate factors for the conversion of corrosion current density to the penetration or corrosion rate.

Determining the Effects of Mass Transfer on Corrosion Rate

The effects of mass transfer on the corrosion current density, and the corresponding rate of corrosion, can be studied with either rotating disk or rotating cylinder electrodes fabricated from the material to be evaluated. Such an approach enables the effects of flow to be accounted for in a rigorous manner, without the construction of large and expensive flow loops.

In the case of the rotating cylinder electrode, the Reynolds number and the corresponding limiting current are both linearly proportional to the angular velocity (ω). In contrast, in the case of the rotating disk electrode, the well-known Levich equation predicts that the limiting current density has a square root dependence on the angular velocity ($\omega^{1/2}$):

$$i_{l,j} = 0.620 F A \omega^{1/2} \nu^{-1/6} n_j D_j^{3/2} C_j$$

Simplifications have been developed that enable the effects of mass-transfer limitations to be taken into account with terms representing limiting currents for cathodic and anodic reactions.

$$\frac{i_j}{i_{0,j}} = \left(1 - \frac{i_j}{i_{l,c,j}} \right) e^{-\alpha_j z_j f \eta_j} - \left(1 - \frac{i_j}{i_{l,a,j}} \right) e^{(1-\alpha_j) z_j f \eta_j}$$

Determining Solubility Limited Corrosion Rate from Dissolved Metal

The predicted penetration depth due to corrosion can be determined with scanning electron microscopy (SEM), and can also be calculated directly from the concentration of dissolved metal in the frozen salt:

$$\delta_{ods} = \frac{V_{salt} C_{salt,j}}{A_{ods} \rho_{ods} X_{ods}}$$

The predicted concentration in the salt is:

$$C_{salt,j} = C_{salt,j}^* \left(1 - e^{-\left(A_{ods} / V_{salt} \right) r_{corr,j}^0 t} \right)$$

Elemental mapping with energy dispersive analysis with X-rays (EDAX) will enable direct determination of the concentration profiles necessary for the solubility-limited corrosion model. A cross-sectional view of multiple samples exposed to high-temperature molten salt is shown in Figure 15. Samples will be frozen in the fluoride salt during rapid cooling, and will be subsequently cross-sectioned to enable SEM and elemental mapping of the corroded interface with EDAX are shown in Figure 16.

The left image in Figure 17 shows a crystallographic map showing micron-size grains in the high chromium ODS steel that was tested in FLINAK at 750°C. The layer closest to the surface is believed to have experienced grain growth due to heating and machining. The electron microscopy in the center shows the formation of voids due to the preferential dissolution of chromium rich phases in the near surface region of the material. This mode of attack penetrated to a depth of approximately 100 microns. The image on the right shows the infiltration of molten fluoride salt into the surface voids formed by preferential chromium dissolution revealed in three dimensional.

Electrochemical Impedance Spectroscopy of Interface

The working electrode is subjected to a small amplitude (± 5 mV) potential modulation centered at the open circuit corrosion potential, and the resultant current response measured. The modulation voltage (e) and the current response (i) are separated by a phase angle (ϕ) [Bard & Faulkner 1980, Chapter 9].

$$e = E \sin(\omega t)$$

$$i = I \sin(\omega t + \phi)$$

For pure resistance, the phase angle (ϕ) is zero. For pure capacitance, a phase difference exists between the voltage modulation and the current response:

$$i = \frac{E}{X_C} \cos(\omega t) = \frac{E}{X_C} \sin\left(\omega t + \frac{\pi}{2}\right)$$

The phase angle (ϕ) is $\pi/2$ for this case, pure capacitance. The voltage and current can be expressed in phasor notation. For pure resistance, the relationship between voltage, current and resistance is:

$$E_R = I R$$

This reflects Ohm's Law. For pure capacitance, the relationship between voltage, current and resistance is:

$$E_C = -j X_C I$$

The capacitive resistance is defined as:

$$X_C = \frac{1}{\omega C}$$

For the case of an equivalent circuit with a resistor and capacitor in series

$$E = E_R + E_C$$

The voltage can also be expressed in complex notation as:

$$E = I(R - j X_C)$$

The complex impedance (Z) is then defined and used to express the relationship that exists between the voltage and current in a system with both resistive and capacitive components:

$$E = I Z$$

The complex impedance has real and imaginary parts:

$$Z = |Z_{\text{Re}}| - j|Z_{\text{Im}}|$$

The complex impedance (Z) and the complex admittance (Y), which is the inverse of the impedance, can also be written as:

$$Z = |Z| e^{j\phi}$$

$$Y = \frac{1}{|Z|} e^{-j\phi}$$

The real and imaginary parts of the complex impedance are defined from the pure resistance and pure capacitance, respectively:

$$Z = R - jX_C$$

The magnitude of the complex impedance is:

$$|Z| = (R^2 + X_C^2)^{1/2}$$

The tangent of the phase angle ($\tan \phi$) is defined as the ratio of the capacitive resistance (X_C) to the pure resistance (R):

$$\tan \phi = \frac{X_C}{R} = \frac{1}{\omega R C}$$

The most common equivalent circuit for an electrochemical cell includes a solution resistance (R_Ω) in series with a Faradaic impedance (R_{ct}) and double layer capacitance (C_d) pair in parallel.

$$Z_{\text{Re}} = R_\Omega + \frac{R_{ct} + \sigma \omega^{-1/2}}{(C_d \sigma \omega^{1/2} + 1)^2 + \omega^2 C_d^2 (R_{ct} + \sigma \omega^{1/2})^2}$$

$$Z_{\text{Im}} = \frac{\omega C_d (R_{ct} + \sigma \omega^{-1/2})^2 + \sigma \omega^{-1/2} (\omega^{1/2} C_d \sigma + 1)}{(C_d \sigma \omega^{1/2} + 1) + \omega^2 C_d^2 (R_{ct} + \sigma \omega^{1/2})^2}$$

The Warburg impedance is defined in terms of (σ), which reflects the relative magnitude of kinetic and mass transfer rates:

$$\sigma = \frac{1}{nFA\sqrt{2}} \left(\frac{\beta_O}{D_O^{1/2}} - \frac{\beta_R}{D_R^{1/2}} \right)$$

Tafel kinetics are represented by (β_O) and (β_R).

$$\beta_O = \frac{RT}{zFC_O^*}$$

$$\beta_R = \frac{RT}{zFC_R^*}$$

The Warburg resistance (R_W) and Warburg capacitance (C_W) are defined as:

$$R_W = \frac{\sigma}{\omega^{1/2}}$$

$$C_W = \frac{1}{\sigma \omega^{1/2}}$$

The low-frequency limit ($\omega \rightarrow 0$) captures the effects of mass transport, and the Warburg impedance:

$$Z_{\text{Re}} = R_{\Omega} + R_{ct} + \sigma \omega^{-1/2}$$

$$Z_{\text{Re}} = R_{\Omega} + R_{ct} + R_W$$

$$Z_{\text{Im}} = \sigma \omega^{-1/2} + 2\sigma^2 C_d$$

$$Z_{\text{Im}} = \sigma^2 (C_W + 2C_d)$$

$$Z_{\text{Im}} = Z_{\text{Re}} - R_{\Omega} - R_{ct} + 2\sigma^2 C_d$$

The high-frequency limit has no mass-transfer dependence, and is:

$$Z = R_{\Omega} - j \left(\frac{R_{ct}}{R_{ct} C_d \omega - j} \right)$$

$$Z_{\text{Re}} = R_{\Omega} + \frac{R_{ct}}{1 + \omega^2 C_d^2 R_{ct}^2}$$

$$Z_{\text{Im}} = \frac{\omega C_d R_{ct}^2}{1 + \omega^2 C_d^2 R_{ct}^2}$$

$$\left(R_{\text{Re}} - R_{\Omega} - \frac{R_{ct}}{2} \right)^2 + Z_{\text{Im}}^2 = \left(\frac{R_{ct}}{2} \right)^2$$

This equation gives the classic semicircular plot of Z_{Im} versus Z_{Re} which is known as the Nyquist plot. The parameters in the equivalent circuit model can be determined graphically from such a plot, assuming ideal behavior. Alternatively, the impedance data can be plotted in the frequency domain as a Bode plot, which shows a peak in phase angle at the resonant frequency.

A three-electrode electrochemical cell with an ODS steel working electrode undergoing high-temperature molten-salt corrosion can be investigated with linear polarization and electrochemical impedance spectroscopy (EIS). An electrochemical cell developed by LLNL for electrochemical corrosion testing of structural and cladding materials in high-temperature molten fluoride salts is shown in Figure 18. The material being tested is held in the electrochemical by a machined ceramic plug. The lower right image shows the cell at 800°C. Figure 19 is a collection of three photographs showing the working electrode on the left, which is a relatively large disk of ODS steel, a reference electrode on the right, which is a relatively small disk of ODS steel, and counter electrode, which is a platinum bar suspended above the two ODS steel disks. The electrical resistance of high-temperature electrochemical cell for testing structural and cladding materials in high-temperature molten-salt environments is shown in Figure 20, with the melting of the salt and sample wetting as the cell evident as the cell was heated to 800°C. The ability to perform in situ electrochemical impedance spectroscopy (EIS) of steel surface in molten-salt at

800°C has been demonstrated, as shown in Figure 21. A simple single time-constant equivalent circuit is insufficient to explain EIS spectra.

Unfortunately, the behavior of a real system may not conform to a simple single-time constant equivalent circuit model. Other effects due to evolving interfacial structure of the corroding sample, including the passive oxide film and the chromium depletion layer, must be captured with additional interfacial impedances to fully explain experimental observations. A two time constant model is required to explain observed impedance spectra qualitatively, with more parameters needed for better fit, as shown in Figure 22.

Additional time constants can be captured by sequentially combining parallel and series impedances until enough complexity has been included to account for observations. As an example, two parallel complex impedances are combined initially:

$$Z_{parallel} = \frac{Z_1 Z_2}{Z_1 + Z_2}$$

The resultant parallel impedance is then combined in series with a third impedance to yield the series capacitance:

$$Z_{series} = Z_{parallel} + Z_3$$

$$Z_{series} = \frac{Z_1 Z_2}{Z_1 + Z_2} + Z_3$$

The effects of various complexities can also be accounted for with such parallel and series impedances based upon mechanistic understanding. As an example, consider the interpretation of a two-time constant impedance spectrum in terms of the electrosorption kinetics of divalent copper on gold substrates [Farmer 1985].

Thermal Pulsing & Corrosion Fatigue

A current pulse can be used to rapidly and homogeneously heat samples of structural and cladding materials, thereby simulating the thermal pulsing anticipated in the LIFE engine. To simulate the a predicted temperature pulse ($\Delta T/\Delta t$), a current pulse of amplitude (I) with pulse width (Δt) must be applied to the sample, which is assumed to have a resistance (R), mass density (m), and volume (V). A test sample of structural material being thermally stressed with a series of current pulses is shown in Figure 23. The corresponding a timing chart showing the sympathetic temperature transients is shown in Figure 24. Temperature depends upon current as follows:

$$\frac{\Delta T}{\Delta t} \approx \frac{dT}{dt} = \frac{I^2 R}{m V C_p}$$

$$I = \sqrt{\frac{\Delta T}{\Delta t} \frac{m V C_p}{R}}$$

For large-amplitude temperature pulses, the effects of temperature on the electrical resistance must be accounted for:

$$\rho = \rho_0 (1 + \alpha_p \Delta T)$$

$$R = \frac{\rho_0 (1 + \alpha_p \Delta T) L}{A}$$

The temperature pulse can then be translated into transient strain and stress with the coefficient of thermal expansion (α):

$$\sigma = \alpha E \Delta T = \alpha E \left(\frac{I^2 R}{m V C_p} \right) \Delta t$$

At a surface flaw of size (a), the stress from thermal pulsing can be used to calculate the stress intensity factor:

$$K_I(a, \sigma) = \beta \sigma \sqrt{\pi a}$$

Fatigue cracking occurs when periodic fluctuations in stress are applied to a material. The propagation of fatigue cracks due to the application of cyclic stress is proportional to the fluctuation in the stress intensity factor:

$$\frac{da}{dN} = C (K_{\max} - K_{\min})^m$$

Fatigue cracks can then be initiated at surface flaws in the sample as shown in Figure 25.

Measurements of Small Ion-Beam Irradiated Samples

Initially, the effects of irradiation will have to be determined with relatively small samples of material that can be bombarded with ions in an accelerator [Allen et al. 2005]. Test methods will have to be developed that enable properties and performance to be determined from such small ion-beam irradiated samples. In regard to the determination of mechanical properties of small ion-beam irradiated samples, the ultimate tensile strength (UTS) for a material can be determined from measurements of the Brinell hardness number (BHN) as shown in the following equation, and as illustrated in Figure 26.

$$UTS \approx 300 \times BHN = 300 \times \left[\frac{2P}{\pi D (D - \sqrt{D^2 - d^2})} \right]$$

Electrochemical testing, which has already been described in detail, provides an ideal means for determining the corrosion rates of such irradiated samples. Bent specimens can be irradiated, and then subjected to corrosive environments.

Integrated Predictive Models

This section of the Topical Report (TR) on Corrosion and Environmental Cracking describes work that will be done to address the materials challenges that have been identified and discussed. A systematic approach to materials modeling includes corrosion and environmental cracking, and will enable design of next-generation materials, as illustrated in Figure 27. Accelerated testing of materials will be required, including in situ corrosion and environmental cracking, accounting for the effects of irradiation database and mechanical stress.

Summary

The LIFE Engine is an advanced high-performance nuclear energy conversion device with an ICF spark plug and requires integration of some of the world's most advanced reactor materials. The initial engine concept includes a W 1st wall, ODS steel structure, Be neutron multiplier blanket, TRISO fission blanket, and molten salt coolant.

There are three primary missions for the LIFE engine, which include the burning of excess weapons-grade plutonium (WG-Pu), natural and depleted uranium (DU and HEU), and light-water reactor (LWR) spent nuclear fuel (SNF). Materials in the LIFE Engine will be subjected to a severe radiation and high temperature environment. Such operating conditions will challenge current materials and stimulate development of next-generation materials. The LIFE engine's structural challenges include: need for high-temperature strength; resistance to high-temperature creep; immunity to radiation damage, including swelling and helium embrittlement; resistance to corrosion and environmental cracking in high-temperature molten fluoride salts; and the ability to be fabricated into necessary shapes and configurations with practical welding processes. It is hoped that these challenges can be met with oxide dispersion strengthened (ODS) ferritic steels, sheets and coatings of refractory metals such as tungsten, advanced solid or liquid fuels, and other advanced reactor materials.

The design of LIFE engines capable of meeting the identified missions will require data and models that account for the corrosion and environmental cracking of as-received and irradiated structural and cladding materials in high-temperature molten salt coolants and liquid fuels.

This report is Volume 6 in a 12-volume series, and focuses on the corrosion and environmental cracking of ODS steel during exposure to high-temperature molten-salt coolants and fuels. Discussion includes: the electrochemical potential for reversible reactions; the mixed potential theory, which serves as the basis for predicting the open circuit corrosion potential, and for predicting the beneficial effects of sacrificial anodes; kinetic and mass-transport limited corrosion currents; corrosion rates, based upon corrosion currents; a model for solubility limited

rates of corrosion in molten salts; the criterion for initiation of mechanical fracture; the criterion for initiation of stress corrosion cracking; and various methodologies for studying the corrosion of structural and cladding materials in high-temperature molten salt environments, including linear polarization, electrochemical impedance spectroscopy, corrosion penetration measurement with SEM, concentration profile determination with EDAX mapping, and current-induced thermal cycling for initiation of thermal and thermal-corrosion fatigue. The information discussed within this report was obtained from searches of the published scientific and technical literature, as well as searches of published United States patents pertaining to first-wall materials for fusion reactors.

In regard to corrosion of the structural material in high-temperature fluoride salts, lithium or beryllium can be used as sacrificial anodes in the LIFE engine, providing protection for the engine in a manner similar to that employed with zincs on brass and steel propellers on ships. Since lithium is consumed in the salt, metallic lithium would be the logical choice for passive control. Alternatively, cathodic protection systems could be effectively used to (1) remove virtually all dissolved tritium, deuterium and hydrogen ions in the salt, forming the corresponding gases which would be swept away with noble gas purges; (2) to suppress the anodic dissolution of the oxide dispersion strengthened ferritic structural material, thereby preventing the preferential dissolution of chromium from the ion-base matrix; and (3) to introduce high temperature corrosion inhibitors, perhaps including dissolved chromium, into the melt. Note that in fluoride salts, unlike our more common experience with stainless steel, it is entirely possible, based upon the Gibbs free energies of the respective metal fluoride salts, that the stability of the alloy may actually be improved by removing chromium from the alloy matrix.

Typical corrosion rates range from 5 to 70 mils per year, which reaches a practical limitation as the salt becomes saturated with dissolved chromium. Based upon observation-based corrosion models, it appears that the salt will become saturated with chromium and limit corrosive attack long before the chamber walls are fully penetrated.

Other alloys systems are under consideration that may ultimately provide superior performance at high temperature and high neutron fluence than the current class of ODS ferritic steels, which include, but are not limited to MA956, MA957, EUROFER97 ODS, ODS-9Cr, 12YWT, 14YWT and other publicized variants. All of these materials experience the preferential dissolution of chromium rich phases from the matrix, leaving behind easily observable chromium depletion layers in the near surface region. By selecting alloying elements from the group: W, V, Mo, Ni and possibly Fe, it is in principle possible to evolve a formulation that promises to be more chemically stable in high temperature molten salt coolants and fuels. Enhanced resistance to high temperature and radiation creep can be achieved through the use of a variety of ceramic and intermetallic nanodispersoids to pin dislocations, grain boundaries, and to provide energetic traps within the matrix for helium and hydrogen, thereby helping mitigate tendencies for related embrittlement mechanisms.

In regard to both structural and fuel cladding materials, the Laboratory has substantial and credible experience in the design, development, fabrication and deployment of new engineering alloys systems without lattices. Thus, we have also begun considering, and performing preliminary designs on novel alloys systems that would be virtually immune to lattice damage (displacements per atom). This report will be revised and updated in the future to provide additional information.

Acknowledgements

George Miller, Director, Lawrence Livermore National Laboratory, Financial Support

Edward Moses, Principal Associate Director, National Ignition Facility & Photon Sciences, Visionary Leadership of Project

Tomas Diaz de la Rubia, Principal Associate Director, Science and Technology, Visionary Leadership of Project

Bibliography

G. M. Adamson, R. S. Crouse, W. D. Manly: Interim Report on Corrosion by Alkali Metal Fluorides, ORNL-2337 (Oak Ridge National Laboratory, Oak Ridge, TN, June 5, 1959).

T. R. Allen, J. Gan, J. I. Cole, S. Ukai, S. Shutthanandan and S. Thevuthasan: The stability of 9Cr-ODS oxide particles under heavy-ion irradiation, Nuclear Science & Engineering 151 (2005) 305–312.

P. L. Andresen, F. P. Ford: Intl. Journal of Pressure Vessels and Piping, 59 (1994) 61-70.

P. L. Anderson: Modeling of water and material chemistry effects on crack tip chemistry and resulting crack growth kinetics, 3rd International Conference, Degradation of Materials in Nuclear Power Industry, Traverse City, MI, August 31st through September 4th 1987 (General Electric Corporate Research Center, Schenectady, NY, 1987).

P. L. Andresen, F. P. Ford: Modeling of irradiation effects on stress corrosion crack growth rates, Presented at International Cooperative Group on Irradiation Assisted Stress Corrosion Cracking, 1988 Summer Meeting, Abisko, Sweden, June 7th through 8th 1988 (General Electric Corporate Research Center, Schenectady, NY, 1988).

T. Angeliu, J. Ward and J. Witter: Assessing the effects of radiation damage on Ni-base alloys for the Prometheus space reactor system (LM-06K033, April 4th 2007, Knolls Atomic Power Laboratory, KAPL, Lockheed Martin, P. O. Box 1072, Schenectady, NY 12301-1072, Telephone 518-395-6163, Email angeltm@kapl.gov).

ASTM G 5-94: Standard reference test method for making potentiostatic and potentiodynamic anodic polarization measurements. Designation G 5-94, In *1997 Annual Book of American Society for Testing and Materials Standards*, Section 3, Vol. 3.02 (ASTM, 1997), pp. 54–57.

ASTM G 5-87: Standard reference test method for making potentiostatic and potentiodynamic anodic polarization measurements. Designation G 5-87, In *1989 Annual Book of American Society for Testing and Materials Standards*, Section 3, Vol. 3.02 (ASTM, 1989), pp. 79–85.

ASTM G 3-89: Standard practice for conventions applicable to electrochemical measurements in corrosion testing. Designation G 3-89, In *1997 Annual Book of American Society for Testing and Materials Standards*, Section 3, Vol. 3.02, (ASTM, 1997), pp. 36–44.

ASTM G 61-86: Standard test method for conducting cyclic potentiodynamic polarization measurements for localized corrosion susceptibility of iron-, nickel-, or cobalt-based alloys. Designation G 61-86, In *1997 Annual Book of American Society for Testing and Materials Standards*, Section 3, Vol. 3.02 (ASTM, 1997), pp. 231–235.

A. J. Bard, L. R. Faulkner: Chapter 2, Potentials and Thermodynamics of Cells; Chapter 3, Kinetics of Electrode Reactions; Chapter 4, Mass Transfer by Migration and Electromigration; Chapter 8, Methods Involving Forced Convection Hydrodynamic Methods, Section 8.3, Rotating Disk Electrode; Chapter 9, Techniques Based on Concepts of Impedance, *Electrochemical Methods; Electrochemical Methods, Fundamentals and Applications* (John Wiley & Sons, New York, NY, 1980) pp. 44-85; 86-135; 28-315; 316-369.

C. O. Bennet, J. E. Myers: Chapter 14, Some Design Equations for the Flow of Incompressible Fluids; Chapter 25, Boiling and Condensation, *Heat & Mass Transfer, 2nd Ed.* (McGraw-Hill, 1974) pp. 193-217; 400-417.

E. T. Cheng, B. J. Merril and Dai-Kai Sze: Nuclear aspects of molten salt blankets, *Fusion Engineering and Design*, Fusion Engineering and Design 69 (2003) 205-213.

J. R. Davis, Ferritic Steels, Guide to Materials Selection, *ASM Engineered Materials Handbook*, M. M. Gauthier, Volume Chair (American Society of Metals International, Materials Park, OH, 1995) 116-117.

K. F. Farrell and E. H. Lee: Ion damage in a Fe-10Cr-6Mo-0.5Nb ferritic steel, *Radiation-Induced Changes in Microstructure, 13th International Symposium, Part I*, Garner, Packan, Kumar, Editors, ASTM STP 955 (American Society for Testing and Materials, ASTM, Philadelphia, PA, 1986) pp. 498-519.

M. A. DeLuchi: Hydrogen vehicles: an evaluation of fuel storage, performance, safety, environmental impacts, and cost, *International Journal of Hydrogen Energy* 14, 2 (1989) 81-130.

J. Farmer, B. El-Dasher, M. Serrano de Caro, J. Ferreira: Corrosion of Ferritic Steels in High-Temperature Molten Salt Coolants for Nuclear Applications, Manuscript 518384, Proceedings of

Symposium R, Materials for Future Fusion and Fission Technologies, Chu-Chun Fu, Akihiko Kimura, Maria Samaras, Magdalena Serrano de Caro, Roger E. Stoller, Organizers (Materials Research Society Fall Meeting, Boston, MA, 2008).

J. C. Farmer et al.: Corrosion resistance of amorphous $\text{Fe}_{49.7}\text{Cr}_{17.7}\text{Mn}_{1.9}\text{Mo}_{7.4}\text{W}_{1.6}\text{B}_{15.2}\text{C}_{3.8}\text{Si}_{2.4}$ coating, a new criticality control material, *Journal of Nuclear Technology* 161, 2 (2008) 169-189.

J. C. Farmer et al.: Corrosion resistance of thermally sprayed high-boron iron-based amorphous-metal coatings: $\text{Fe}_{49.7}\text{Cr}_{17.7}\text{Mn}_{1.9}\text{Mo}_{7.4}\text{W}_{1.6}\text{B}_{15.2}\text{C}_{3.8}\text{Si}_{2.4}$, *Journal of Materials Research* 22, 8 (2007) 2297-2311.

J. Farmer, S. Lu, D. McCright, G. Gdowski, F. Wang, T. Summers, P. Bedrossian, J. Horn, T. Lian, J. Estill, A. Lingenfelter, W. Halsey: General and localized corrosion of high-level waste container in Yucca Mountain, The 2000 ASME Pressure Vessel and Piping Conference, Seattle, Washington, July 23-27, 2000, Transportation, Storage, and Disposal of Radioactive Materials, PVP Vol. 408 (2000) 53-70.

J. Farmer, S. Lu, T. Summers, D. McCright, A. Lingenfelter, F. Wang, J. Estill, L. Hackel, H-L. Chen, G. Gordon, V. Pasupathi, P. Andresen, S. Tang, M. Herrera: Modeling and mitigation of stress corrosion cracking in closure welds of high-level waste containers for Yucca Mountain, The 2000 ASME Pressure Vessel and Piping Conference, Seattle, Washington, July 23-27, 2000, Transportation, Storage, and Disposal of Radioactive Materials, PVP Vol. 408 (2000) 71-81.

J. C. Farmer, R. D. McCright: Crevice corrosion and pitting of high-level waste containers: integration of deterministic and probabilistic models, Paper No. 98160, Symposium 98-T-2A, Corrosion 98, San Diego, CA March 22-27, 1998 (National Association of Corrosion Engineers, Houston, Texas, 1998).

J. C. Farmer, F. T. Wang, R. A. Hawley-Fedder, P. R. Lewis, L. J. Summers, L. Foils: Electrochemical treatment of mixed and hazardous wastes, oxidation of ethylene glycol and benzene by silver (II), *Journal of the Electrochemical Society* 139, 3 (1992) 654-662.

J. C. Farmer, F. T. Wang, P. R. Lewis, L. J. Summers: Destruction of chlorinated organics by cobalt (III) mediated electrochemical oxidation, *Journal of the Electrochemical Society*, 139, 11 (1992) 3025-3029.

J. C. Farmer, F. T. Wang, P. R. Lewis, L. J. Summers, Electrochemical treatment of mixed and hazardous wastes: oxidation of ethylene glycol by cobalt (III) and iron (III), *Transactions of the Institute of Chemical Engineering* 70 B (1992) 158-164.

J. C. Farmer, G. E. Gdowski, R. D. McCright, H. S. Ahluwalia: Corrosion models for performance assessment of high-level radioactive waste containers, *Nuclear Engineering Design*, 129 (1991) 57-88.

J. C. Farmer, R. D. McCright: A review of models relevant to the prediction of performance of high-level radioactive waste disposal containers, *Corrosion* 89, April 17-21, 1989, New Orleans, LA (National Association of Corrosion Engineers, Houston, Texas, 1989).

J. C. Farmer: Underpotential deposition of copper on gold and the effects of thiourea studied by AC impedance 132, 11 (1985) 2640-2648.

F. P. Ford: Current understanding of the mechanisms of stress corrosion and corrosion fatigue, *Symposium on Environment-Sensitive Fracture, Evaluation and Comparison of Test Methods*, Gaithersburg, MD, April 25th through 28th 1982, ASTM Special Technical Publication 821, ASTM Publication Code Number (PCN) 04-82100-27, S. W. Dean, E. N. Pugh, G. M. Ugiansky, Editors (American Society of Testing and Materials, Philadelphia, PA, 1983) pp. 32-51.

A. R. Foster, R. L. Wright, Jr.: Chapter 4, Nuclear Reactions, Fusion, Chapter 11, Radiation Damage and Reactor Materials, Dispersion-Type Alloys (TRISO), Chapter 13, Nuclear Reactors, Molten Salt Breeder Reactor, Fusion by Laser, Fusion-Fission Symbiosis, Table 13.6, Typical MSBR Compositions and Properties, Figure 13.31, MSBR Fuel Processing Flow Diagram, *Basic Nuclear Engineering*, 2nd Ed. (Allyn and Bacon, Incorporated, Boston, MA, 1973) pp. 72-80, 330-342, 416-422, 446-449.

W. R. Grimes, S. Cantor: Molten salt as blanket fluids in controlled fusion reactors, *The Chemistry of Fusion Technology*, Plenum Press, 1972.

C. R. Hammond: The Elements, Nomenclature of Inorganic Chemistry, Physical Constants of Inorganic Compounds, *Chemical Rubber Company (CRC) Handbook of Chemistry and Physics*, 61st Ed. (R. C. Weast, M. J. Astle, Editors, CRC Press Incorporated, Boca Raton, FL 33431, 1980) B-2 through B166.

P. N. Haubenreich, J. R. Engel: Experience with the molten-salt reactor experiment, *Nuclear Applications and Technology* 8 (1970) 118-121.

J. E. Indacochea, J. L. Smith, K. R. Litko and E. J. Karell: Corrosion performance of ferrous and refractory metals in molten salts under reducing conditions, *Journal of Materials Research* 14, 5 (1999) 1990-1995.

N. Iwamoto, Y. Makino, K. Furukawa, Y. Katoh, H. Katsuta: *Trans. JWRI* 9, 2 (1980) 117.

R. H. Jones: Stress corrosion cracking, *ASM Metals Handbook*, 9th Ed. Vol. 13 (ASM, Metals Park, OH, 1987) p. 160.

J. R. Keiser, D. L. Manning, R. E. Clausing: in *Proc. Int. Symp. Molten Salts*, J. P. Pemsler et al., Ed. (The Electrochemical Society, Princeton, NJ, 1976) 315.

J. R. Keiser, J. H. DeVan, E. J. Lawrence: *J. Nucl. Mat.* 85/86 (1979) 296.

R. L. Klueh, N. Hashimoto and P. J. Maziasz: New nano-particle-strengthened ferritic-martensitic steels by conventional thermo-mechanical treatment, *Journal of Nuclear Materials* 367-370 (2007) 48-53.

J. W. Koger: *Corrosion*, 29, 3 (1973) 115.

J. W. Koger: *Corrosion*, 30, 4 (1974) 125.

M. Kondo, T. Nagasaka, T. Muroga, A. Sagara, N. Noda, Q. Xu, D. Ninomiya, N. Masaru, A. Suzuki, T. Terai: Corrosion Resistance of Ni-Rich Steels in Molten Salt FLiBe, *Fusion Science and Technology* (18th Topical on the Technology of Fusion Energy, San Francisco, CA, 2008).

G. Y. Lau: *Molten Salt Corrosion*, Chapter 9, *High-Temperature Corrosion of Engineering Alloys* (ASM International, Materials Park, Ohio, 1990) 169-183.

B. J. Makenas, R. G. Trenchard, S. L. Hecht, J. M. McCarthy and F. A. Garner: The effect of swelling in Inconel 600 on the performance of FFTF reflector assemblies, *Radiation-Induced Changes in Microstructure, 13th International Symposium, Part I*, Garner, Packan, Kumar, Editors, ASTM STP 955 (American Society for Testing and Materials, ASTM, Philadelphia, Pennsylvania, 1986) pp. 206-229.

A. K. Misra, J. D. Whittenberger: Fluoride Salts and Container Materials for Thermal Energy Storage Applications in the Temperature Range 973 to 1400K, NASA Tech. Memo. 89913 (NASA Lewis Research Center, Cleveland, OH, 1987).

R. W. Moir, J. D. Lee, F. J. Fulton, F. Huegel, W. S. Neef, Jr., A. E. Sherwood, P. H. Berwald, R. H. Whitley, C. D. C. Wong, J. H. DeVan, W. R. Grimes, S. K. Ghose: Design of a Helium-Cooled Molten-Salt Fusion Breeder, *Fusion Technology* 8 (1985) 465-473.

T. Nakayama, M. Takano: Application of slip-dissolution-repassivation model for stress corrosion cracking of AISI 304 stainless steel in boiling 42% MgCl₂ solution, *Corrosion* 42, 1 (1986) 10-14.

J. S. Newman: Chapter 16, Fundamental Equations; Chapter 17, Convective Transport Problems, Section 103, Rotating Disk, Section 105, Annulus, Section 109, Rotating Cylinder, *Electrochemical Systems*, 2nd Ed. (Prentice Hall, Englewood Cliffs, NJ, 1991), pp. 301-304; 305-339.

H. Nishimura, A. Suzuki, T. Terai, M. Yamawaki, S. Tanaka, A. Sagra and O. Motojima: Chemical behavior of Li₂BeF₄ molten salt as a liquid tritium breeder, *Fusion Engineering and Design* 58-59 (2001) 667-672.

J. A. Ober: Lithium, *2006 Minerals Yearbook; Mineral Commodity Summaries* (USGS, October 2007, Tel 703-648-7717, Email jobber@usgs.gov).

H. Okamoto: *Desk Handbook of Phase Diagrams for Binary Diagrams* (American Society of Metals, International, Materials Park, Ohio, 2000).

A. Paskin, K. Sieradzki, D. K. Som, G. J. Dienes: Dislocation enhancement and inhibition induced by films on crack surfaces, *Acta Metall.* 31, 8 (1983) 1253-1265.

A. Paskin, K. Sieradzki, D. K. Som, G. J. Dienes: Environmentally induced crack nucleation and brittle fracture, *Acta Metall.* 30 (1982) 1781-1788.

A. Paskin, K. Sieradzki, D. K. Som, G. J. Dienes: Computer simulation of crack propagation, *Phys. Rev. Lett.* 44 (1980) 940-943.

L. Pauling: Chapter 15, Oxidation-Reduction Reactions, Electrolysis, *General Chemistry* (Dover Publications, New York, NY, 1947, 1950, 1970) pp. 513-550.

D. Petti, P. Martin, M. Phélip and R. Ballinger: Development of improved models and designs for coated-particle gas reactor fuels (Final Report, International Nuclear Energy Research Initiative (INEEL/EXT-05-02615, Idaho National Engineering and Environmental Laboratory, Idaho Falls, Idaho 83415, December 2004).

D. A. Petti, G. R. Smolik, M. F. Simpson, J. P. Sharpe, R. A. Andrerl, S. Fukada, Y. Hatano, M. Hara, Y. Oya, T. Terai, D-K. Sze, S. Tanaka: Jupiter-II molten salt FLIBE research, an update on tritium, mobilization and redox chemistry experiments, *Fusion Engineering and Design* 81 (2006) 1439-1449.

B. A. Pint, P. F. Tortorelli, A. Jankowski, J. Hayes, T. Muroga, A. Suzuki, O. I. Yelisseyeva, V. M. Chernov: Recent progress in the development of electrically insulating coatings for a liquid lithium blanket, *Journal of Nuclear Materials* 329-333 (2004) 119-124.

B. A. Pint, J. L. Moser and P. F. Tortorelli: Liquid metal compatibility issues for test blanket modules, *Fusion Engineering and Design* 81 (2006) 901-908.

K. A. Romberger, J. Braunstein, R. E. Thoma: New Electrochemical Measurements of the Liquidus in the LiF-BeF₂ System, Congruency of the Li₂BeF₄, *J. Phys. Chem.* 76 (1972) 1154-1159.

M. W. Rosenthal, P. R. Kasten, R. B. Briggs: *Nuclear Technology* 8, 2 (1970) 111.

R. Schaublin et al.: Microstructural development under irradiation in European ODS FM steels, *Journal of Nuclear Materials* 351 (2006) 247-260.

K. B. Shedd, Beryllium, *2006 Minerals Yearbook; Mineral Commodity Summaries* (USGS, October 2007, Tel 703-648-4974, Email ksheddd@usgs.gov).

D. L. Smith, M. C. Billone, K. Natesan: Vanadium-base alloys for fusion first-wall/blanket applications, *International Journal of Refractory Metals and Hard Materials* 18 (2000) 213-224.

I. N. Sviatoslavsky, M. E. Sawan, E. A. Mogahed, S. Majumdar, R. Mattas, S. Malang, P. J. Fogarty, M. Friend, C. P. C. Wong and S. Sharafat: Engineering and geometric aspects of the solid wall re-circulating fluid blanket based on advanced ferritic steel, *Fusion Engineering and Design* 72 (2004) 307-326.

P. A. Thornton and V. J. Colangelo: Chapter 9, Fracture Toughness of Engineering Materials, *Fundamentals of Engineering Materials* (Prentice-Hall Incorporated, Englewood Cliffs, NJ, 1985) pp. 262-325.

R. Treseder, R. Baboian, and C. Munger: Polarization resistance method for determining corrosion rates, *Corrosion Engineer's Reference Book, 2nd Ed.* (National Association of Corrosion Engineers, NACE, Houston, Texas, 1991) pp. 65-66.

D. F. Williams, L. M. Toth and K. T. Clarno: Assessment of candidate molten salt coolants for the advanced high-temperature reactor (ORNL/TM-2006/12, Nuclear Science and Technology Division, Oak Ridge National Laboratory, P.O. Box 2008, Oak Ridge, Tennessee 37831-6283, March 2006).

I. Wright, B. Pint and Z. Ping Lu: Overview of ODS alloy development (Oak Ridge National Laboratory, 1 Bethel Road, Oak Ridge, TN).

S. Ukai, M. Fujiwara: Perspective of ODS alloys application in nuclear environments, *Journal of Nuclear Materials* 307-311 (2002) 749-757.

S. Ukai et al.: Oxide dispersion strengthened (ODS) fuel pin fabrication for BOR-60 irradiation test, *Journal of Nuclear Science & Technology* 42, 1 (2005) 109-122.

S. Ukai and S. Ohtsuka: Low cycle fatigue properties of ODS ferritic-martensitic steels at high temperature, *Journal of Nuclear Materials* 367-370 (2007) 234-238.

I. Ursu: Chapter 5, Moderator Materials, Chapter 12, Materials in Fusion Reactors, *Physics and Technology of Nuclear Materials* (Pergamon Press, New York, New York, 1985) pp. 169-206, 406-457.

W. C. Young: *Roark's Formulas for Stress and Strain, 5th Ed.* (McGraw-Hill Incorporated, San Francisco, CA, 1975).

S. J. Zinkle and N. M. Ghoniem: Operating temperature windows for fusion reactor structural materials, *Fusion Engineering and Design*, 51-51 (2000) 55-71.

S. J. Zinkle: Materials in extreme nuclear environments (Invited Presentation, National Ignition Facility, Lawrence Livermore National Laboratory, March 17, 2008).

Table

Table 1 – Important Physical Properties of Candidate Structural Materials

| Property | Type 316L Stainless Steel | Type HT-9 Ferritic Steel | V-Cr-Ti Alloy |
|--|------------------------------|-----------------------------|------------------|
| Melting Temperature (°C) | 1400 | 1420 | 1890 |
| Density (g/cm ³) | 8.0 | 7.8 | 6.1 |
| Poisson's Ratio | 0.27 | 0.27 | 0.36 |
| Modulus of Elasticity (GPa at 400°C) | 168 | 180 | 120 |
| Linear Thermal Expansion (10 ⁻⁶ /K) | | | |
| 400°C | 17.6 | 11.8 | 10.2 |
| 500°C | 18.0 | 12.3 | 10.3 |
| 600°C | 18.3 | 12.6 | 10.5 |
| Thermal Conductivity (W/m-K) | | | |
| 400°C | 19.5 | 26.8 | 33.6 |
| 500°C | 21.0 | 27.3 | 34.5 |
| 600°C | 22.5 | 27.7 | 35.3 |
| Electrical Resistivity (μm) | | | |
| 400°C | 1.01 | 0.91* | 0.67 |
| 500°C | 1.06 | 0.99* | 0.74 |
| 600°C | 1.12 | 1.05* | |
| Specific Heat (J/kg-K) | | | |
| 400°C | 560 | 600 | 535 |
| 500°C | 575 | 680 | 560 |
| 600°C | 580 | 800 | 575 |

Note: Data from Smith et al. 2000.

Table 2 – Blanket and Coolant Properties

| Salt Formula | Formula Weight | Melting Point | Latent Heat of Fusion | Vapor Pressure (900°C) | Density | Heat Capacity (700°C) | Viscosity | Thermal Conductivity | Neutron Capture vs. Graphite | Moderating Ratio |
|--|----------------|---------------|-----------------------|------------------------|----------------------|---------------------------|-----------|----------------------|------------------------------|------------------|
| | FW | MP | ΔH_f | P_{vap} | ρ | $\rho \times C_p$ | μ | κ | | |
| | (g/mol) | (°C) | (cal/g) | (mm Hg) | (g/cm ³) | (cal/cm ³ /°C) | (cP) | (W/m-K) | | |
| LiF | 25.9 | 842 | | | 2300 | | | | | |
| BeF ₂ | 47.0 | | | | 1086 | | | | | |
| LiF-BeF ₂ | 33.0 | 460 | | 1.2 | 1.94 | 1.12 | 5.6 | 1.00 | 8 | 60 |
| LiF-NaF-BeF ₂ | 38.9 | 315 | | 1.7 | 2.00 | 0.98 | 5.0 | 0.97 | 20 | 22 |
| KF-ZrF ₄ | 103.9 | 390 | | 2.8 | 2.80 | 0.70 | 5.1 | 0.45 | 67 | 3 |
| Rb-ZrF ₄ | 132.9 | 410 | | 1.3 | 3.22 | 0.64 | 5.1 | 0.39 | 14 | 13 |
| LiF-NaF-ZrF ₄ | 84.2 | 436 | | 5.2 | 2.79 | 0.84 | 6.9 | 0.53 | 20 | 13 |
| LiF-NaF-KF | 41.3 | 454 | | 0.7 | 2.02 | 0.91 | 2.9 | 0.92 | 90 | 2 |
| LiF-NaF-RbF | 67.7 | 435 | | 0.8 | 2.69 | 0.63 | 2.6 | 0.62 | 20 | 8 |
| 72LiF-16BeF ₂ -12ThF ₄ | | | 63.00 | 0.1 torr | 3.35 | | 12 | 1.10 | | |
| 70LiF-12BeF ₂ -18ThF ₄ | | | | | 3.87 | | | | | |
| 71LiF-2BeF ₂ -27ThF ₄ | | | 54.00 | | 4.52 | | 15-25 | 0.70 | | |

Note: Data from Williams et al. 2006; Moir et al. 1985; Wright and Foster 1973; Rosenthal et al. 1971.

Table 3 – Free Energies of Formation for Various Fluorides

| Fluoride Salts: Possible Corrosion Products | Free Energy of Formation (kcal/g-mol F) at 1000K |
|--|---|
| MoF ₆ | -50.2 |
| WF ₆ | -56.8 |
| NiF ₂ | -55.3 |
| VF ₅ | -58 |
| VF ₄ | -66 |
| HF | -66.2 |
| FeF ₂ | -66.5 |
| CrF ₂ | -75.2 |
| BeF ₂ | -106.9 |
| LiF | -125.2 |

Note: Data taken from Cheng et al. 2003.

Table 4 – Results of corrosion tests in LiF-19.5CaF₂ at 797°C (1467°F) for 500 h (a)

| Alloy | Depth of Attack μm (mils) | |
|------------|--------------------------------------|--------------------|
| | General (b) | Grain Boundary (c) |
| Mild Steel | | 155 (6.1) |
| 304 | | 185 (7.3) |
| 310 | | 130 (5.1) |
| 316 | | 165 (6.5) |
| RA330 | | 270 (10.6) |
| B | 30 (1.2) | |
| N | 15 (0.6) | 15 (0.6) |
| S | 90 (3.5) | |
| X | | 140 (5.5) |
| 600 | 90 (3.5) | 30 (1.2) |
| 718 | 45 (1.8) | 120 (4.7) |
| 75 | 30 (1.2) | 135 (5.3) |
| 25 | | 95 (3.7) |
| 188 | | 105 (4.1) |

Note: Data taken from Lau 1990.

Table 5 – Corrosion of Steels in High Temperature Molten Salts

| Loop # | Alloy | Salt | Duration (hours) | T _{max} (°C) | Corrosion Depth (mil) | Corrosion Rate (mil/yr) | ONL Report [Reference] |
|--------|---------|--------------------------------|------------------|-----------------------|-----------------------|-------------------------|------------------------|
| | | | | | | | |
| 116 | 316SS | FLiNaK | 500 | 815 | 4.0 | 70.1 | 1294 |
| 119 | 316SS | FLiNaK + NaK | 500 | 815 | 2.0 | 5.8 | 1294 |
| 347 | Inconel | 50NaF-50ZrF ₄ | 3000 | 815 | 11.0 | 32.1 | 1692 |
| 518 | Inconel | NaF-ZrF ₄ | 3000 | 815 | 11.0 | 48.2 | 2338 |
| 346 | Inconel | 50NaF-50ZrF ₄ | 2000 | 815 | 9.0 | 39.4 | 1692 |
| 519 | Inconel | NaF-ZrF ₄ | 2000 | 815 | 12.5 | 109.5 | 1692 |
| 78 | Inconel | FLiNaK | 1000 | 815 | 13.0 | 113.9 | 1294, 2337 |
| | Inconel | NaF-ZrF ₄ | 1000 | 815 | 3.0 | 26.3 | [76] |
| 278 | Inconel | NaF-ZrF ₄ | 1000 | 815 | 5.0 | 43.8 | 2338 |
| 399 | Inconel | NaF-ZrF ₄ | 1000 | 815 | 10.0 | 87.6 | 2338 |
| | Inconel | 60NaF-40ZrF ₄ | 1000 | 815 | 5.0 | 43.8 | CF-57-9-35 |
| | Inconel | 50NaF-50BeF ₂ | 1000 | 815 | 8.0 | 70.1 | CF-57-9-35 |
| | Inconel | 70NaF-30BeF ₂ | 1000 | 815 | 6.0 | 52.6 | CF-57-9-35 |
| | Inconel | 24LiF-53NaF-23BeF ₂ | 1000 | 815 | 5.0 | 43.8 | CF-57-9-35 |
| | Inconel | 36LiF-49NaF-15BeF ₂ | 1000 | 815 | 3.0 | 26.3 | CF-57-9-35 |
| | Inconel | 74LiF-26ThF ₄ | 1000 | 815 | 6.0 | 63.9 | CF-57-9-35 |
| 517 | Inconel | NaF-ZrF ₄ | 822 | 815 | 5.5 | 83.8 | 2338 |
| 337 | Inconel | NaF-ZrF ₄ | 575 | 815 | 8.0 | 140.2 | 2338 |
| 214 | Inconel | FLiNaK + NaK | 500 | 815 | 3.0 | 52.6 | 1294 |
| 230 | Inconel | 36NaF-18KF-46ZrF ₄ | 500 | 815 | 10.0 | 175.2 | 1375 |
| 348 | Inconel | 50NaF-50ZrF ₄ | 500 | 815 | 5.5 | 96.4 | 1692 |
| | Inconel | FLiNaK | 500 | 815 | 7.0 | 122.6 | 1816 |
| 934 | Inconel | 60NaF-40ZrF ₄ | 500 | 815 | 5.0 | 87.6 | 2157 |
| 935 | Inconel | 60NaF-40ZrF ₄ | 500 | 815 | 5.0 | 87.6 | 2157 |
| | Inconel | NaF-BeF ₂ | 500 | 815 | 10.0 | 175.2 | [76] |
| | Inconel | LiF-NaF-BeF ₂ | 500 | 815 | 5.0 | 87.6 | [76] |

| | | | | | | | |
|--------|---------|--|-------|-----|------|-------|------|
| 246 | Inconel | 52NaF-48ZrF ₄ | 500 | 815 | 8.0 | 140.2 | 2337 |
| 262 | Inconel | 57NaF-43BeF ₂ | 500 | 815 | 9.0 | 157.7 | 2337 |
| 277 | Inconel | 50NaF-50ZrF ₄ | 500 | 815 | 5.0 | 87.6 | 2337 |
| 276 | Inconel | NaF-ZrF ₄ | 500 | 815 | 8.0 | 140.2 | 2338 |
| 277 | Inconel | NaF-ZrF ₄ | 500 | 815 | 4.0 | 70.1 | 2338 |
| 336 | Inconel | NaF-ZrF ₄ | 500 | 815 | 6.0 | 105.1 | 2338 |
| 341 | Inconel | NaF-ZrF ₄ | 500 | 815 | 5.5 | 96.4 | 2338 |
| 342 | Inconel | NaF-ZrF ₄ | 500 | 815 | 6.0 | 105.1 | 2338 |
| 516 | Inconel | NaF-ZrF ₄ | 500 | 815 | 6.0 | 105.1 | 2338 |
| 338 | Inconel | NaF-ZrF ₄ | 500 | 815 | 6.0 | 210.2 | 2338 |
| 411 | Inconel | NaF-ZrF ₄ | 250 | 815 | 4.5 | 394.2 | 2338 |
| 410 | Inconel | NaF-ZrF ₄ | 100 | 815 | 4.0 | 700.8 | 2338 |
| 400 | Inconel | NaF-ZrF ₄ | 50 | 815 | 3.0 | 3.0 | 2338 |
| 1181 | Inconel | 71LiF-29ThF ₄ | 8760 | 732 | 6.5 | 6.5 | 2684 |
| 1239 | Inconel | 71LiF-16BeF ₂ -13ThF ₄ | 8760 | 732 | 7.5 | 5.0 | 2973 |
| 9377-6 | Inconel | 71LiF-16BeF ₂ -13ThF ₄ | 13155 | 704 | 13.0 | 13.0 | 3215 |
| 1188 | Inconel | 35LiF-27NaF-38BeF ₂ | 8760 | 677 | 9.0 | 9.0 | 2723 |
| 1210 | Inconel | 71LiF-29ThF ₄ | 8760 | 677 | 5.0 | 5.6 | 2799 |
| 1235 | Inconel | 71LiF-16BeF ₂ -13ThF ₄ | 7789 | 677 | 4.0 | 7.5 | 2973 |
| 1214 | Inconel | FLiNaK | 4673 | 677 | 13.0 | 113.9 | 2684 |
| 1169 | Inconel | 71LiF-29ThF ₄ | 1000 | 677 | 1.0 | 8.8 | 2474 |
| 1177 | Inconel | 71LiF-29ThF ₄ | 1000 | 677 | 1.5 | 13.1 | 2474 |
| 1173 | Inconel | 58NaF-35BeF ₂ -7ThF ₄ | 1000 | 677 | 4.0 | 35.0 | 2474 |
| 1176 | Inconel | 58LiF-35BeF ₂ -7ThF ₄ | 1000 | 677 | 1.0 | 8.8 | 2474 |
| 1234 | Inconel | 71LiF-16BeF ₂ -13ThF ₄ | 1000 | 677 | 1.0 | 1.0 | 2799 |
| 9344-2 | Inconel | FLiNaK | 8760 | 649 | 8.0 | 8.0 | 2890 |
| 9344-2 | Inconel | FLiNaK | 8735 | 649 | 8.0 | 70.1 | 3215 |
| 1172 | Inconel | 35LiF-27NaF-38BeF ₂ | 1000 | 607 | 2.0 | 17.5 | 2474 |
| 1175 | Inconel | FLiNaK | 1000 | 607 | 1.0 | 2.9 | 2474 |
| LDRD | INOR-8 | FLiNaK | 3048 | 815 | 0.1 | 0.1 | [77] |
| 1209 | INOR-8 | 71LiF-29ThF ₄ | 8760 | 732 | 0.0 | 0.0 | 2799 |
| 1216 | INOR-8 | 58LiF-35BeF ₂ -7ThF ₄ | 8760 | 732 | 1.0 | 1.0 | 2973 |
| 1240 | INOR-8 | 71LiF-16BeF ₂ -13ThF ₄ | 8760 | 732 | 0.0 | 0.0 | 2973 |
| MSRP | INOR-8 | 71LiF-16BeF ₂ -13ThF ₄ | 20000 | 704 | 1.0 | 0.9 | 3215 |

| | | | | | | | |
|-----------|--------|--|-------|-----|-----|-----|---------|
| 7 | | | | | | | |
| MSRP 8 | INOR-8 | 58LiF-35BeF ₂ -7ThF ₄ | 9633 | 704 | 0.0 | 0.0 | 3215 |
| 15A | INOR-8 | 73LiF-2BeF ₂ -25ThF ₄ | 39476 | 677 | 0.1 | 0.1 | TM-4286 |
| 1208 | INOR-8 | FLiNaK | 8760 | 677 | 1.0 | 1.0 | 2799 |
| 1190 | INOR-8 | 58NaF-35BeF ₂ -7ThF ₄ | 8760 | 677 | 1.0 | 1.0 | 2799 |
| 1233 | INOR-8 | 71LiF-16BeF ₂ -13ThF ₄ | 8760 | 677 | 0.0 | 0.0 | 2973 |
| 1213 | INOR-8 | 71LiF-29ThF ₄ | 3114 | 677 | 0.0 | 0.0 | 2626 |
| 15 | INOR-8 | 73LiF-2BeF ₂ -25ThF ₄ | 2003 | 677 | 0.0 | 0.0 | TM-4286 |
| 1165 | INOR-8 | FLiNaK | 1340 | 677 | 0.0 | 0.0 | 2551 |
| 1164 | INOR-8 | 58NaF-35BeF ₂ -7ThF ₄ | 1000 | 677 | 0.0 | 0.0 | 2551 |
| 1221 | INOR-8 | 71LiF-29ThF ₄ | 1000 | 677 | 0.0 | 0.0 | 2626 |
| 1228 | INOR-8 | 71LiF-16BeF ₂ -13ThF ₄ | 1000 | 677 | 0.0 | 0.0 | 2723 |
| MSRE | INOR-8 | 67LiF-33BeF ₂ | 26000 | 649 | 0.0 | 0.0 | TM-4174 |
| 9354-3 | INOR-8 | 35LiF-27NaF-38BeF ₂ | 19942 | 649 | 0.0 | 0.0 | 3215 |
| 1194 | INOR-8 | FLiNaK | 1000 | 607 | 0.0 | 0.0 | 2551 |
| 1195 | INOR-8 | 35LiF-27NaF-28BeF ₂ | 1000 | 607 | 0.0 | 0.0 | 2551 |

Note: Data taken from Williams et al. 2006.

Table 6 – Solubility of Chromium in Various Fluoride Salts

| Salt mixture | ZrF ₄ or BeF ₂ (mol %) | UF ₄ (mol %) | Cr at 600°C (ppm) | Cr at 800°C (ppm) |
|--------------------------------|---|----------------------------|----------------------|----------------------|
| FLiNaK | 0 | 2.5 | 1100 | 2700 |
| LiF-ZrF ₄ | 48 | 4 | 2900 | 3900 |
| NaF-ZrF ₄ | 50 | 4.1 | 2300 | 2550 |
| NaF-ZrF ₄ | 47 | 4 | 1700 | 2100 |
| NaF-ZrF ₄ | 41 | 3.7 | 975 | 1050 |
| KF-ZrF ₄ | 48 | 3.9 | 1080 | 1160 |
| 22NaF-55LiF-23ZrF ₄ | 23 | 2.5 | 550 | 750 |
| LiF-BeF ₂ | 48 | 1.5 | 1470 | 2260 |

Note: Data taken from Williams et al. 2006.

Figures

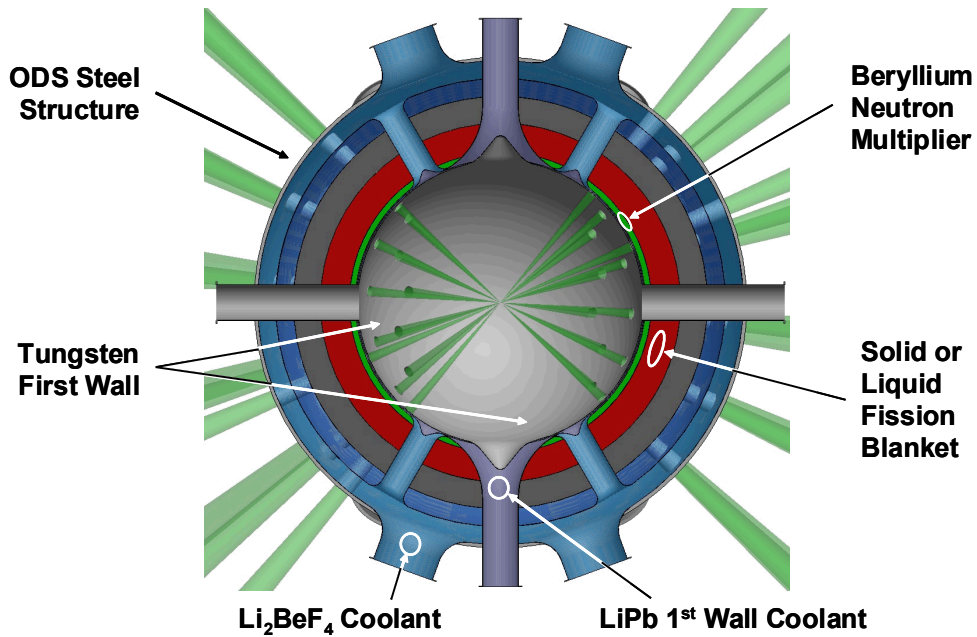


Figure 1 – Structure of LIFE engine, showing contacting of ODS ferritic steel structure, fission fuel, and beryllium neutron multiplier by flowing molten salt coolants.

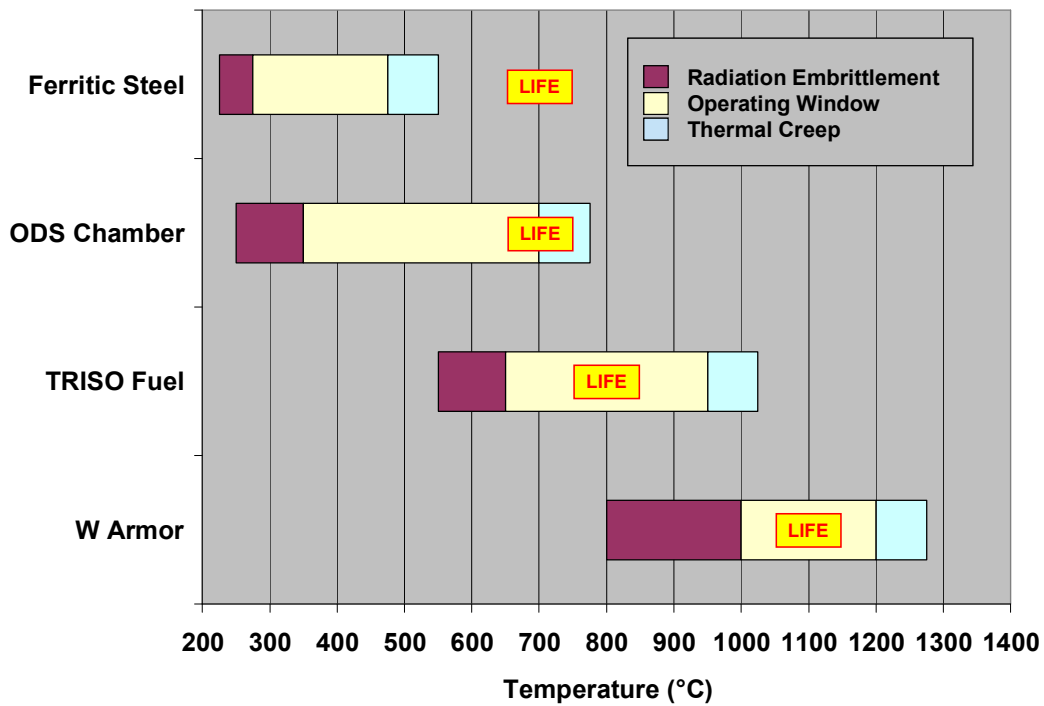


Figure 2 – The operating windows for materials used to construct the LIFE engine are bounded by radiation embrittlement at lower temperatures, and by thermal creep at higher temperatures.

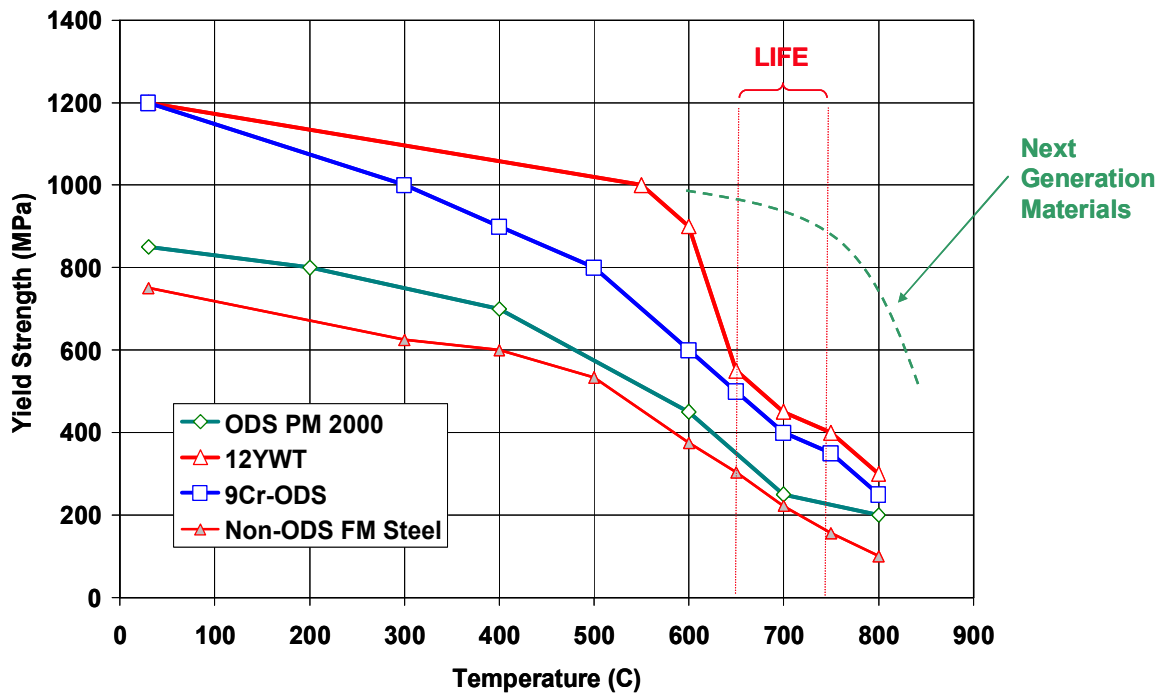


Figure 3 – Yield strength of new ODS FM steels such as 9Cr-ODS & Kobe 12YWT showing exceptional yield strength at high temperature.

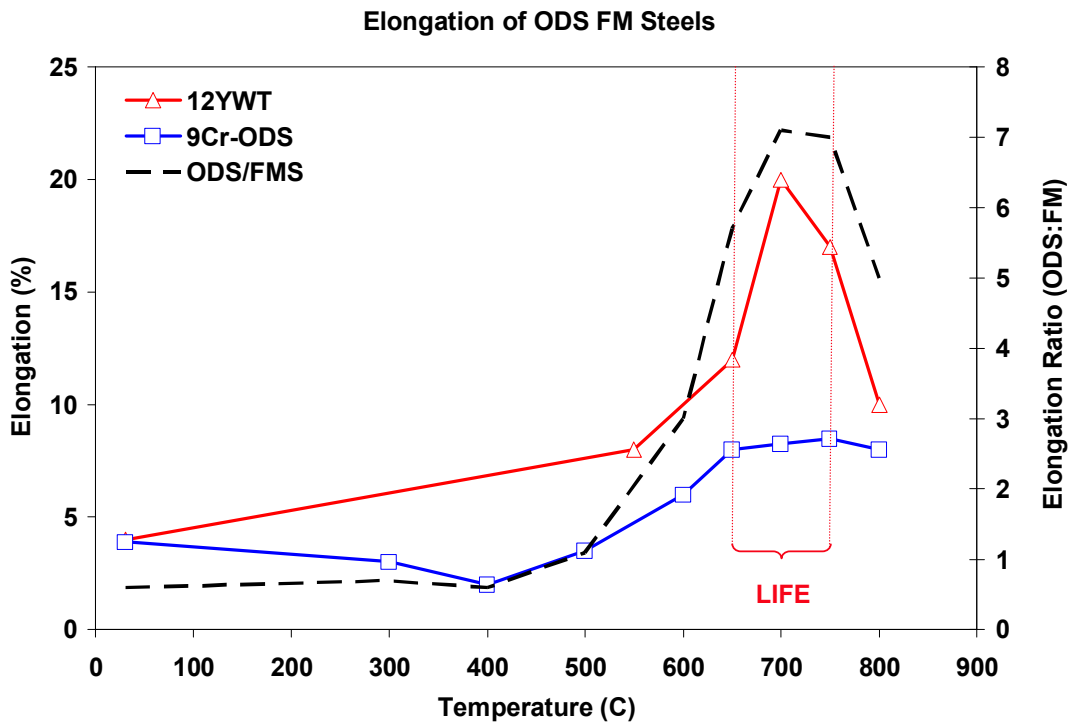


Figure 4 – Elongation of new ODS FM steels such as 9Cr-ODS & Kobe 12YWT showing exceptional creep resistance at high temperature.

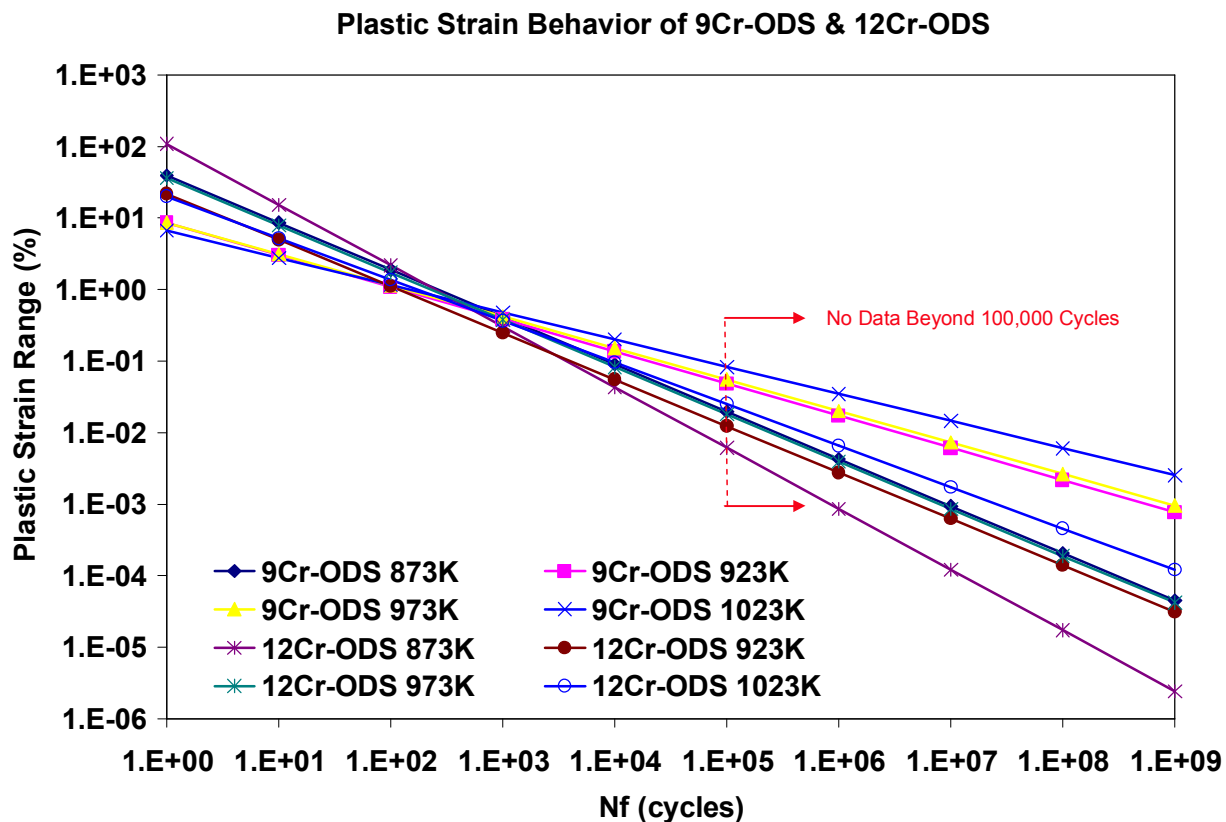


Figure 5 – ODS ferritic-martensitic steel has longer fatigue life than conventional ferritic steels such as modified 9Cr-1Mo steel.

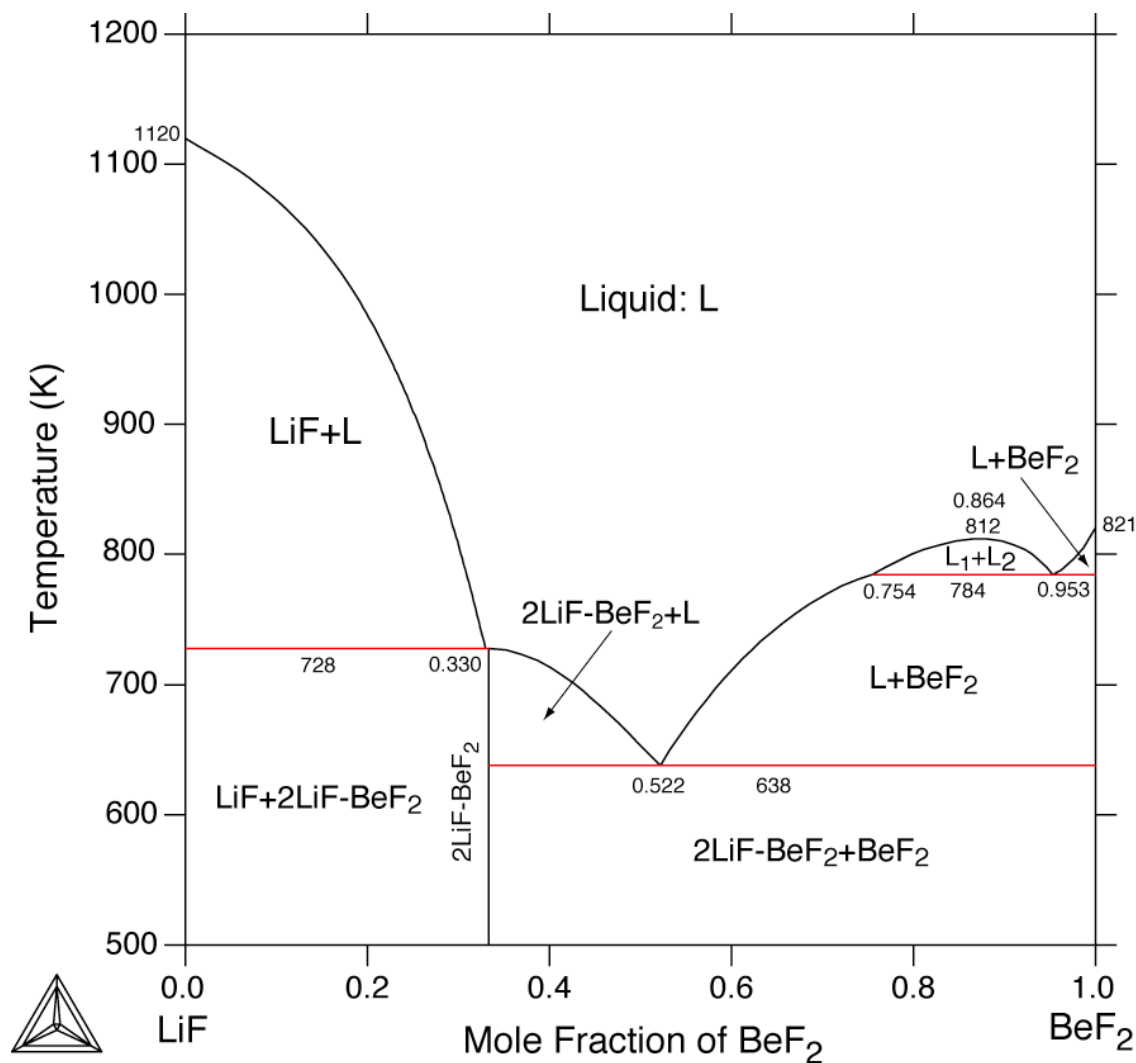


Figure 6 – A binary mixture of BeF₂ and LiF produces a eutectic composition. The mixture of BeF₂ and LiF forms a low-melting eutectic (Li₂BeF₄) with a melting point of less than 638 K (365°C).

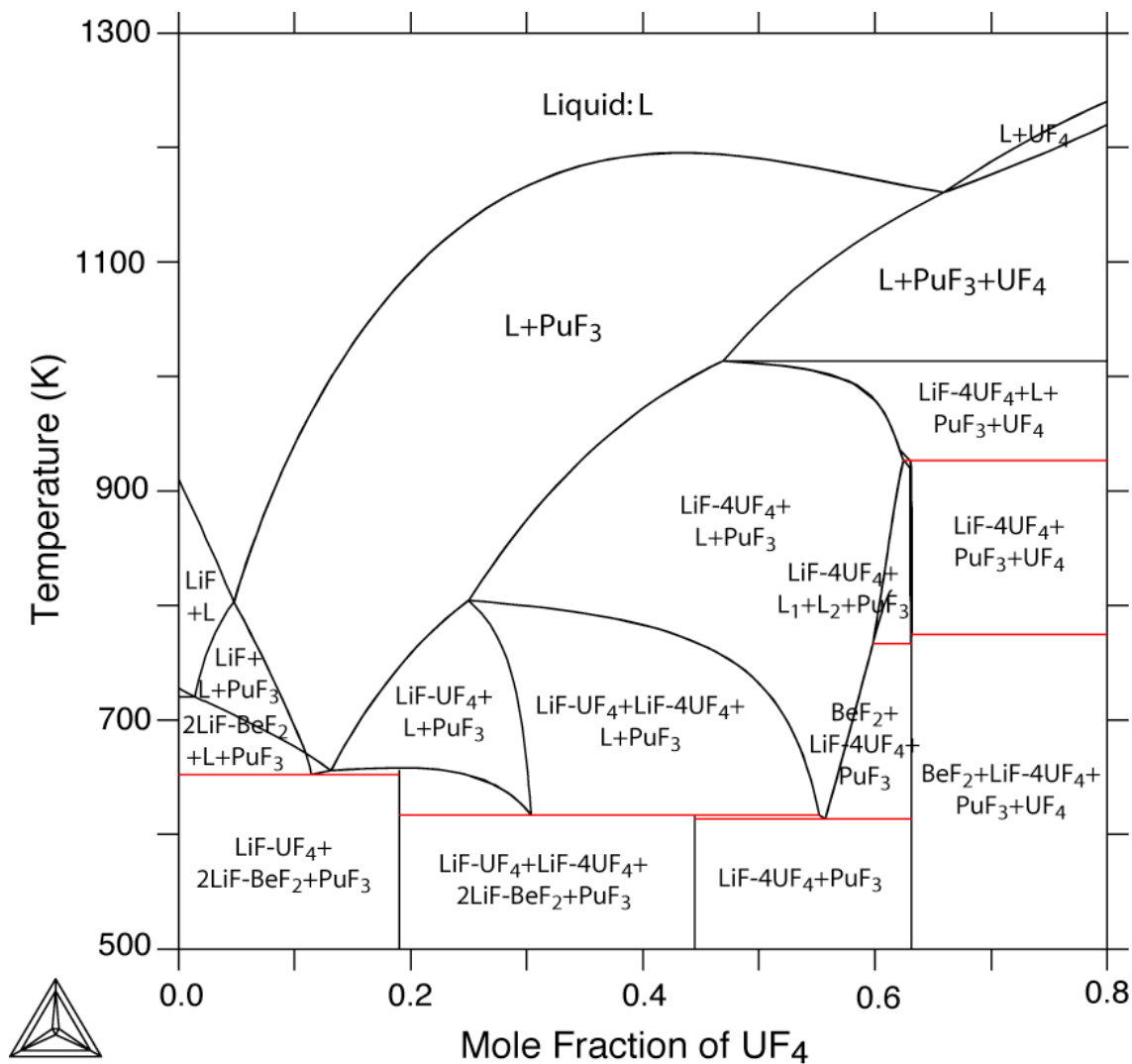


Figure 7 – Calculated phase diagram for molten salt fuel, showing regions of composition and temperature where only liquid exists, which defines the limits of safe operation. The solubility of PuF_3 and other fission product salts bound the safe operating temperature for liquid fuels.

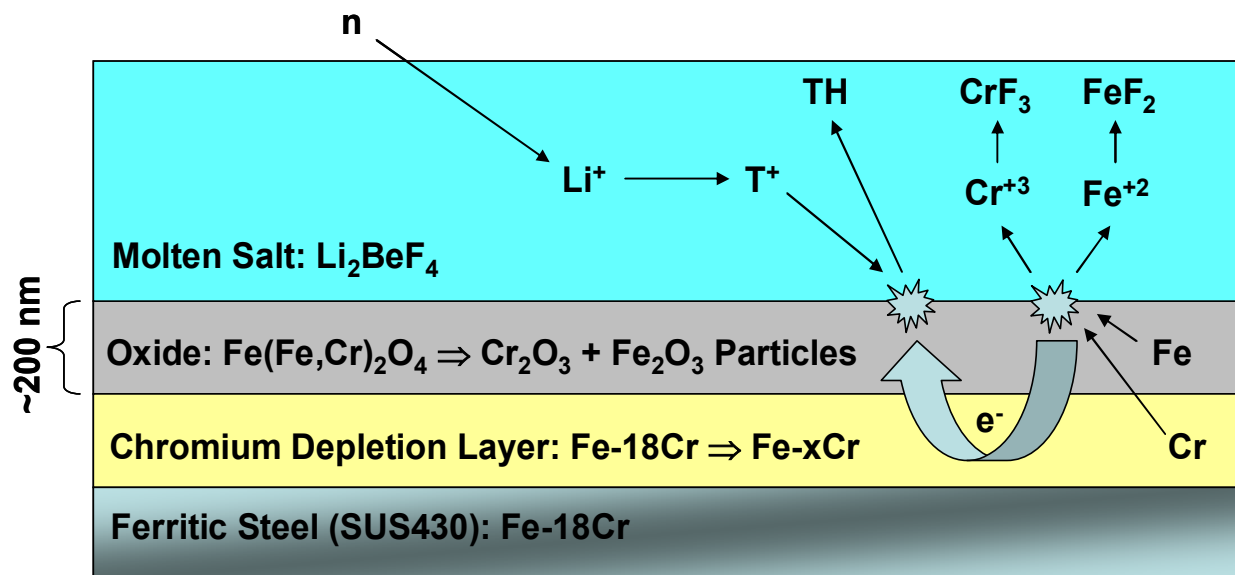


Figure 8 – Corrosion mechanism for ODS ferritic steel in molten FLIBE based upon discussion in the literature.

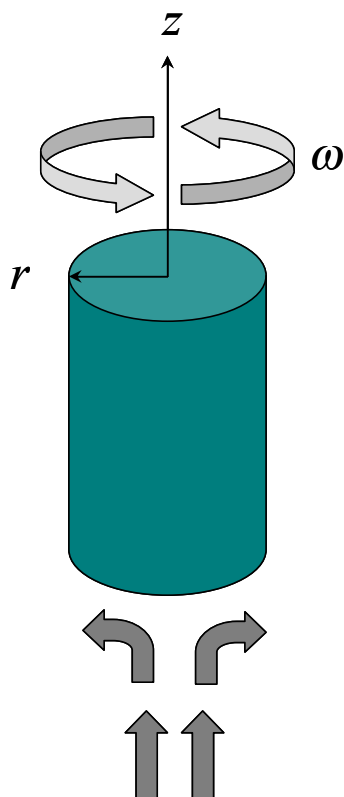


Figure 9 – Schematic representation showing rotating disk electrode (lower face of cylinder), with the fluid flow approaching the electrode normal to the lower surface.

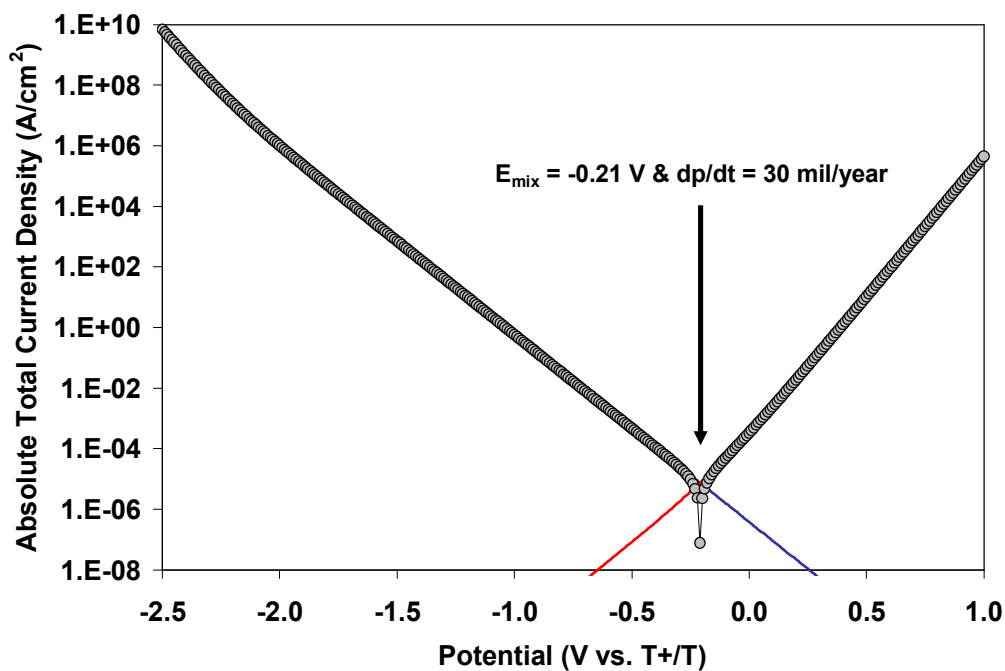


Figure 10 – Mixed potential theory applied to ODS ferritic steel without sacrificial beryllium anode in molten Li_2BeF_4 at 815°C .

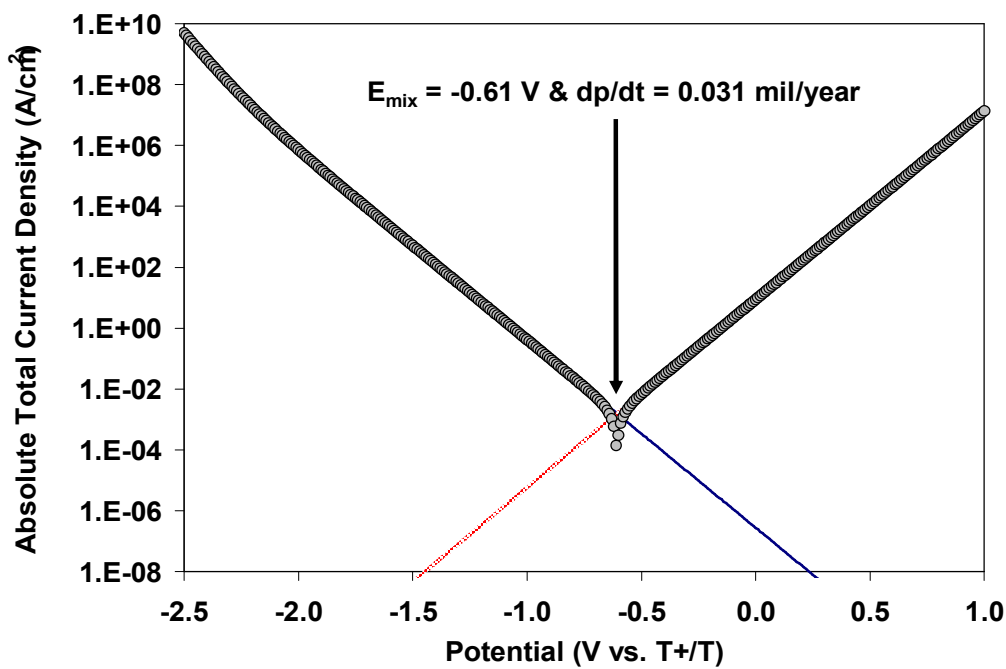


Figure 11 – Mixed potential theory applied to ODS ferritic steel with sacrificial beryllium anode in molten Li_2BeF_4 at 815°C .

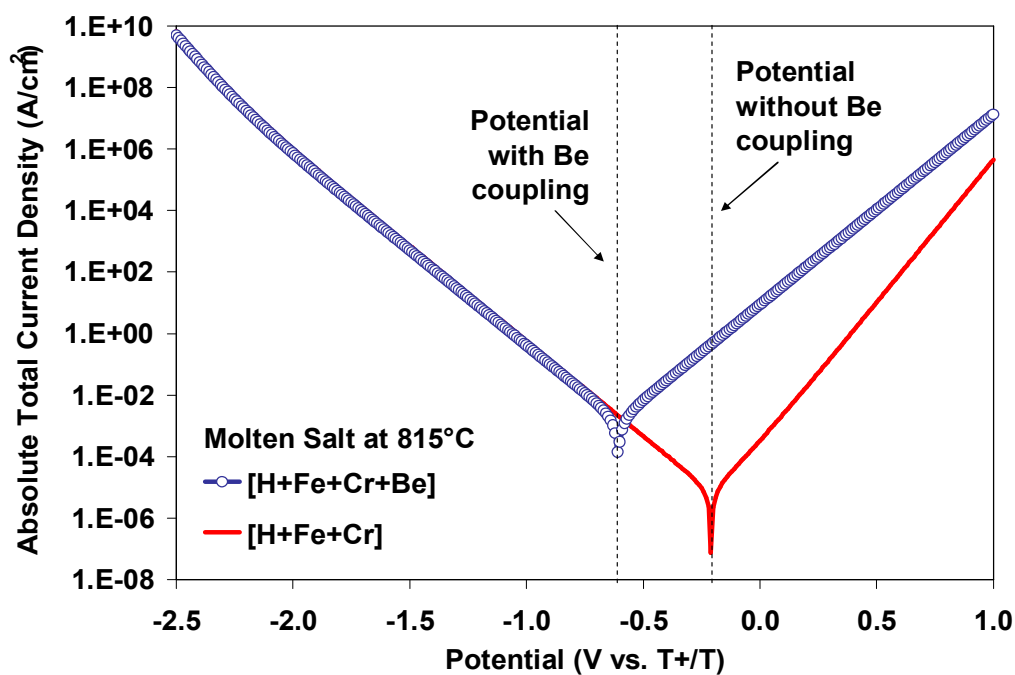


Figure 12 – A comparison of these two curves, taken from Figures 10 and 11 respectively, clearly show the cathodic shift of the open circuit corrosion potential due to galvanic coupling of beryllium and ODS steel at 815°C. A comparison of these two curves shows the cathodic shift of the corrosion potential due to galvanic coupling.

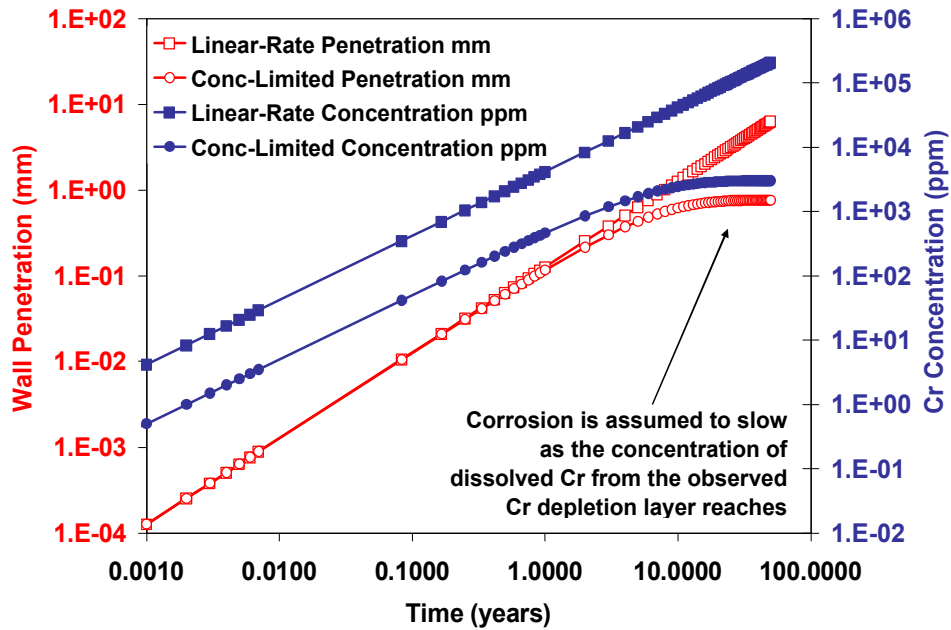


Figure 13 – Limited corrosive attack of ODS by molten salts at 815°C, assuming a rate of attack of 5.0 mils per year, and saturation of the salt with chromium at a concentration of approximately 3000 ppm.

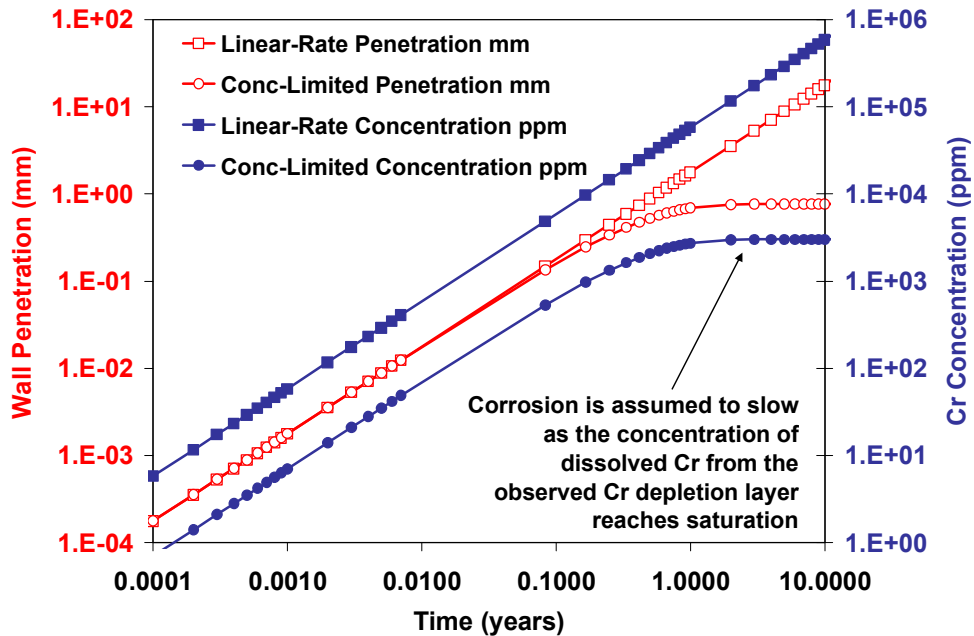


Figure 14 – Limited corrosive attack of ODS by molten salts at 815°C, assuming a rate of attack of 70.1 mils per year, and saturation of the salt with chromium at a concentration of approximately 3000 ppm.

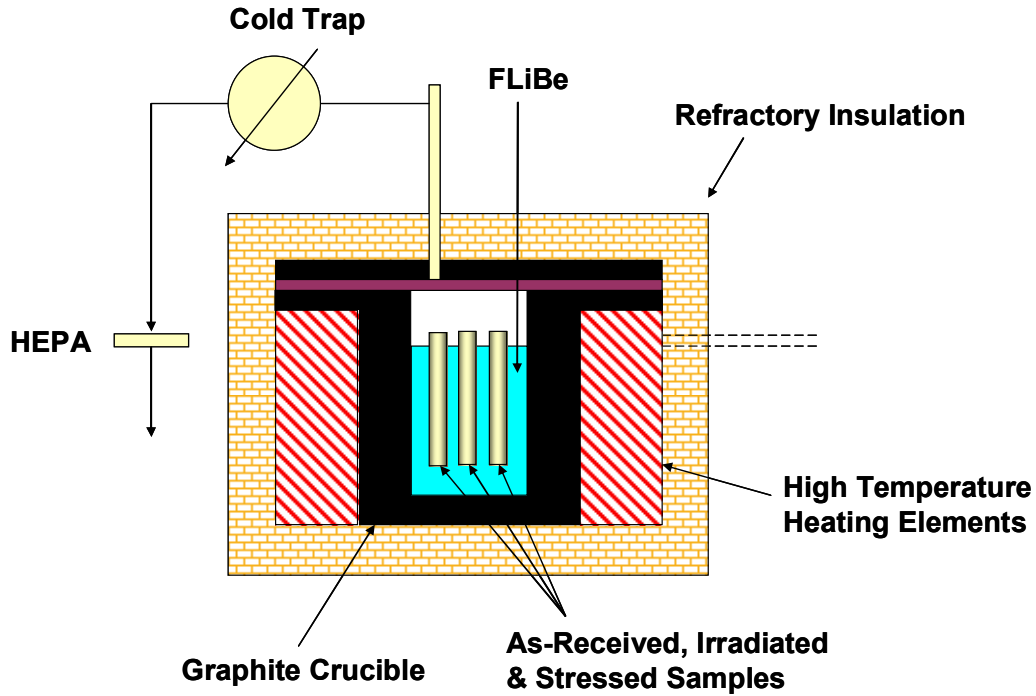


Figure 15 – This drawing shows a cross-sectional view of a high temperature test chamber, showing the exposure of multiple samples of structural or cladding material.

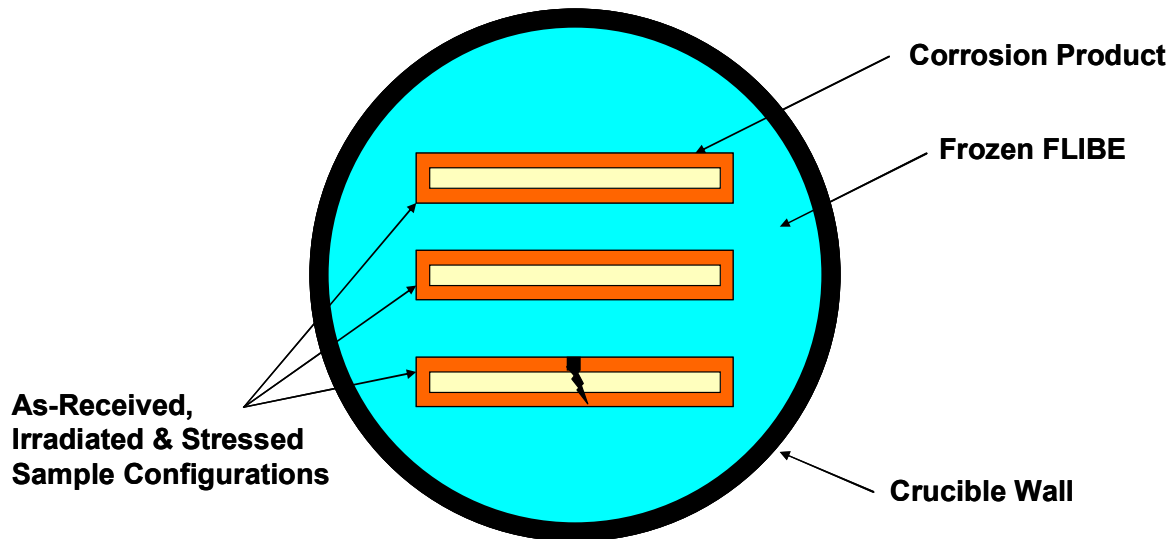


Figure 16 – The samples can be frozen in the high-temperature molten fluoride salt for cross-sectioning to enable scanning electron microscopy (SEM) and energy dispersive analysis with X-rays (EDAX), thereby enabling elemental mapping of the corroded interface, and the concentration profile of dissolved metals in the frozen salt.

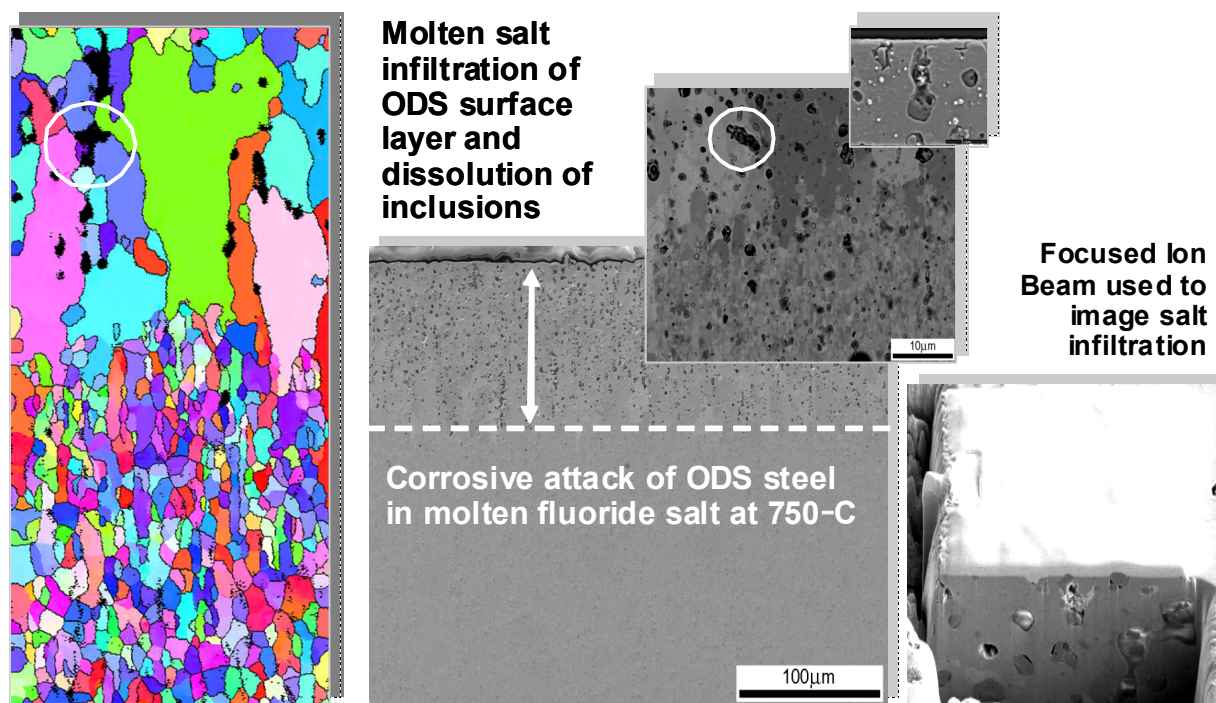


Figure 17 – The image on the left is a crystallographic map showing micron-size grains in the high chromium ODS steel that was tested in FLINAK at at 750°C. The layer closest to the surface is believed to have experienced grain growth due to heating and machining. The electron microscopy in the center shows the formation of voids due to the preferential dissolution of chromium rich phases in the near surface region of the material. This mode of attack penetrated to a depth of approximately 100 microns. The image on the right shows the infiltration of molten fluoride salt into the surface voids formed by preferential chromium dissolution revealed in three dimensional.

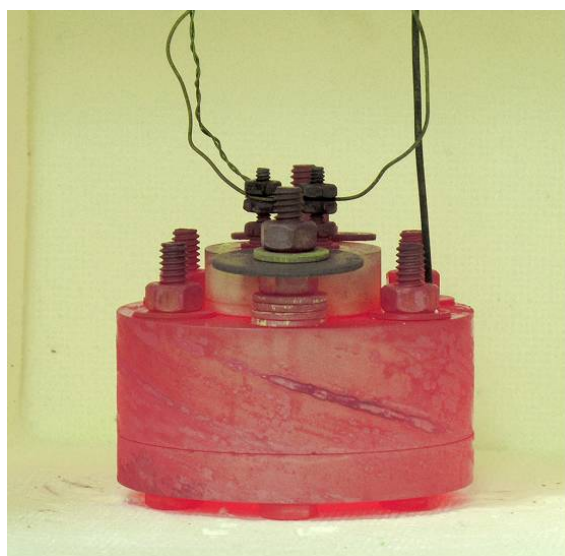
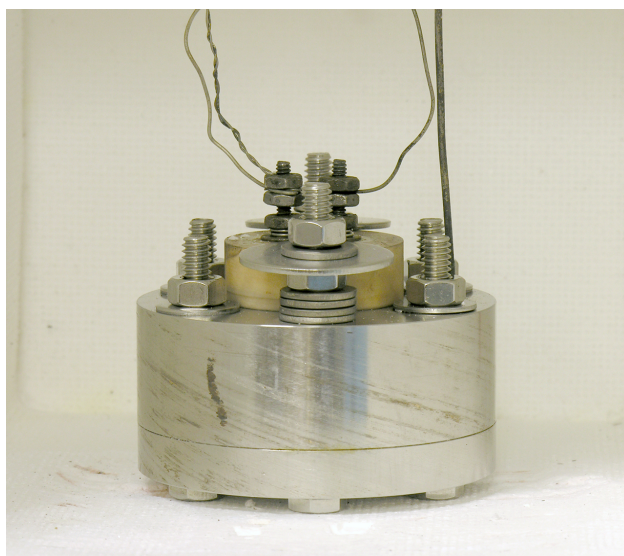
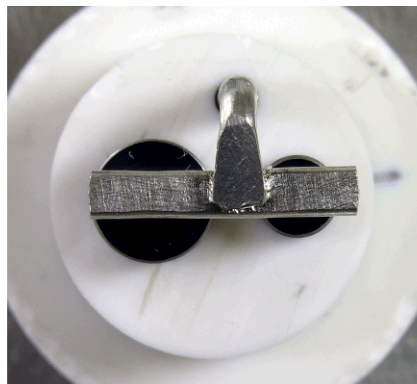
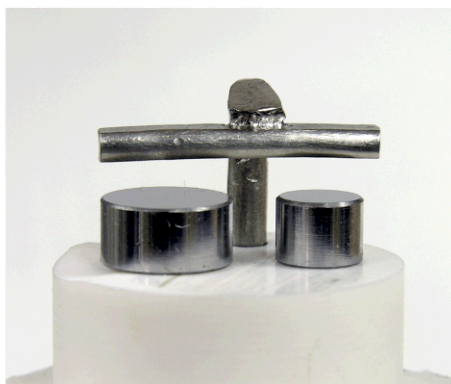


Figure 18 – Electrochemical cell for corrosion testing of structural and cladding materials in high-temperature molten fluoride salts. The material being tested is held in the cell by a machined ceramic plug. The lower right image shows the cell at 800°C.

Platinum Bar Counter Electrode
& ODS Steel Button Electrodes



- Pt electrode, formed and laser welded 0.125" rod
- ODS steel electrodes, 0.25" and 0.375" dia. x 0.1875" high
- Macor ceramic (white) electrode fixture assembly

Figure 19 – Photographs showing working electrode (larger disk of ODS steel on left), reference electrode (smaller disk of ODS steel on right), and counter electrode (platinum bar suspended above the two ODS steel disks).

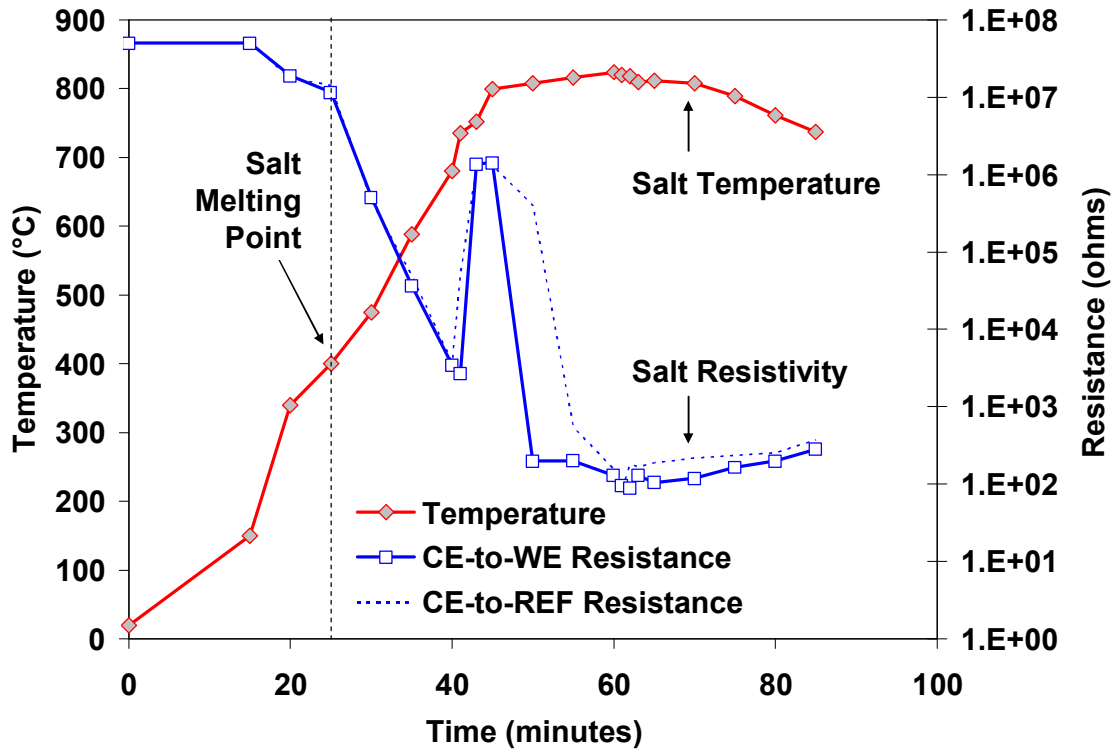


Figure 20 – Electrical resistance of high-temperature electrochemical cell for testing structural and cladding materials in high-temperature molten-salt environments showing the melting of the salt and wetting of the sample as the cell is heated to 800°C. Such monitoring enables experimentalist to determine when to begin measurements.

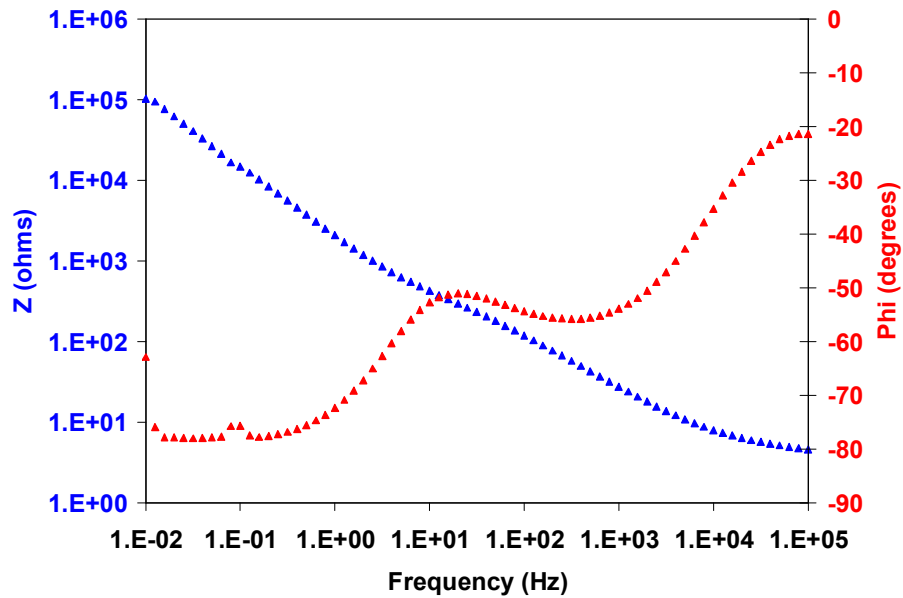


Figure 21 – The ability to perform *in situ* electrochemical impedance spectroscopy (EIS) of steel surface in molten-salt at 800°C has been demonstrated. We can now begin to elucidate high temperature molten salt corrosion mechanisms and monitor corrosion rates at 363°C to temperatures above 800°C *in situ*.

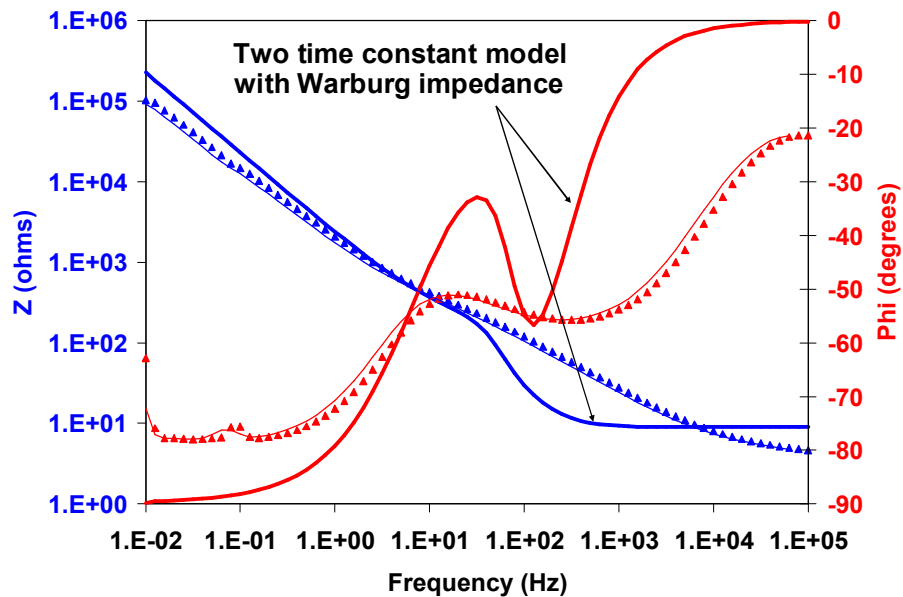


Figure 22 – The simple single time-constant equivalent circuit is insufficient to explain EIS spectra. A two time constant model is required to explain observed impedance spectra qualitatively, with more parameters needed for better fit.

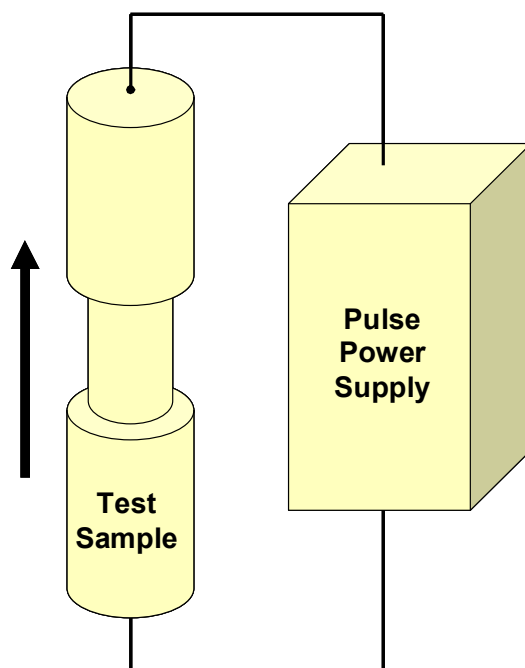


Figure 23 – Test sample of ODS ferritic steel being thermally stressed for fatigue and corrosion fatigue studies with current pulse.

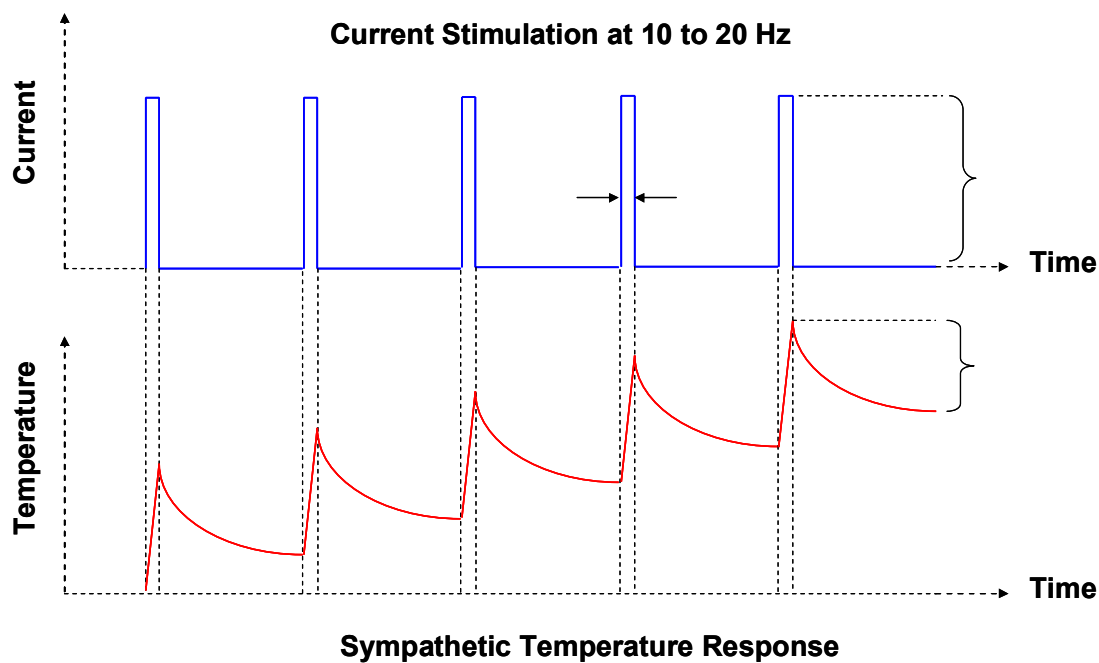


Figure 24 – Timing chart showing current pulse and sympathetic transient temperature during testing of a sample such as ODS steel.

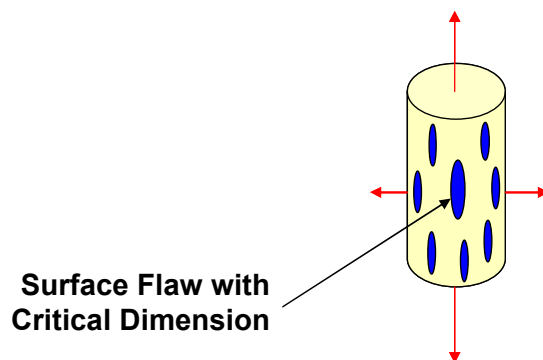


Figure 25 – Schematic showing surface flaws where corrosion fatigue cracking can initiate and propagate.

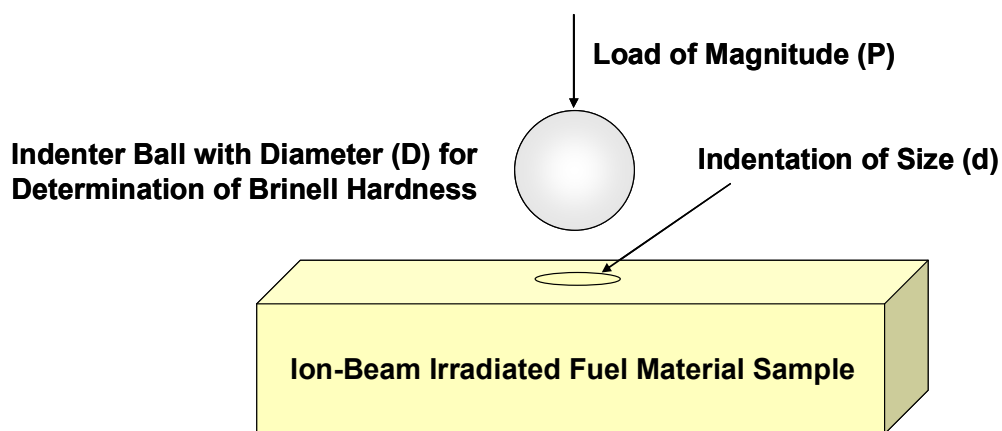


Figure 26 – Schematic showing the determination of the Ultimate Tensile Strength (UTS) of ion-beam irradiated sample through determination of the Brinell Hardness Number (BHN).

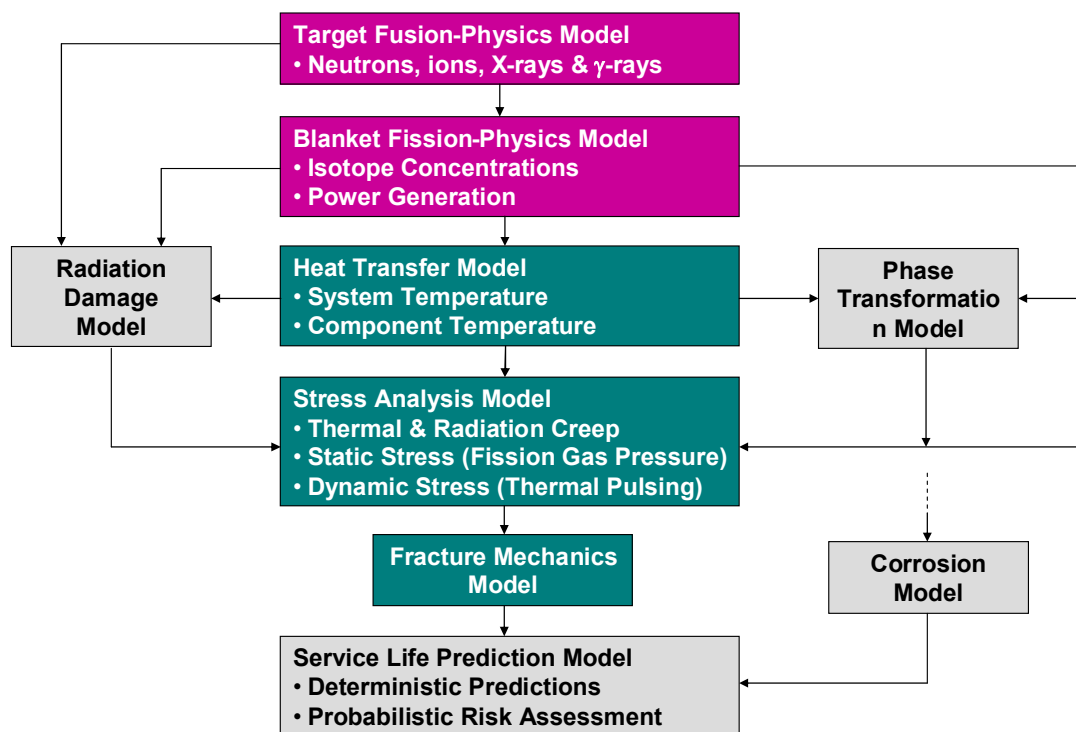


Figure 27 – A systematic approach to materials modeling will enable design of next-generation materials.